



Laser micromachining of metal tools to adjust overall adhesion of composites to the tool surface

Shashini Rathnayaka
Department of Chemical Engineering
McGill University, Montreal
July 2023

A thesis submitted to McGill University in partial fulfillment of the requirements of the
degree of the Master of Science

© Shashini Rathnayaka 2023

Abstract

Epoxy resin to metal surface adhesion is of importance to composite manufacturing industries since composite parts are mostly fabricated in metal molds. At the composite fabrication stage, the resin-metal interface is desired to have low adhesion for easy demolding of the cured composite. This research studied the feasibility of using micro/nano scale topography modifications introduced through femtosecond (fs) laser micromachining to hinder epoxy resin adhesion on aluminum alloy substrates. The main hypotheses were that air bubbles trapped in microcavities reduce the interfacial area which causes lower adhesion. Simultaneously, the same voids can promote adhesive failure at the resin-metal interface. Therefore, the project analyzed adhesion strength as a function of different femtosecond laser micromachined geometries on metal surfaces. Hexagonal holes, circular holes, and periodic ripple structures were micromachined on bare aluminum alloy substrates. Contact angle goniometry was performed to measure the static contact angle of the resin solution on metal substrates at the curing temperature. Tensile tests were carried out to determine the adhesion strength. An epoxy resin layer cured between two similarly laser micromachined substrates was used for tensile testing. Scanning electron microscopy and laser scanning profilometry were used to analyze failure modes and detect resin penetration into microcavities. All the microtextured substrates reported higher resin adhesion than the bare metal substrates and the measured adhesion strengths positively correlated with the increased surface area by laser micromachining. Therefore, the selected micromachined structures for this study do not support lower resin adhesion to metals. The microscopy analysis for periodic ripple structures revealed adhesive/cohesive failure at the interface. Circular hole observations confirmed that resin has penetrated into the microcavities, thus increasing the interfacial area available for adhesion bonding and mechanical interlocking. However, failed hexagonal hole substrates showed traces of entrapped air pockets coinciding at the hole positions but the adhesion strength was still high due to cohesive failure occurring around microcavities. Therefore, this research concludes that closed-end hole structures have the potential for air trapping at the resin-metal interface and need more exploration in different geometries with higher hole depths than what is studied during this work.

Résumé

L'adhérence de la résine époxy à la surface du métal est importante pour les industries de fabrication de composites car les pièces composites sont généralement fabriquées dans des moules métalliques. Lors de la fabrication des composites, l'adhérence de la résine sur le métal doit être faible pour faciliter le démoulage du composite durci. L'étude porte donc sur la faisabilité de l'utilisation de modifications de la topographie à l'échelle micro/nano introduites par micro- avec un laser femtoseconde (fs) pour empêcher l'adhésion de la résine époxy sur des substrats en alliage d'aluminium. Cette étude part de deux hypothèses, d'une part, les bulles d'air piégées dans les microcavités pourraient réduire la surface interfaciale et ainsi diminuer l'adhérence. D'autre part, le mécanisme de rupture adhésive serait favorisé par la présence de ces bulles d'air. La force d'adhésion a été mesurée en fonction de différentes géométries micro-usinées par laser femtoseconde sur des surfaces métalliques. Ainsi, des cavités hexagonales, des cavités circulaires et des structures ondulées périodiques ont été micro-usinées sur des substrats d'alliage d'aluminium non traités. L'angle de contact statique de la résine liquide sur les substrats métalliques à la température de durcissement a été mesuré par goniométrie. Des tests de traction ont été effectués pour mesurer la force d'adhésion. Une couche de résine époxy durcie entre deux substrats micro-usinés au laser a été utilisée pour les essais de traction. La microscopie électronique à balayage et la profilométrie à balayage laser ont été utilisées pour analyser les modes de rupture et détecter la pénétration de la résine dans les microcavités. Tous les substrats microtexturés ont présenté une adhérence à la résine supérieure à celle des substrats métalliques non traités et il y a une corrélation positive entre les forces d'adhérence mesurées et l'augmentation de la surface par micro-usinage laser. Par conséquent, les structures micro-usinées sélectionnées pour cette étude ne permettent pas de réduire l'adhérence de la résine aux métaux. L'analyse microscopique des structures ondulées périodiques a révélé une rupture adhésive/cohésive à l'interface. Les observations des substrats à cavités circulaires ont confirmé que la résine avait pénétré dans les microcavités, augmentant ainsi la zone interfaciale disponible pour l'adhésion et l'emboîtement mécanique. Cependant, les substrats à cavités hexagonales ayant rompu présentaient des traces de poches d'air piégées coïncidant avec les positions des cavités. Cependant, les forces d'adhésion étaient encore élevées car il s'est produit une rupture cohésive autour des microcavités. Ainsi, cette étude abouti à la conclusion que les structures à cavités fermées ont le potentiel de piéger de l'air à l'interface résine-métal. Elle doivent donc continuer d'être étudiées en changeant la géométrie et/ou la profondeur des cavités. Il serait par exemple intéressant de mener une étude avec des cavités plus profondes.

Acknowledgment

I am grateful to my mother, father, and little brothers for supporting me in realizing my intentions to join McGill as an MSc student in the research group that I wanted to be a part of. I would like to appreciate the support from my lovely roommates (Shannon, Tharushi, and Hyun) and my best friends back home, who have been a great pillar of strength throughout the past two years.

I would like to extend my acknowledgement to Manuela Talbot from Airbus Defence and Space, Germany for the support in providing raw materials for this research project. I am grateful for the enormous support and understanding from my supervisor Prof. Anne Kietzig who has opened doors for me to improve in various aspects ever since I started my MSc. Also, I greatly acknowledge my supportive lab members, Dr. Damon Aboud, Dr. Michael Wood, Nithin Joy, Yuhua Liu, Zainab Adedipe, Gianluca Zeppetelli, Breno Sequeira, and Anas Esbel. I would like to thank Gianluca Zeppetelli, Florian Dano, Nithin Joy, Shannon Constantine and Jinani Sooriyaarachchi for the assistance in proofreading this thesis. Finally, I am grateful for the McGill University for all the support and opportunities during my master's studies.

Table of contents

Abstract.....	ii
Résumé.....	iii
Acknowledgment.....	iv
Table of contents.....	v
List of figures.....	viii
List of tables.....	xiii
List of abbreviations	xiv
1 Introduction	1
2 Literature review.....	3
2.1 Femtosecond (fs) laser micromachining	3
2.1.1 Femtosecond laser and solid-matter interaction	3
2.1.2 Laser inscribed structures	5
2.1.3 Laser induced structures	6
2.1.4 Laser micromachining influence on the surface chemistry	6
2.2 Surface wetting principles.....	7
2.3 Liquid resin wettability and resulting adhesion	11
2.4 Adhesive/ Cohesive failure at a solid-solid interface.....	13
2.5 Laser modified metal tool surfaces for resin wetting and de-wetting properties	15
2.6 Adhesion strength tests.....	17
3 Objectives	19
4 Materials and characterization techniques.....	20
4.1 Materials.....	20
4.2 Instrumentation and data analysis software	21
4.2.1 Laser system.....	21
4.2.2 Tensile testing	22
4.2.3 Surface characterization.....	22

5	Adhesion strength test development and resin leaking	24
5.1	Resin leaking	25
5.2	Finalized tensile test setup and sample preparation procedure for tensile testing	32
6	Optimization of required surface geometries	34
6.1	Thermodynamic calculations	34
6.2	Liquid resin surface tension and wettability characterization	39
6.2.1	Preliminary results of contact angle measurement	39
6.2.2	Finalized contact angle measurement procedure	41
6.2.3	Epoxy resin contact angle results on smooth metal substrates	43
6.3	Selection of desired surface structures	47
7	Analysis of laser micromachined metal sample surfaces	52
7.1	Laser micromachining optimization	52
7.1.1	Cylindrical hole micromachining optimization	52
7.1.2	Hexagonal hole micromachining optimization	54
7.1.3	Periodic nanostructures micromachining optimization	56
7.2	Surface topography characterization of laser micromachined samples	58
7.3	Results and discussion.....	61
7.3.1	Adhesion strength at the metal-resin interface.....	61
7.3.2	Surface characterization of failed surfaces	64
8	Conclusions	71
9	Future work.....	72
10	Original contributions	73
11	References.....	74
12	APPENDIX.....	80
	APPENDIX I: Preliminary resin contact angle results	80
	APPENDIX II: Optimization code for cylindrical holes	81
	APPENDIX III: Optimization code results	86

APPENDIX IV: Increased surface area calculation after laser micromachining.....	87
APPENDIX V: Increased surface area calculation after laser micromachining.....	89

List of figures

Figure 1 Gaussian fluence profile of the laser beam. D: diameter of the ablated area, F_0 : Peak fluence, F_{th} : Threshold fluence. Reprinted with permission from reference [21].	4
Figure 2 SEM images for fs laser inscribed structures on copper substrate a) pyramid structures b) columnar structures with magnified views. Reprinted with permission from reference [16] under © 2014 (CC BY 4.0) by MDPI.	5
Figure 3 SEM images for fs laser inscribed structures a) square pillars b) parallelogram structures in a hexagonal order c) grooves in circular arrangement d) hole structures. Reprinted with permission from reference [16] under © 2014 (CC BY 4.0) by MDPI.	5
Figure 4 SEM images of LIPSS structures a) low spatial frequency ripple-like LIPSS on stainless steel. Adapted with permission from reference [28] b) Triangular LIPSS on stainless steel. Adapted with permission from reference [25].	6
Figure 5 a) Contact angle on a smooth surface b) Wenzel wetting state c) Cassie-Baxter wetting state	7
Figure 6 a) CB wetting state b) Depinning, Intermediate wetting state while CB → Wenzel transition occurs, red arrows show the three-phase contact line movement [36] c) Sagging, Pressure elements present in the three phase system [35]	8
Figure 7 CB to Wenzel transition mechanism A) the sagging fluid front touches the bottom of the cavity B) the three-phase contact line advance along the sidewalls after depinning. Reprinted from reference [35].	9
Figure 8 a) Periodic pillar microstructures (cross section in grey) b) A unit cell of the periodic structure where A_c : unit cell area, A : solid-liquid interface area, L -perimeter of the pillar/hole structure. Adapted with permission from reference [36] under © 2005, American Chemical Society.	10
Figure 9 Sessile drop images of melted polypropylene on polished steel at 200 °C at different times a) in N ₂ b) in air. Reprinted with permission from reference [40] under © 2016, Wiley Periodicals, Inc.	11
Figure 10 Summary of rheological property and molecular weight change during cure of epoxy resins. Reprinted with permission from reference [38] under © 1993, Springer Science & Business Media Dordrecht.	12
Figure 11 epoxy/oxirane functional group	12

Figure 12 Crack propagation a) purely adhesive b) purely cohesive c) hybrid adhesive-cohesive failure. Reprinted with permission from reference [46] with © 2020, Scrivener Publishing LLC.	14
Figure 13 a) SEM image of a laser machined steel surface with microprotrusion structures. b) Contact angle change of hydrophobized laser machined samples with different microprotrusion heights (Microprotrusion diameter and spacing is 100 μm). Adapted with permission from reference [50] under © 2018, Elsevier B.V. All rights reserved.	15
Figure 14 a) SEM image of the mould surface topography with scanning speed 500 mm/s and line pitch 0.05 mm b) Resulting CFRP surface topography. Adapted with permission from reference [51] under © 2019, Elsevier.	16
Figure 15 Illustration of a test sample for single lap shear test	17
Figure 16 Schematic of an ASTM C633 test setup for a surface coating adhesion strength test	17
Figure 17 Schematic explaining the research hypotheses a) Cassie-Baxter wetting b) adhesion failure promoted by entrapped air bubbles in the cured resin matrix	19
Figure 18 a) Raster scanning for LIPSS b) raster scanning for hexagonal holes c) percussion drilling for microscale holes	21
Figure 19 Initial tensile test set up a) 3D view b) 2D side view (the resin layer is not in actual scale with the other components)	24
Figure 20 a) Illustration of a laser micromachined substrate sample b) Random spreading of same amount of resin on Al alloy samples with identical surface topology	25
Figure 21 a) laser micromachined area surrounded by an adhesive tape to prevent liquid resin flow beyond the laser patch b) Resin patch cured with adhesive tape boundary on a bare metal surface c) Resin patch cured on a laser micromachined metal sample surface with adhesive tape boundaries. Yellow contour lines mark the resin areas.	26
Figure 22 Resin layer cured with PDMS-based release agent gel applied on the boundary of a bare Al alloy sample	27
Figure 23 Resin layer cured on circular hole laser micromachined Al alloy sample after the entire surface is lauric acid treated	28
Figure 24 Resin layer cured on circular hole laser micromachined Al alloy sample after the non-laser machined areas are lauric acid treated	28
Figure 25 Resin leaking in an Al alloy sample with an adhesive tape carefully applied just around the boundary of the laser micromachined region	30
Figure 26 Resin layer cured with silicone glue boundaries a) side view	30

Figure 27 Illustration of a plastic ring mold clamped onto a laser-machined sample	31
Figure 28 Finalized tensile test set up for adhesion strength test a) Top substrate with T holder unit b) Bottom substrate with T holder unit c) actual image of the setup clamped to the tensile tester.....	32
Figure 29 A tensile test sample before mounting on the test set up (A resin layer is cured in between the overlapping area of the orthogonally placed substrates with the same surface modifications.....	33
Figure 30 Unit cell (marked in red dash lines) considered for cylindrical hole structures.....	35
Figure 31 Unit cell (marked in red dash lines) considered for hexagonal hole structures.....	35
Figure 32 Example of a resin droplet image used for the surface tension calculation just before falling off from the needle tip	39
Figure 33 Time Vs Contact angle change for R2 resin system on bare Al alloy surface (Al) and release coating applied Al surface (RC)	40
Figure 34 Schematic of the heating stage and the sample during a contact angle measurement experiment.....	41
Figure 35 a) Image of the heating stage with metal sample and thermocouples attached to it during the contact angle measurement experiment b) Averaged heating curves used for the contact angle measurements on bare Al alloy surface (Al) and release coating applied surface (RC).....	42
Figure 36 Final stabilized contact angles at 60 °C for bare aluminum alloy samples (Al) and with release coating applied aluminum alloy samples (RC).....	43
Figure 37 Temperature Vs R2 resin Average Contact Angle for aluminum alloy samples with and without release coating.....	44
Figure 38 R2 resin droplet top view images at the end of the contact angle experiments for a) a bare aluminum alloy sample, red arrow: polished line direction b) a release coating applied aluminum alloy sample	45
Figure 39 Side view of resin droplets on aluminum alloy surface a) bare aluminum alloy surface b) release coating applied aluminum alloy surface (CA - Contact Angle)	46
Figure 40 The summarized flowchart of the thermodynamic calculations followed in the python code	49
Figure 41 Confocal microscopy image of CY_P3 structures with the height profile of micro holes	54

Figure 42 Raster scans with different laser parameters with 1 over scan a) 34.8 mW, 1 kHz, 70 PPS b) 184.6 mW, 1 kHz, 700 PPS c) 51.3 mW, 1 kHz, 70 PPS and d) 34.8 mW, 1 kHz, 70 PPS with 10 over scans	55
Figure 43 Different laser settings tested for LIPSS. Linearly polarized laser beam a) 27.1 mW, 43 PPS, 90% b) 33.4 mW, 43 PPS, 90% c) 27.1 mW, 9 PPS, 50%. Circularly polarized laser beam with 43 PPS, 90% d) 27.1 mW e) 33.4 mW f) 38.6 mW	57
Figure 44 SEM images obtained for different laser micromachined patterns a) CY_P1 b) CY_P2 c) CY_P3 d) HX_P2	58
Figure 45 Confocal profilometry images obtained for different laser micromachined patterns a) CY_P1 b) CY_P2 c) CY_P3 d) HX_P2 (example dimensional measurements are presented)	59
Figure 46 Stress curves reported for Al alloy substrates with different surface topographies	61
Figure 47 Average maximum breaking stress data obtained for different substrates with comparison to increased surface area	62
Figure 48 Stress at the first step failure obtained for different substrates with comparison to increased surface area	63
Figure 49 Images of a bare aluminum alloy sample substrates after failure. Yellow arrows: air bubbles.	64
Figure 50 LIPSS failed bottom substrate a) image b) SEM, failed top substrate c) image d) SEM, e) SEM of LIPSS surface before resin casting. Yellow arrows: air bubbles.	65
Figure 51 L_LIPSS failed bottom substrate a) image b) SEM, failed top substrate c) image d) SEM, e) SEM of L_LIPSS surface before resin casting. Yellow arrows: air bubbles.	65
Figure 52 CY_P1 a) failed bottom substrate image b) & c) SEM d) confocal, e) failed top substrate image f) & d) SEM i) confocal. Red arrows: air bubbles.	66
Figure 53 CY_P2 a) failed bottom substrate image b) & c) SEM d) confocal, e) failed top substrate image f) & d) SEM i) confocal. Red arrows: air bubbles.	67
Figure 54 CY_P3 a) failed bottom substrate image b) & c) SEM d) confocal, e) failed top substrate image f) & d) SEM i) confocal. Yellow arrows: locations of cohesive failure. Red arrows: air bubbles.	67
Figure 55 HX_P2 a) failed bottom substrate image b) & c) SEM d) confocal, e) failed top substrate image f) & d) SEM i) confocal	68
Figure 56 Failed HX_P2 interfaces a) & b) Confocal 3D view image at an air bubble entrapped location (white dashed line: traces of the hexagon on counter surface), c) & d) magnified SEM	

images of air bubble entrapped hexagonal hole locations (red dashed lines: a belt of redeposited nanoparticles around the hexagon hole entrance)	70
Figure 57 The model used to estimate the surface area of the ripple structure. Closely packed ridges with parabolic cross section were assumed.....	87
Figure 58 Example a) CY_P1 b) CY_P2 c) CY_P3 depth profile from confocal d) Model used for a circular hole for the estimation of surface area. A conical shape was assumed.....	88

List of tables

Table 1 Material specifications for the resin system	20
Table 2 Chemical layer barriers applied to prevent resin leaking	27
Table 3 Physical barriers applied to prevent resin leaking	30
Table 4 Equations derived for a unit cell of hexagonal and cylindrical hole patterns considered for this study	35
Table 5 Selected structural geometries from the optimization process	50
Table 6 Laser inscribed surface textures selected for the adhesion strength testing campaign	51
Table 7 Cylindrical hole percussion drilling optimization on Al alloy (AA6061) metal	53
Table 8 fs laser raster scanning optimization on Al alloy (AA6061) metal	55
Table 9 Laser machining optimization settings tested for LIPSS	56
Table 10 Characteristic dimensions measured for laser textured substrates.....	60
Table 11 One-tailed T-test results for maximum breaking stress values reported	63
Table 12 Surface area calculations for LIPSS and L_LIPSS samples	87

List of abbreviations

USD	United States Dollar
PPS	Pulse Per Spot
LIPSS	Laser Induced Periodic Surface Structures
CB	Cassie-Baxter
CFRP	Carbon Fiber Reinforced Polymer
ASTM	American Society for Testing and Materials
RC	Release Coating
USA	United States of America
PVT	Position-Velocity-Time
SEM	Scanning Electron Microscopy
EDX	Energy Dispersive X-ray spectroscopy
PDMS	Polydimethylsiloxane
CA	Contact Angle
CY	Cylindrical holes
HX	Hexagonal holes

1 Introduction

Advanced composite manufacturing in the aerospace industry has grown to be a huge market owing to the continuous improvement of new composite technologies. According to the market insights, in 2020, the global aerospace composites market size exceeded 10 billion USD and is expected to grow up to 16 billion USD by 2027 [1]. A composite is a combination of two or more materials with no chemical reactions in between and has superior performance to individual materials. Composites contain two components which are the reinforcement phase and the continuous phase. Carbon fiber and glass fibers are common reinforcement materials in aerospace applications whereas the continuous phase is a material matrix of polymer, metal, or ceramic. The matrix phase holds the reinforcing material in the composite [2].

Composites are cured inside molds to get the required component shape. Metallic molds are advantageous in composite fabrication because of their high strength and durability. While steel, aluminum, and Invar metal molds are primarily used within the aerospace industry. Epoxy based resin systems are popular matrix materials because of the high temperature resistance and processability characteristics. Resin compounds typically used as the composite matrix have a high affinity to metals. Hence, composites tend to adhere well to the mold and demolding of the cured component becomes challenging.

Adhesion force between two surfaces results from one or more of the following types of interactions, van der Waals forces, electrostatic forces, chemical bonding, capillary forces, hydrogen bonding, mechanical interlocking, diffusion, etc. In the case of a smooth metal surface in contact with a highly wetting liquid such as resin, intermolecular bond formations are dominated. Further, the extent of interfacial bond interactions depends on the actual contact area of the two materials at the interface. Therefore, liquid resin wettability on metal directly affects the cured resin adhesion on the mold.

Barrier/release coatings are used to avoid above-mentioned demolding issue [3, 4]. Release agents are materials that facilitate demolding of a fabricated component from a mold. It is in the form of either a solid film or a chemical solution which deposits as a thin barrier coating on the mold surface. Release agent materials contain highly stable functional groups which reduce the intermolecular bond formation. Moreover, often a release coating creates a smoother surface than bare metal, which prevents mechanical interlocking as well as reduces the solid-

liquid contact area available for adhesion bond formation [4]. Some popular mold release agents are fluoro-polymer based systems, silicone based systems and polysiloxanes [5].

Even though release agents are heavily used in the industry, they carry certain drawbacks. Release coating residue tends to contaminate the composite component's surface. In most aerospace applications, this is disadvantageous. Contamination free surfaces are essential for further manufacturing processes such as plating, painting or bonding with adhesives [6]. Furthermore, aerosol-based release agents require well-ventilated operational spaces due to aerosol particles and volatile organic compounds used as the solvent medium. Therefore, release coating usage carries an environmental and a health burden [3]. To address this, the industry focus has been directed towards using release agent solutions with zero/reduced volatile organic matter content, developing new barrier coating materials or efficient coating processes [7-10] which however, often comes with the downside of poor performance [5]. Still, the contamination issue is yet to be addressed.

With all the above-mentioned factors, it is important to notice that even a reduction in the amount of release agent usage has a considerable positive impact on a sustainable production process. Hence, the motivation of this study was to explore the possibility of replacing the active role of release coatings with a passive surface. Micro/nano scale surface structures fabricated from laser micromachining have the potential to modify surface wettability and adhesion, attributed to correct surface features [11-13]. This project focused on understanding liquid resin wettability on metals and identifying the factors promoting adhesive failure at the cured resin-metal interface in the presence of a femtosecond laser textured mold.

2 Literature review

This literature review summarizes the potential of femtosecond laser micromachining as a surface wettability modification technique, relevant established surface wettability science, resin curing mechanism and adhesive/ cohesive failure mechanisms which were important background topics for this research project.

2.1 Femtosecond (fs) laser micromachining

2.1.1 Femtosecond laser and solid-matter interaction

Fabrication methods commonly used for textured surface topographies are lithography, electrodeposition, electro etching, laser machining, and plasma treatments, etc. Among several fabrication techniques, laser micromachining remains a facile and scalable process suitable for industrial scale applications [14].

Laser-matter interaction causes material ablation, introducing micro/nano features to the surface under certain laser characteristics. Particularly, ultrashort pulsed laser (femtosecond or picosecond) have received tremendous attention since 1994 [15] because the very short period of interaction of high intensity laser pulses with the material is unique compared to the longer pulses. For example, the shorter interaction time of femtosecond laser pulses, limits heat conduction to the surrounding incident area, resulting in a very small to no heat affected zone. Hence femtosecond laser machining provides high precision and control over the machined structural features on a material surface [16, 17].

The characteristic parameter of fs lasers is the pulse duration (also known as pulse width), which is in the femtosecond range (< 1 ps). Different micro/nano structures are achievable through micromachining by varying a range of laser parameters including laser fluence, wavelength (λ_{laser}), pulse duration, beam polarization, scan velocity (v), repetition rate (f) and number of over scans. Externally to laser system parameters, incident angle, substrate surface roughness, substrate composition, environmental composition, and humidity also affect the resulting micromachined structures [16, 18-20]. Therefore, in summary, the resulting surface features depend on the fs laser parameters, substrate characteristics, and the machining environmental conditions.

The ablation threshold is the primary parameter that is considered when laser micromachining a material. It is defined as the minimal laser fluence necessary to ablate material from the bulk

material surface. Most pulsed laser systems have a Gaussian beam intensity profile. Accordingly, the fluence profile has the same Gaussian nature as illustrated in Figure 1.

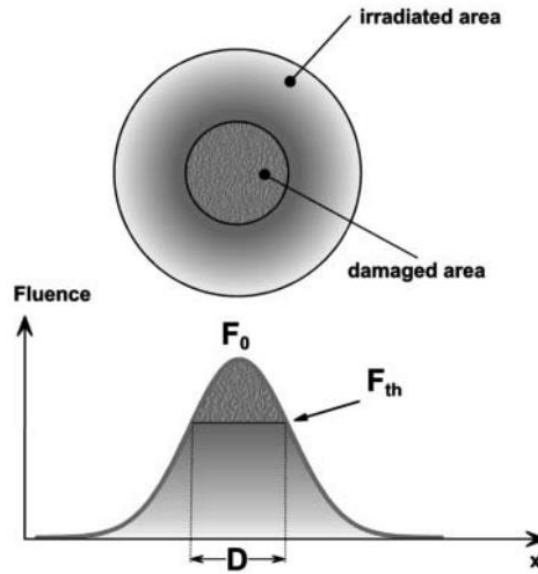


Figure 1 Gaussian fluence profile of the laser beam. D : diameter of the ablated area, F_0 : Peak fluence, F_{th} : Threshold fluence. Reprinted with permission from reference [21].

The ablation threshold is calculated using Equation 1 where the diameter (D) of the ablated area is obtained experimentally [21] and the peak fluence (F_0) is calculated from Equation 2. ω_0 is the theoretical beam diameter (Equation 3) while l and d denote lens focal length and incoming beam diameter to the focusing lens. Peak fluence and the number of pulses per spot are most commonly used when reporting laser settings in the literature. Equation 4 & Equation 5 detail how the PPS is calculated based on ω_{eff} , ϕ_{line} , and t , which correspond to effective beam diameter, scanning line overlap and scanning time, respectively. The PPS equation changes depending on the machining technique. For example, Equation 4 is derived for raster scanning of the laser beam on a substrate whereas, Equation 5 is derived for steady laser beam incident on a substrate which is known as percussion drilling.

$$2D^2 = \omega_0^2 \ln \left(\frac{F_0}{F_{th}} \right) \quad \text{Equation 1}$$

$$F_0 = \frac{8P}{\pi \omega_0^2 f} \quad \text{Equation 2}$$

$$\omega_0 = \frac{4l\lambda_{laser}M^2}{\pi d} \quad \text{Equation 3}$$

$$PPS_{raster} = \frac{\omega_0^2 f}{v\omega_{eff}(1 - \phi_{line})} \quad \text{Equation 4}$$

$$PPS_{drilling} = ft$$

Equation 5

The outcome of fs laser machining of surface textures is distinguished under two categories as laser inscribed structures and laser induced structures.

2.1.2 Laser inscribed structures

Laser machined surface features with dimensions in the same range or larger than the effective laser beam spot size are defined as laser inscribed structures. Since they depend on the material ablation and the trajectory of the laser relative to the substrate surface, inscribed structures are produced in a wide range of geometries. Figure 2 & Figure 3 are examples of different femtosecond laser inscribed structures on a copper substrate [16]

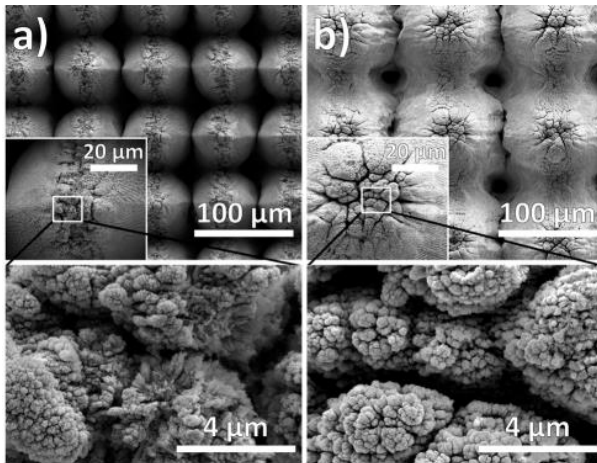


Figure 2 SEM images for fs laser inscribed structures on copper substrate a) pyramid structures b) columnar structures with magnified views. Reprinted with permission from reference [16] under © 2014 (CC BY 4.0) by MDPI.

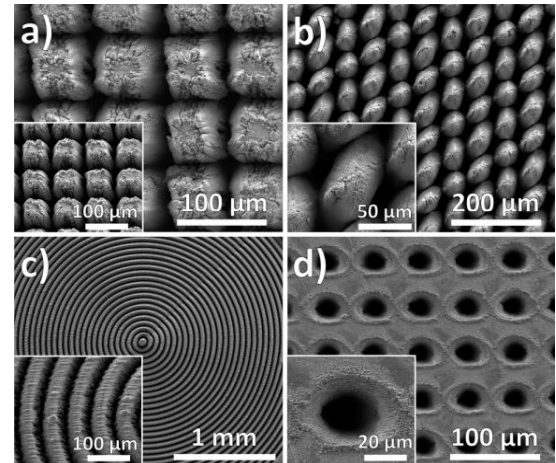


Figure 3 SEM images for fs laser inscribed structures a) square pillars b) parallelogram structures in a hexagonal order c) grooves in circular arrangement d) hole structures. Reprinted with permission from reference [16] under © 2014 (CC BY 4.0) by MDPI.

Furthermore, ultra short, pulsed laser machining fabricates hierarchical micro/nano scale surfaces in a single machining step. Enlarged views of such hierarchical structures are shown in Figure 2. Inscribed structures are popular for surface functionality modifications beneficial to various applications, including anti-adhesion of fluids such as water, oil, blood etc. [11, 13, 22].

2.1.3 Laser induced structures

Surface features smaller than the effective laser beam diameter are defined as laser induced structures. For example, linearly polarized femtosecond laser irradiation on metals creates ripple-like periodic modulations on the surface. These are known as laser induced periodic surface structures (LIPSS). Metals typically report low spatial frequency LIPSS with a period similar to or slightly shorter than the laser wavelength, and the ripple orientation perpendicular to the laser polarization [23]. Similar to ripple-like structures, triangular modulations are formed using circularly polarized laser beams [24, 25]. Examples for ripples and triangular LIPSS are shown in Figure 4. Laser induced structure formation allows surface texturing of finer features (in the submicron scale) than inscribed structures. LIPSS formation depends on various laser parameters such as laser wavelength, fluence, number of pulses, and polarization. [23, 26, 27].

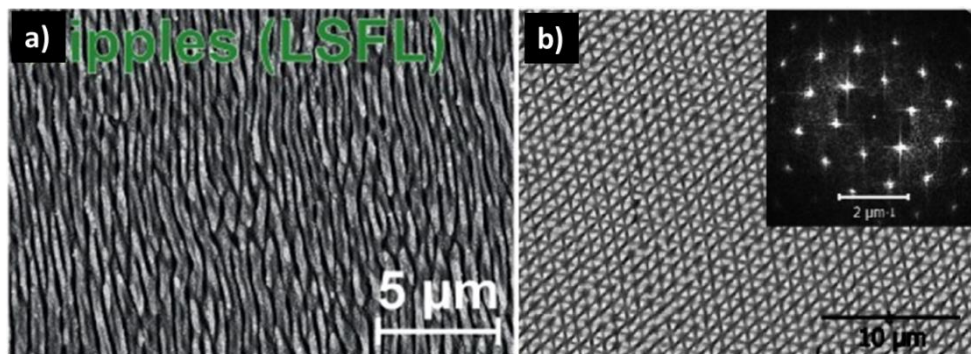


Figure 4 SEM images of LIPSS structures a) low spatial frequency ripple-like LIPSS on stainless steel. Adapted with permission from reference [28] b) Triangular LIPSS on stainless steel. Adapted with permission from reference [25].

2.1.4 Laser micromachining influence on the surface chemistry

The wettability transition of laser micromachined metal samples with time has been reported in the literature, where the contact angle eventually increases and reaches a plateau value [29]. The wettability transition without a surface topology change is attributed to the surface chemistry change. Several hypotheses are debated to explain this hydrophilic to hydrophobic wettability transition of metal samples. Some researchers attribute this wettability transition to the adsorption of organic molecules on the laser machined surface [30, 31].

Post-processing conditions, including exposure to different liquid or gaseous environments and heat treatments, have been revealed to change the surface chemistry, thus accelerating the wettability transition process [20, 32, 33]. For example, one study has reported achieving superhydrophobic surfaces on laser machined aluminum samples after immersing the sample in a 5 mM lauric acid-ethanol solution for 30 minutes. Then the sample was taken out, rinsed

with ethanol, and dried for 15 minutes in an oven at 80 °C temperature [30]. A recent publication from our group further confirms that lauric acid contributes to the adsorption of carbonaceous compounds onto a laser irradiated Cu surface [32]. Nevertheless, the desired surface topography and chemistry for reduced surface adhesion properties requires an understanding of the wettability of resin liquids on metal.

2.2 Surface wetting principles

The wettability of a surface depends not only on the surface chemistry but also on the surface roughness in nano/micro scale and on the properties of the wetting material. For example, the superhydrophobicity of a lotus leaf is achieved by combining a hydrophobic wax layer with air-trapping nano/micro textures. Air-trapping caused by tiny surface features reduces the water contact area with the solid, allowing water droplets to readily roll off the leaves [12, 34, 35].

For an ideally smooth, chemically homogeneous surface, liquid wettability is described by a force balance as formulated in Young's equation (Equation 6).

$$\gamma_{sa} = \gamma_{sl} + \gamma_{la}(\cos\theta) \quad \text{Equation 6}$$

The value θ is the contact angle on an ideally smooth surface as represented in Figure 5a. The surface tension is represented by γ while s, l, a denote the solid, liquid, and air phases, respectively. Surface tension or surface energy is defined as the free energy change, when the surface area of a medium is increased by a unit area and is determined by the intermolecular forces within the material. For a real surface, Equation 6 is not valid because of microscale roughness and chemical inhomogeneity on surfaces. The Wenzel and Cassie-Baxter (CB) equations are commonly used to approximate the liquid wettability of rough surfaces. The Wenzel and CB wetting of a liquid droplet are illustrated in Figure 5b and Figure 5c, respectively.

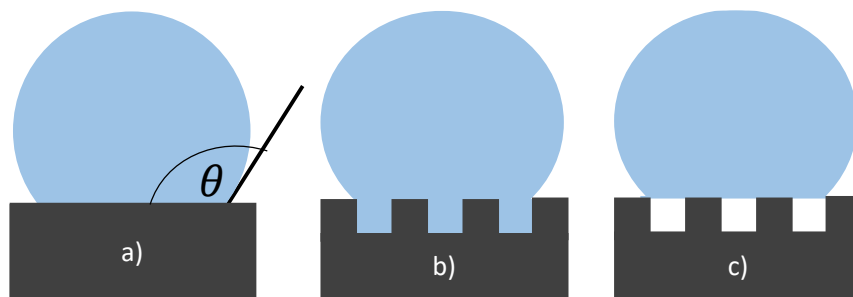


Figure 5 a) Contact angle on a smooth surface b) Wenzel wetting state c) Cassie-Baxter wetting state

The contact angle of the Wenzel state is represented in Equation 7 as θ_w where r is the roughness factor defined as the ratio between the actual surface area to the projected surface area. Equation 8 represents the contact angle of the CB state (θ_{CB}) where f denotes the solid surface fraction at the interface.

$$\cos\theta_w = r (\cos\theta) \quad \text{Equation 7}$$

$$\cos\theta_{CB} = f (\cos\theta) - 1 + f \quad \text{Equation 8}$$

In the CB state, the liquid droplet sits on a solid-air heterogeneous surface. There are trapped air pockets at the liquid-solid interface which contribute to the lower adhesion of liquid droplets to the solid surface. Among Wenzel and CB, the preferred wetting state for a system depends on Gibb's free energy. A system will attempt to reach a minimum energy state, either a local minimum (a metastable state) or a global minimum. The most stable wetting state (global energy minimum) varies depending on the micro/nanoscale surface roughness. The change in Gibb's energy (ΔG) from one state to another is calculated by Equation 9 where ΔA represents newly formed or destroyed surface areas.

$$\Delta G = \gamma_{la}\Delta A_{la} + \Delta A_{sl}(\gamma_{sl} - \gamma_{sa}) \quad \text{Equation 9}$$

In the case of a CB metastable state, a CB to Wenzel transition occurs upon the application of external forces on the liquid. An energy barrier needs to be overcome for a Cassie-to-Wenzel transition. Therefore, higher transition energy barriers allow more robust liquid repellency because there is more resistance for liquid penetration into microcavities. The energy barrier to overcome for a Cassie-to-Wenzel transition (E_{gap}) is calculated by Equation 10 where η is the pillar slenderness ratio (expressed in Equation 11), H pillar height, L perimeter, and A_{sl} solid to liquid surface area at the Cassie state [36]. This equation is obtained by considering the excess energy associated with wetting the pillar/hole side walls while the liquid phase moves into feature valleys (Figure 6b).

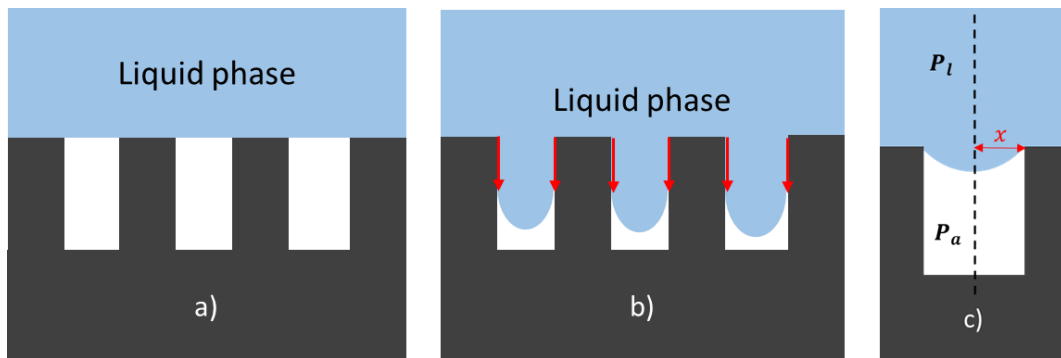


Figure 6 a) CB wetting state b) Depinning, Intermediate wetting state while CB \rightarrow Wenzel transition occurs, red arrows show the three-phase contact line movement [36] c) Sagging, Pressure elements present in the three phase system [35]

Interestingly, Equation 10 & Equation 11 show that higher pillars/ deeper holes cause greater transition barriers, implying that such textures support more robust CB wetting states.

$$E_{gap} = -\eta\gamma_{la}f\cos\theta \quad \text{Equation 10}$$

$$\eta = \frac{HL}{A_{sl}} \quad \text{Equation 11}$$

Apart from the energy-based explanations, pressure effects existing between the liquid phase (P_l) and the air phase inside microcavities (P_a) constitutes another approach to describe the robustness of a CB wetting state. The pressure difference ($\Delta P = P_a - P_l$) is determined by Laplace's law (Equation 12) where K is the radius of curvature of the liquid front.

$$\Delta P = 2\gamma_{la}K \quad \text{Equation 12}$$

When the pressure difference becomes higher than the critical breakthrough pressure (P_{break}), liquid penetrates into the cavity and results in the loss of the CB wetting state which can occur in two scenarios. A high enough hydrostatic pressure can lead to sagging of the fluid front until it touches the bottom of the cavity (see Figure 7A). Or else, depinning of the three-phase contact line causes the fluid front to move along the side walls of the cavity and eventually hit the bottom as illustrated in Figure 7B. Therefore, deep holes ensure the robustness of the CB state.

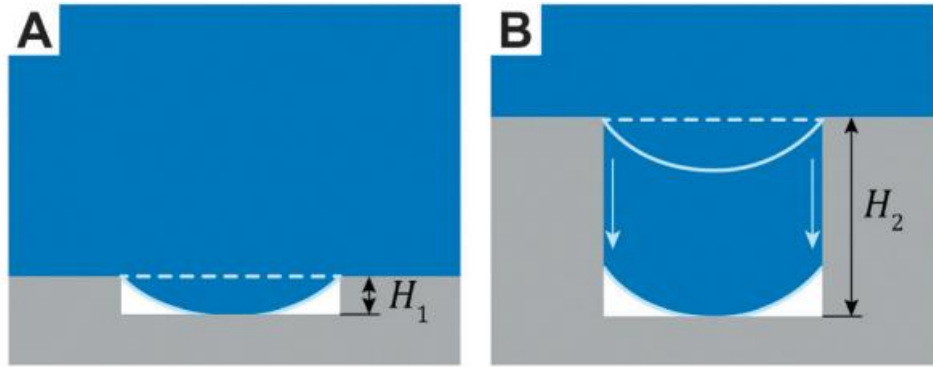


Figure 7 CB to Wenzel transition mechanism A) the sagging fluid front touches the bottom of the cavity B) the three-phase contact line advance along the sidewalls after depinning. Reprinted from reference [35].

Equation 13 is the simplified version of the critical pressure for circular holes with radius x , where $K (= \frac{1}{x})$ has reached the minimum possible curvature [35].

$$P_{break} = \frac{2\gamma_{la}}{x} \quad \text{Equation 13}$$

Figure 8C displays a periodic microstructure of pillars with the cross section A . A unit cell of the periodic microstructure is defined in Figure 8D. The derivation of a generalized breakthrough pressure equation for a unit cell is essential for thermodynamic estimations of wettability of a three-phase system.

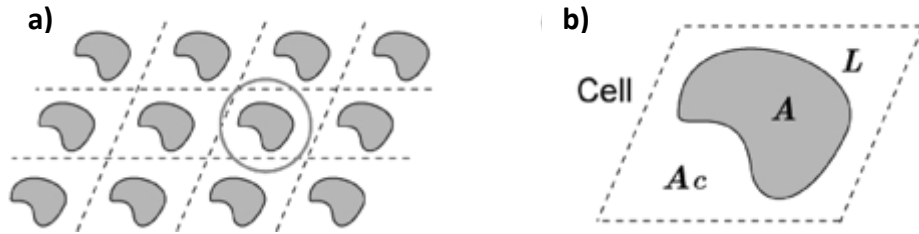


Figure 8 a) Periodic pillar microstructures (cross section in grey) b) A unit cell of the periodic structure where A_c : unit cell area, A : solid-liquid interface area, L -perimeter of the pillar/hole structure. Adapted with permission from reference [36] under © 2005, American Chemical Society.

When considering the pressure induced force on the liquid-air interface and corresponding surface tension along the three-phase contact line at the side walls, Equation 14 is generated at equilibrium just before breakthrough. The same is converted to Equation 15, since $f = A/A_c$. Then λ is defined as A/L and therefore, Equation 16 is derived for calculation of breakthrough pressure in a unit cell [36].

$$P_{break}(A_c - A) = -\gamma_{la}L\cos\theta \quad \text{Equation 14}$$

$$\Delta P(1 - f) = \frac{-\gamma_{la}L\cos\theta}{A_c} \quad \text{Equation 15}$$

$$\Delta P = -\frac{\gamma_{la}f\cos\theta}{(1 - f)\lambda} \quad \text{Equation 16}$$

Considering the topics of this thesis, resin solutions have a comparatively low surface tension. Although studies carried out specifically for resin repelling surfaces are scarce, many superomniphobic surface designs investigate the stability of CB wetting states for low surface tension fluids such as organic solvents (surface tension below 25 mN/m), oil, blood etc. In such studies, re-entrant structures with overhanging surface features [13, 35] and porous metal structures [34] have shown promising results.

In the literature, some uncured liquid epoxy resin systems have been reported to have surface tensions in the range of 36 - 41 mN/m at 24 °C ambient conditions. However, they have shown negative linear correlation to temperature increase [37]. This information leads concerns regarding temperature dependence of liquid resin wettability.

2.3 Liquid resin wettability and resulting adhesion

Liquid wettability on a solid is characterized using its contact angle. Water contact angle measurement protocols are well established in the field of wetting investigations. However, resin solutions are viscous fluids with high sensitivity to temperature [37, 38], and performing contact angle measurements for highly viscous liquids has been challenging compared to water contact angle measurements due to viscosity dependent wetting dynamics. A study performed on the wetting dynamics of varying liquid viscosity has revealed that more viscous liquids take more time to reach equilibrium (longer inertial wetting time) but that the spreading radius and resulting base diameter at equilibrium are alike for every liquid that was tested with different viscosities [39]. However, it is important to note that these results are specific to a water-glycerol mixture and may differ for another polymer solution.

Two studies from Zitzenbacher et al. report on the sessile drop contact angles measured for molten polymers on metal substrates inside a heating chamber [40, 41]. The authors report that a high contact angle corresponds to high viscosity of polymer melts. Further, they observed higher wettability caused by lower polymer viscosity at elevated processing temperatures than at ambient conditions. A decrease in contact angle with time (Figure 9) at a constant temperature of 200 °C for polymer melts was also reported [40]. These data highlight the importance of studying wettability at the relevant processing temperatures.

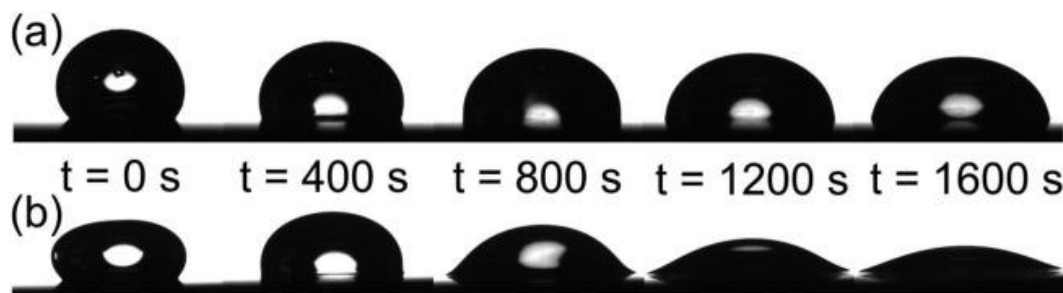


Figure 9 Sessile drop images of melted polypropylene on polished steel at 200 °C at different times a) in N2 b) in air. Reprinted with permission from reference [40] under © 2016, Wiley Periodicals, Inc.

In contrast to thermoplastic polymers investigated in the aforementioned study, resin systems used in composite manufacturing are thermosets which also undergo a compositional change during solidification which is further elaborated on in the following.

Curing of a thermoset polymer is characterized by the crosslinking of molecules when the polymer matrix transforms to a solid state from a liquid state. This involves a significant variation in viscosity during the process. Important parameters to consider in resin curing are the curing temperature and gelation point. Once the resin is mixed with the hardener or the

curing agent, the polymerization is initiated, and larger molecules start forming. Then highly branched molecules start forming as curing progresses. Once the branched network spreads throughout the sample and no soluble molecules are available anymore, the gelation point is reached [42]. Figure 10 contains a detailed representation of the rheological properties and molecular structure changes of a crosslinking polymer during the curing process. The horizontal axis (X_e) represents conversion, which describes the extent of the crosslinking reaction. The gelation point is noted as $X_{e\text{gel}}$ in the Figure 10. Once the soluble molecule fraction (w_s – soluble molecules weight fraction) goes to zero and gel fraction (w_g – crosslinked network weight fraction) goes to 1, the resin is considered fully cured [38].

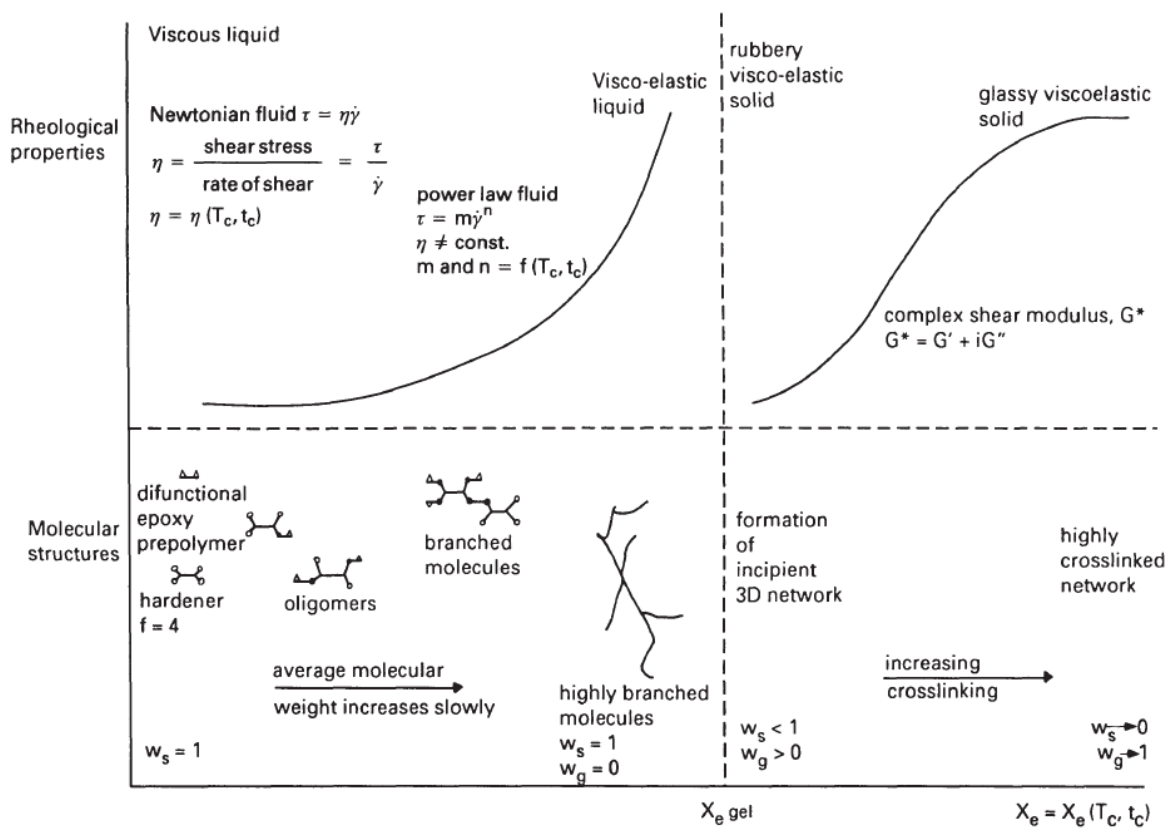


Figure 10 Summary of rheological property and molecular weight change during cure of epoxy resins. Reprinted with permission from reference [38] under © 1993, Springer Science & Business Media Dordrecht.

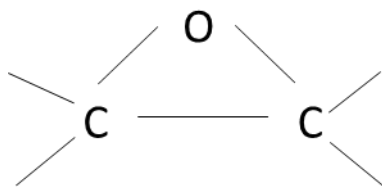


Figure 11 epoxy/oxirane functional group

Metallic materials such as Invar, steel, aluminum alloys as well as composite materials have been used as mold materials in the aerospace industry. Molds made out of composites are desirable when high accuracy of the fabricated composite part is required because of the similar thermal expansion coefficients of the mold and composite materials. Whereas, metal molds are known to hold less dimensional accuracy under high curing process temperatures. However, composite based molds have short lifetime. Therefore, metal based molds are still preferred in mass production given the long service life and cost effectivity [3, 43].

Resin to metal adhesion is primarily due to chemical properties. While curing, the resin phase forms adhesion bonds with the solid metal substrate. Characteristically, epoxy resins contain hydroxyl groups and ether groups in the polymer chains of both the prepolymer and the cured resin [44]. Upon exposure to air, metals form metal oxides on their surface. Polar groups of the resin molecules develop strong hydrogen bonds with the metal oxides with bond energies in the 21 – 42 kJ/mol range. Even polymers with only nonpolar groups tend to build van der Waals forces with bond energies ranging from 2 – 21 kJ/mol. This causes adhesion bonding between a metal substrate and resin.

Additionally, mechanical interlocking plays a role in increasing the adhesion if the metal substrate is not smooth. The rough surface allows resin penetration/interlocking into the irregular pores on the surface, thus increasing the energy required for detachment [45]. It is further confirmed in literature that, irregular/porous mold surfaces cause higher cured resin-to-metal adhesion than a smooth surface. Similarly, curing under high pressure has also been reported to result in higher adhesion compared to normal pressure conditions. It is argued that the external pressure allows the resin to overcome surface tension and penetrate into the cavities on the mold surface, and thus mechanical interlocking causes higher adhesion. Therefore, the effect of curing pressure on adhesion seems to be dependent on the metal mold's surface roughness [4].

2.4 Adhesive/ Cohesive failure at a solid-solid interface

The work of adhesion is defined as the work done to separate two surfaces or media from contact to infinity. Adhesion is the parameter which quantifies the resistance to separation of two substrate surfaces. Detachment of one solid surface from another solid surface occurs by adhesive failure or/and cohesive failure. In either case, first, a crack initiates and then it propagates. During adhesive failure, crack initiation happens at the solid-solid interface and propagates along the interface (Figure 12a). For cohesive failure, crack initiation happens at the interface or inside the bulk material and it propagates through the bulk (Figure 12b). Hybrid

adhesive-cohesive failures occur when the crack propagates through the interface at some parts and through the bulk in others (Figure 12c). The path of least resistance is critical for crack propagation [46].

A cured resin adhered to a metal surface can be broadly compared to an adhesive layer in a metal-metal or metal-composite joint. There are numerous studies which discuss bonding failure of such joints. According to published literature, an adhesive failure occurs when there is contamination on the substrate surface, partial curing, inhibition to develop chemical bonds with the substrate (such as is the case with release coatings), or simply the applied stress exceeding the bonding strength at the interface. Meanwhile cohesive failures initiate due to excessive shear stresses or pores/voids within the resin matrix [47]. Additionally, strain buildup in resin layers during the curing process is also reported in literature [48, 49]. This is beneficial as such locally stressed points have the potential to promote crack initiation or crack propagation [45].

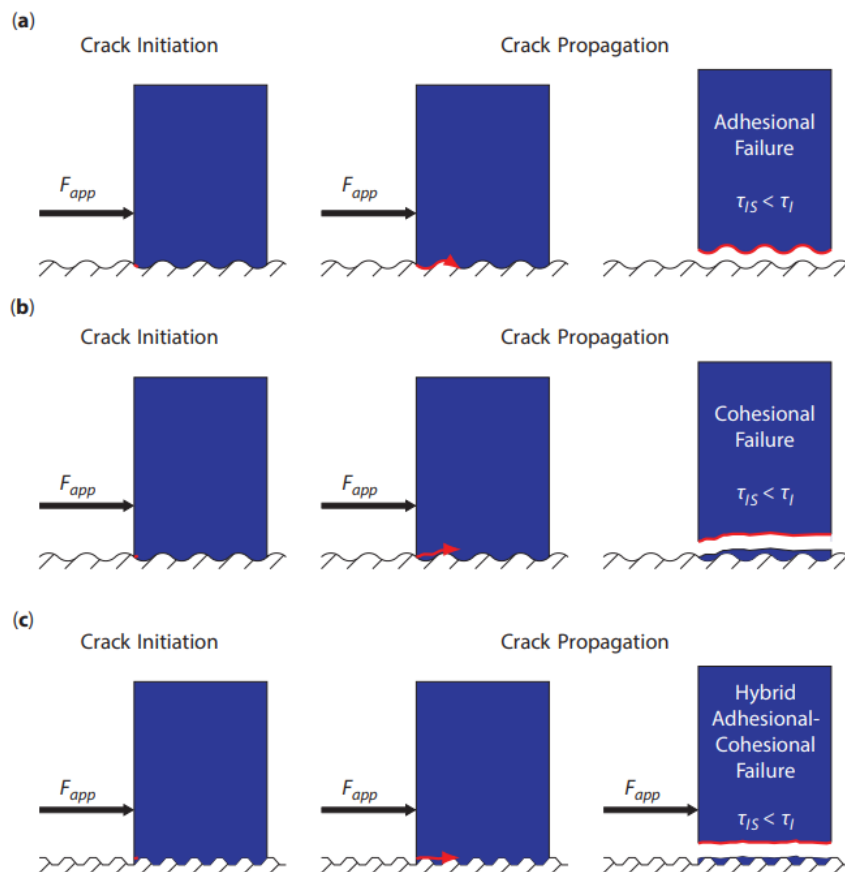


Figure 12 Crack propagation a) purely adhesive b) purely cohesive c) hybrid adhesive-cohesive failure. Reprinted with permission from reference [46] with © 2020, Scrivener Publishing LLC.

2.5 Laser modified metal tool surfaces for resin wetting and de-wetting properties

Liang et al. (2019) conducted a study on liquid resin anti-adhesion on metal tools used in composite manufacturing. They have reported the resin contact angle increasing to 149.7° from 59.6° on a steel surface by mold surface modification using laser machining and surface hydrophobization. A nanosecond pulsed laser system was used to fabricate microprotrusion structures (Figure 13a). Then, the surface chemistry was further modified by grafting low surface energy alkyl silane molecules onto the surface which characterizes the hydrophobization. Directly after the laser micromachining, substrates demonstrated complete wetting for the epoxy resin. After the hydrophobization, resin wettability decreased significantly, and contact angles above 130° were reported ((see Figure 13b).

Furthermore, the researchers claim that adhesion force along the sliding axis is proportional to the sliding angle (minimum tilt angle of the substrate for the liquid droplet to slide down) of the droplet. The sliding angles measured were as low as 7.3° . Even though the resin droplets did not show rolling off effect on the modified samples, the authors concluded that above surface modifications including the hydrophobization of steel promotes anti-adhesion of epoxy resin in the liquid state [50]. The conclusion is controversial as it is well established within the field that the liquid droplets should demonstrate both the low sliding angles and rolling effect for the substrate to be considered liquid repellent.

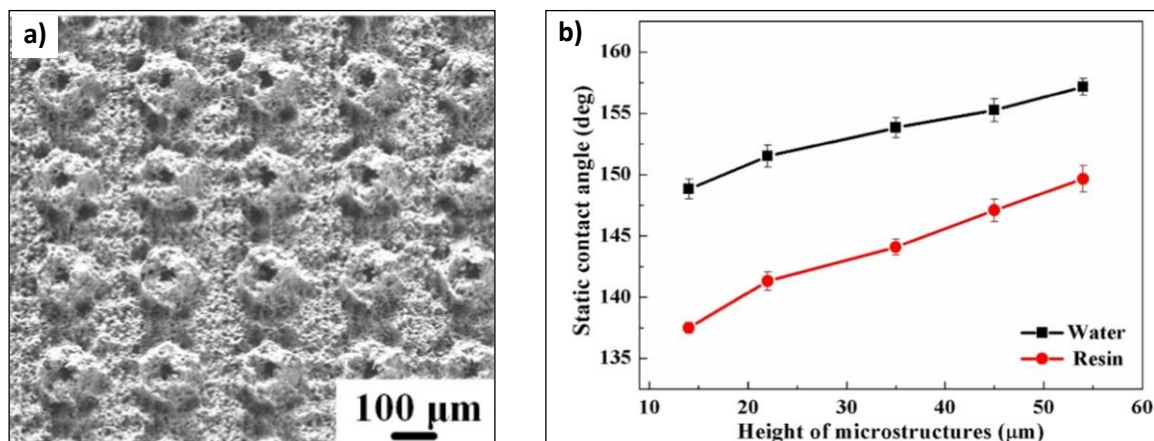


Figure 13 a) SEM image of a laser machined steel surface with microprotrusion structures. b) Contact angle change of hydrophobized laser machined samples with different microprotrusion heights (Microprotrusion diameter and spacing is 100 μm). Adapted with permission from reference [50] under © 2018, Elsevier B.V. All rights reserved.

The study does not have a strong scientific explanation for the claim that a lower sliding angle represents lower adhesion. Neither did they investigate the resin interaction with the modified metal surface while curing or after being cured, when changes in wettability could be expected

as explained previously. Also, the application of a hydrophobic layer is similar to the application of a release coating, which comes with the same concerns regarding contamination and reapplication. To the best of the author's knowledge, publications on anti-adhesion of resins on laser treated surfaces are scarce. Hence, there is a major knowledge gap on changing liquid/cured resin adhesion on metals using laser based surface modifications.

In contrast to the above-mentioned investigation, another study by Mund et al., 2019 focuses on increasing composite surface roughness by introducing a rough surface topography to the mold. The aim was to increase the adhesion in subsequent bonding processes between composite parts and to eliminate negative impacts of the release compound such as CFRP surface contamination and smoothness that prevents mechanical interlocking. By using a pulsed laser system with 1062 nm wavelength and 70 W power, they introduced an irregular rough surface to the aluminum mold as shown in Figure 14a. Different substrates were prepared by varying the scanning speed. They then applied a release agent coating on the mold and cured the composite thereafter. The resulting CFRP surface topography showed fracture patterns for some laser settings as indicated by the arrows in Figure 14b. Even the samples with other laser parameters which showed complete demolding in the first cycle have shown damaged surfaces in the second or third molding cycle. The only difference between the cycles is loss of release coating material at each demolding cycle. Therefore, the results from the study conclude that the demoldability (demoldable, demoldable with damage, not demoldable) of composite parts depends on the mold's surface roughness and surface energy [51].

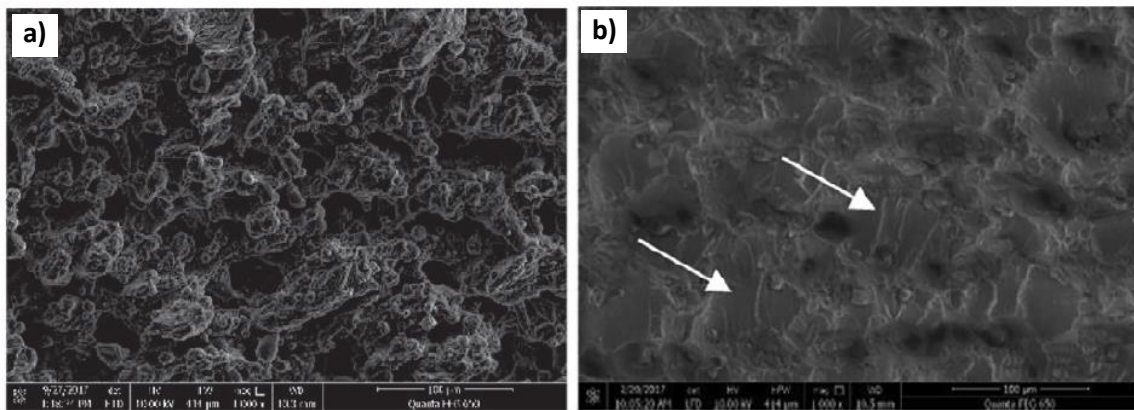


Figure 14 a) SEM image of the mould surface topography with scanning speed 500 mm/s and line pitch 0.05 mm b) Resulting CFRP surface topography. Adapted with permission from reference [51] under © 2019, Elsevier.

The observations from this study highlight that an irregular surface roughness introduced by the laser treatment has increased the composite bonding to the mold. Therefore, laser modification of surface topography can decrease as well as increase the resin adhesion to a

metal mold. The relationship between different surface topographies and resulting adhesion remains to be discovered.

2.6 Adhesion strength tests

There is no standard procedure specifically designed to measure demolding forces for composites from molds. Yet, there are two commonly used test methods for adhesion strength measurements of composite-composite or composite-metal bonded parts. A lap shear test (Figure 15) is the most used test method for that purpose. The recommended loading rate is 13 mm/min (0.5 in/min), specimen size is 25.4 x 101.6 mm (1" x 4") and overlapping area is 12.7 mm X 25.4 mm (0.5" X 1"). [52] Additionally, the ASTM 633C standard which is used for measuring adhesion and/or cohesion strength of thermal spray coatings is also a potential test configuration (Figure 16). With the ASTM 633C method, a tensile force is applied to a coating on one of the substrates which is also clamped as a fixture to the tensile tester. The other fixture is glued on to the coating surface using an adhesive with higher adhesion/cohesion strength. Cylindrical bars are usually used as the specimen for the fixtures [53].

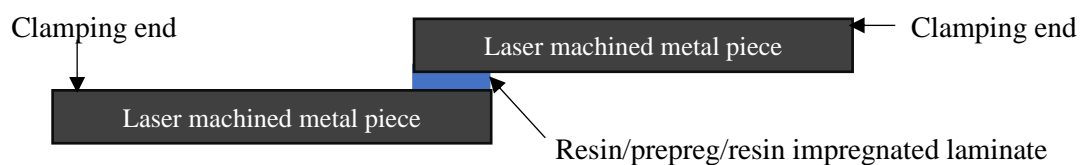


Figure 15 Illustration of a test sample for single lap shear test

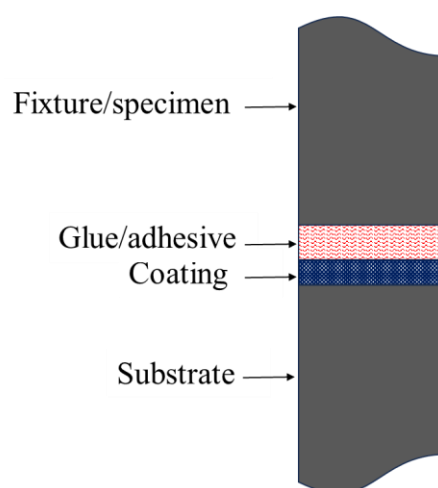


Figure 16 Schematic of an ASTM C633 test setup for a surface coating adhesion strength test

This chapter summarized findings and shortcomings in the existing literature to address resin adhesion and possible new strategies to outperform the current state of the art. Available literature confirms that adhesion failure occurs due to weak boundary layers and interface defects promoting crack initiation. Therefore, we conclude that mold substrate surface wettability and surface geometry affect adhesion strength at the resin-metal interface. However, no research is available on stable CB wetting states achieved for liquid resin-metal-air systems. Similarly, the effect of microcavities on adhesion failure needs better understanding. This highlights a research gap in the interest of resin anti-adhesion metal surfaces.

3 Objectives

This study focuses on exploring the efficiency of resin detachment from a metal surface based on the following hypotheses:

- a) Modifying the surface topology with microstructures that promote a CB wetting state allows a minimum contact area for solid-resin liquid interface. Under the assumption that liquid wetting contact angles are representative for the solidification process, such wetting should lead to a minimum contact area between the cured resin and mold, which ultimately leads to a decrease in adhesion strength at the resin-metal interface (Figure 17a). Furthermore, lower wettability or surface energy can be incorporated by changing the surface chemistry through post processing after laser irradiation.
- b) In the case of Wenzel wetting, air inside microcavities must escape the liquid resin matrix while curing takes place. Given the higher wetting inertia of resins, air bubbles can still be entrapped in the resin matrix after it is fully cured (Figure 17b). These voids or residual stress buildup at microstructure edges may promote adhesive failure at the interface.

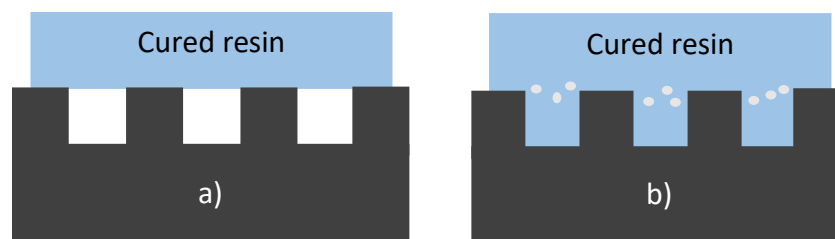


Figure 17 Schematic explaining the research hypotheses a) Cassie-Baxter wetting b) adhesion failure promoted by entrapped air bubbles in the cured resin matrix

The scope of this research was limited to studying resin-to-metal adhesion under elevated curing temperatures and atmospheric pressure conditions. Based on the hypotheses and the research gaps identified in the literature review, the main objectives of the study were as follows.

- i. Identify the critical contact angles that will define the adhesion strength of the cured resins to metal surfaces.
- ii. Identify trends between laser machined metal substrate surface properties and resin contact angle variations.
- iii. Identify the adhesion failure mechanism of cured resins on surface modified metal substrates.
- iv. Identify potential surface modifications for metal molds to increase the demolding efficiency of cured resins from the molds.

4 Materials and characterization techniques

4.1 Materials

The resin system and the metal material used for the study were industrial grade materials that are of interest to aerospace composite manufacturing. Accordingly, the metal chosen was an aluminum alloy (AA6061) sheet metal, which is recommended by the industrial partner. Only the resin adhesion on metal was focused on this study and therefore, no fiber matrix was incorporated in the resin phase. A summary of the resin specifications is listed in Table 1 below. Except in this section, the rest of the thesis will use ‘resin’ to refer to the resin system, which also includes the hardener material. No characterizations were performed to test the curing behavior of the R2 resin system, and the curing cycle is based on the technical data sheets.

Table 1 Material specifications for the resin system

Resin symbol	R2
Industrial names	Resin: EPIKOTE™ Resin L 20 Hardener: EPIKURE™ Curing Agent 960
Composition	Resin: <ul style="list-style-type: none">• Epoxy resin (bisphenol-A-(epichlorhydrin))• Epoxy resin (bisphenol-F-(epichlorhydrin))• 1,6-Bis(2,3-epoxypropoxy)hexane Hardener: 2,2'-dimethyl-4,4'-methylenebis (cyclohexylamine)
Mixing ratio	100: 34 (resin: hardener)
Pot life	4 hours (at 25 °C for 500 g)
Curing step	4 hours at 60 °C followed by 3 hours at 130 °C

Frekote 770-NC aerosol was used as the release coating (RC) material for comparison with laser modified samples. Frekote 770-NC is a silicone (polydimethylsiloxane) based release agent dissolved in a hydrocarbon solution.

4.2 Instrumentation and data analysis software

4.2.1 Laser system

Aluminum alloy samples were used as received after cleaning by sonication in acetone for 10 minutes. Laser micromachining was performed on metal samples using a class IV femtosecond laser system. The central wavelength of the Gaussian beam used is 1030 nm with a maximum repetition rate of 200 kHz and 40 W maximum power. Pulse duration was set at 224 fs. Metal samples were mounted on a translation stage. The laser beam path is stationary in this system, and the translation stages (Newport corporation, USA) are moving. Stages are actuated by a controller unit that decodes trajectory files pre-coded using Python software. Trajectory files included position, velocity, and time (PVT codes) data required to micromachine the desired surface geometry.

The laser micromachined structures are hexagonal holes, circular holes, and LIPSS. Raster scanning was used to ablate hexagonal holes and LIPSS. Raster scanning optimization was performed using a 5 mm incoming laser beam diameter and 10 cm lens focal length. The hole percussion drilling technique was used for micromachining circular holes. Circular hole drilling optimizations and metal substrate preparation for adhesion strength tests were completed using a 6.81 mm incoming laser beam diameter and 15 cm lens focal length. Further details on the micromachining laser parameters and optimization are provided in section 7.1. Immediately after laser irradiation, all samples were cleaned by sonication in acetone for 10 minutes and stored in airtight containers.

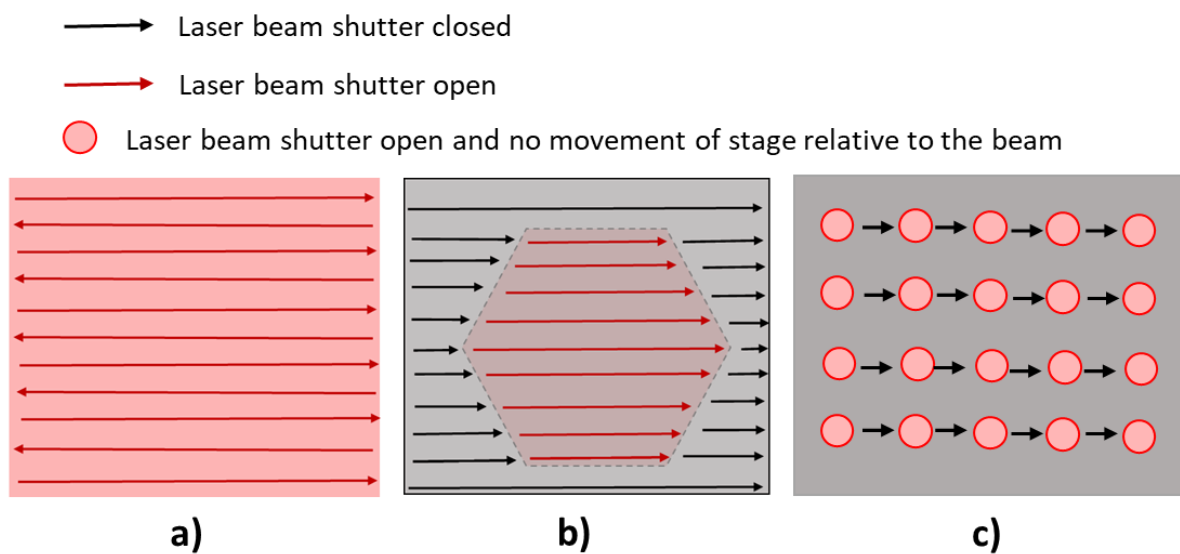


Figure 18 a) Raster scanning for LIPSS b) raster scanning for hexagonal holes c) percussion drilling for microscale holes

4.2.2 Tensile testing

A tensile testing machine (SHIMADZU AGS-H/EZTEST series) with a 500 N load cell was used for adhesion strength testing. Tensile forces were applied at 2 mm/min crosshead speed and the breaking loads were recorded. The sample preparation and sample holder setup are explained in detail in section 5.2. Adhesion strength was calculated by dividing the breaking load by the effective surface area of the failed interface. The effective surface area was extracted from images of the failed metal sample surface using ImageJ software.

4.2.3 Surface characterization

The laser micromachined sample surfaces and failed interfaces were characterized using Scanning Electron Microscopy (SEM) imaging and laser scanning confocal profilometry. The SEM (Model: FEI Quanta 450 FE-ESEM) was used to micrograph the surface topology. Images were taken under 10 kV high voltage mode and data was collected through a secondary electron detector. Occasionally, Energy Dispersive X-ray Analysis (EDX) function in the SEM was used to detect compositional distributions on surfaces for qualitative analysis. The laser scanning confocal profilometry (Model: Olympus LEXT OLS5000-SAF) was used to collect depth profile data and surface roughness. The surface roughness of bare metal samples was extracted using the areal roughness (S_a) calculator in the OLS5000 software for confocal data analyzing. The considered parameter is the arithmetical mean height which is calculated with Equation 17, where z is the depth/height at a (x, y) coordinate in the considered area.

$$S_a = \frac{1}{A} \iint_0^A |z(x, y)| dx dy \quad \text{Equation 17}$$

The wettability of the surfaces was characterized using a custom-built contact angle goniometer in the Biomimetic Surface Engineering Lab at the Chemical Engineering Department of McGill University. Resin droplets of microliter volume ($>2 \mu\text{l}$) were generated through a 1 ml disposable luer lock syringe with a 32-gauge needle tip connected to a 70-2203 syringe pump module (Harvard apparatus, USA). A new heating stage was combined with this setup for this study. The specifications of the heated stage are reported in section 6.2.2. Videos of sessile droplets were captured by a microscopic camera (Infinity 3 by Teledyne Inc, CA) with 20 frames per second. For sections 6.2.1 and 6.2.3, videos were analyzed using SCA20 contact angle measurement software to detect and record contact angles at each frame. For the rest of the analysis, a more user-friendly, custom MATLAB based video analysis software was used

[54]. The surface tension values were obtained using the OPENDROP software following the pendant drop method (refer section 6.2).

5 Adhesion strength test development and resin leaking

Designing a suitable adhesion strength measurement technique was one of the first steps of the methodology development. Given the nature of the application, the focus was to establish a test method that quantifies adhesion strength subjected to a tensile force. Therefore, the initial setup was inspired by the ASTM 633C standard mentioned in section 2.6 with modifications to accommodate a sheet metal substrate.

For the preliminary studies, the resin solution was drop-cast, aiming to create roughly a 1-2 cm² area of resin layer on the sheet metal surface. The sample was then cured according to the standard curing cycle for the resin from Table 1. As presented in Figure 19, the T-shaped sample holders (upper traverse and bottom traverse) were clamped to the tensile tester. The laser machined sample was clamped to the bottom traverse. The upper traverse was glued to the cured resin layer using Loctite 496, an instant adhesive dissolving in acetone so that the upper traverse is reusable.

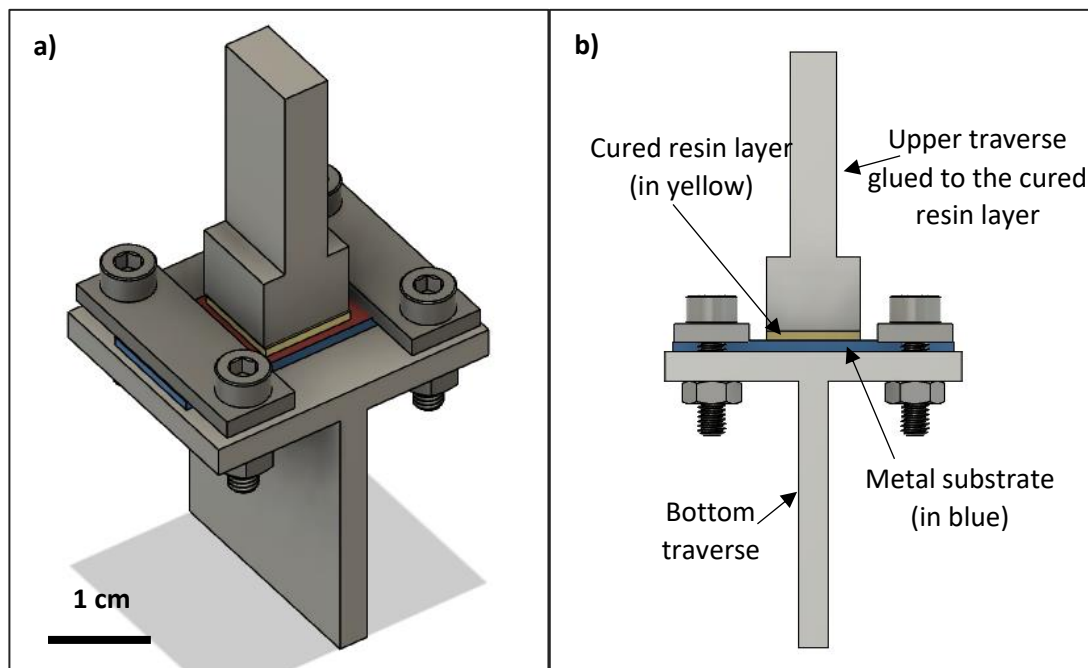


Figure 19 Initial tensile test set up a) 3D view b) 2D side view (the resin layer is not in actual scale with the other components)

5.1 Resin leaking

Figure 20a illustrates the laser micromachined area on a sheet metal sample. Only the middle portion of the substrate was laser machined and there is a clamping allowance at the two ends. The resin layer should ideally be present only within the laser micromachined area in the middle of the sample to ensure that the measured adhesion strength only corresponds to the laser micromachined surface area. However, due to the high affinity of resin to metal, the resin solution randomly spreads on the metal sample surface while curing (Figure 20b). Such samples could not be clamped to the setup without disturbing the cured resin layer, which eventually concerned the repeatability of results.

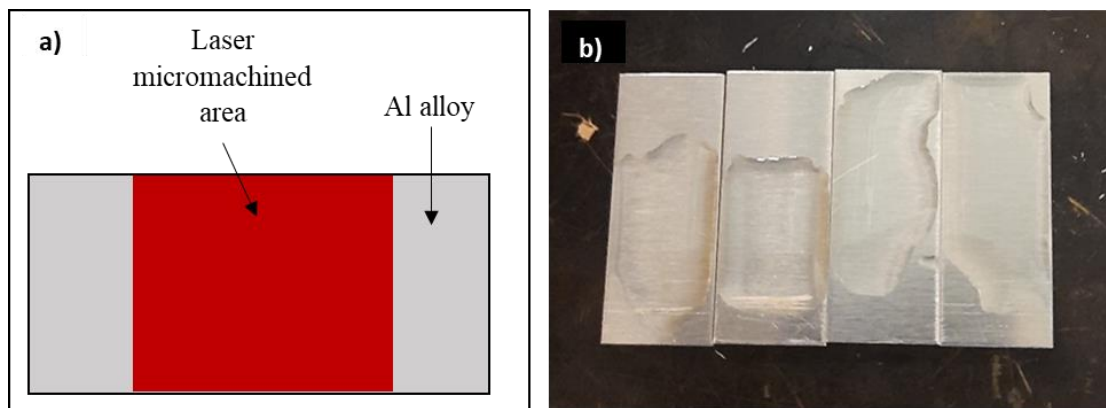


Figure 20 a) Illustration of a laser micromachined substrate sample b) Random spreading of same amount of resin on Al alloy samples with identical surface topology

Resin overflow/leaking is a common occurrence in composite fabrication. The best practice to avoid the issue has been to apply release coating on the boundaries, which however is not compatible with the testing purposes of this project. Another simple fix is applying a physical barrier such as thick tape, silicone glue etc. Hence, an adhesive tape was applied around the desired surface area to act as a barrier for resin flow beyond the laser patch (illustrated in Figure 21a). This approach worked for the bare metal control samples as shown in Figure 21b. However, for the laser micromachined surfaces, resin spreads more vigorously and beyond the adhesive tape on top or underneath (see Figure 21c). This uncontrolled resin leaking on laser patches was suspected to be caused by changes in surface wettability after the laser micromachining process.

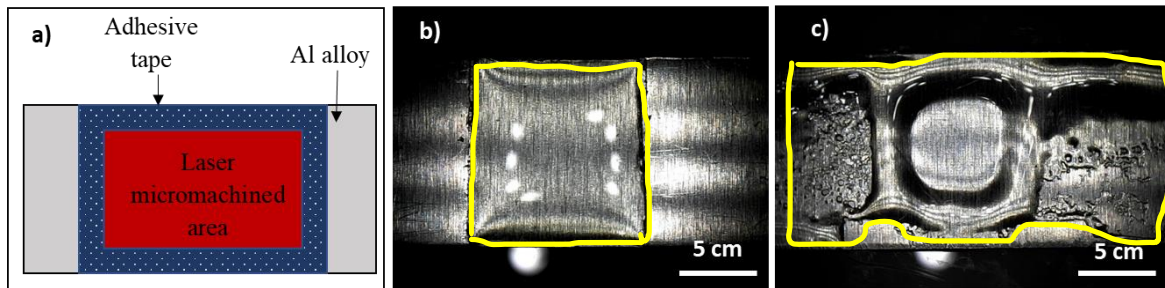
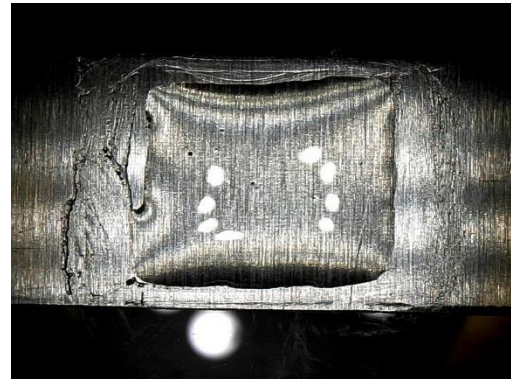


Figure 21 a) laser micromachined area surrounded by an adhesive tape to prevent liquid resin flow beyond the laser patch b) Resin patch cured with adhesive tape boundary on a bare metal surface c) Resin patch cured on a laser micromachined metal sample surface with adhesive tape boundaries. Yellow contour lines mark the resin areas.

Troubleshooting the resin leaking issue involved two different approaches: (1) a chemical barrier and (2) a physical barrier application around the laser micromachined area. The various different procedures tested are summarized in Table 2 and Table 3.

Table 2 Chemical layer barriers applied to prevent resin leaking

Procedure explained	Figures and illustrations
<p>Method 1</p> <p>From the literature review and preliminary contact angle tests (section 6.2) it was evident that release agent materials retain the resin flow. Therefore, a gel type Polydimethylsiloxane (PDMS) based release agent (DOW CORNING 7 release compound) was applied directly on the sample boundary.</p> <p>To check if there is PDMS material diffusion into the patch underneath the resin layer, another similar sample was subjected to the curing cycle without a resin layer on the surface. After this, an EDAX analysis was carried out to track if there were Silicone traces within the laser micromachined surface area.</p> <p>Observations:</p> <p>This approach succeeded in stopping the resin overflowing as presented in Figure 22. However, tensile tests resulted in extremely low adhesion strengths that highly deviated from other test samples. From the EDAX data for the blank sample, Si was detected to be present even in the middle of the patch.</p> <p>Conclusions:</p> <p>The presence of the release agent boundary controls the resin flow, but release agent material diffuses into the area of interest and alters the actual adhesion at the resin-metal interface. Therefore, this method is not suitable for the purpose of this study.</p>	 <p><i>Figure 22 Resin layer cured with PDMS-based release agent gel applied on the boundary of a bare Al alloy sample</i></p>

Method 2

The presence of non-polar groups on a surface lowers the surface energy and thus reduces surface wettability. Therefore, the laser micromachined sample surface was grafted with an alkyl chain monolayer by lauric acid treatment. The metal sample was dipped in 200 mM lauric acid/ ethanol solution for 30 minutes, and then washed by dipping once in ethanol. After, the sample was dried at 80 °C for 15 minutes in the oven. Finally, the sample was laser micromachined within a day.

Observations:

Resin was spreading beyond the laser patch area as presented in Figure 23.

Conclusion:

When the surface chemistry is homogeneous everywhere in the sample, resin spreads throughout the sample.



Figure 23 Resin layer cured on circular hole laser micromachined Al alloy sample after the entire surface is lauric acid treated

Method 3

After laser micromachining, the sample was sonicated in acetone for 10 minutes. Then the two sides which were not laser micromachined were dipped in 200 mM lauric acid/ ethanol solution for 30 minutes then washed with ethanol by dipping once. The sample was then dried at 80 °C for 15 minutes in the oven.

Observations:

The resin seemed not to spread beyond the laser patch into the lauric acid treated region as evident in Figure 24. However, treating the non-laser machined sides distinctively was challenging as the lauric acid-ethanol solution readily flowed into the laser micromachined region.




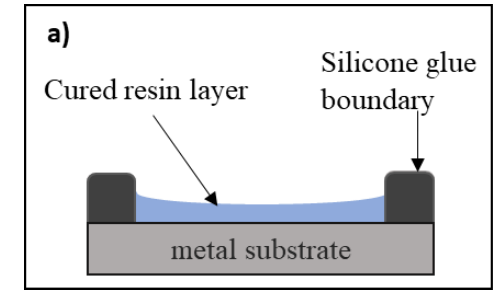
Figure 24 Resin layer cured on circular hole laser micromachined Al alloy sample

Conclusion:

When there is a chemical compositional difference, it acts as a barrier to the resin flow. However, there is a high possibility that a portion of the laser machined area is also subjected to surface compositional change.

*after the non-laser machined areas are
lauric acid treated*

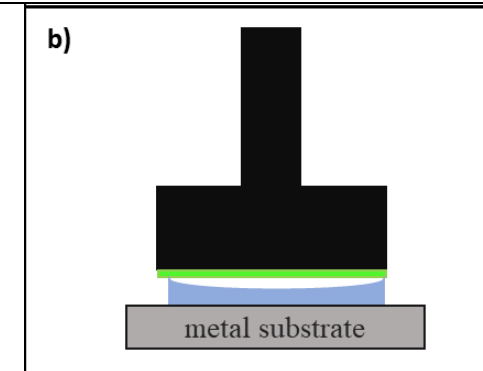
Table 3 Physical barriers applied to prevent resin leaking

Procedure explained	Figures and illustrations
<p>Method 4</p> <p>An adhesive tape was applied just around the boundary of the laser patch. The overlapping of the adhesive tape onto the laser patch was kept minimal through naked eye observations.</p> <p>Observations:</p> <p>The resin leaked in areas that were open to the adhesive surface of the tape (Figure 25).</p> <p>Conclusion:</p> <p>Whenever the resin solution encounters the adhesive surface of the tape, it reacts or wicks through the adhesive material, thus, intensifying the resin leaking.</p>	 <p>Figure 25 Resin leaking in an Al alloy sample with an adhesive tape carefully applied just around the boundary of the laser micromachined region</p>
<p>Method 5</p> <p>Using silicone glue as a boundary to prevent resin leaking is a common practice in composite sample preparation. An adhesive tape was applied just around the boundary of the laser patch. Then a silicone glue (DOWSIL™ 732 multipurpose sealant) boundary was applied on top of the tape boundary prior to depositing the resin mix. This way, the glue boundary was easily removable after the resin curing.</p> <p>Observations:</p> <p>The resin leaking was controlled but due to the high affinity of the resin with the glue material, the cured resin layer surface had a concave shape which was not suitable for the test setup as</p>	 <p>Figure 26 Resin layer cured with silicone glue boundaries a) side view</p>

illustrated in Figure 26a. This concave surface does not allow the upper traverse to grip and glue well with the resin surface as sketched in Figure 26b.

Conclusions:

Suitable method for preventing the resin leaking issue, however not ideal for the test setup.



b) side view with the upper traverse glued by the instant adhesive

Method 6

A 3D printed polymeric ring mold was clamped on to the sheet metal surface surrounding the laser micromachined area as illustrated in Figure 27. A release agent material (Frekote NC770) was sprayed on the ring mold before clamping such that resin adhesion on the ring mold is minimal and it is easier to remove after the resin layer is cured.

Observations:

The ring mold prevented resin leaking. However, for some laser patterns, the resin patch cured with the concave surface, as in method 5 above.

Conclusions:

Suitable method for preventing the resin leaking, however not ideal for the test set up.

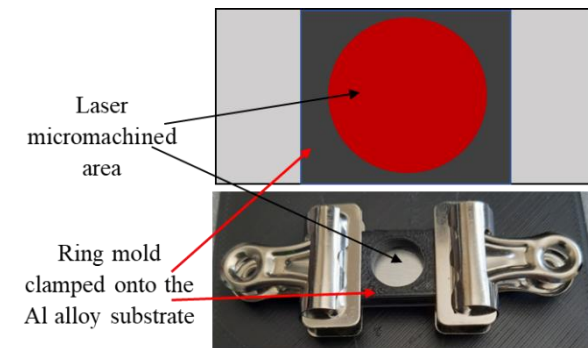


Figure 27 Illustration of a plastic ring mold clamped onto a laser-machined sample

With the knowledge accumulated from the observations in Table 2 & Table 3, it was concluded that neither of the barrier mechanisms are ideal for reliable experimentation to measure adhesion strength. Furthermore, the instant adhesive used for glueing the upper traverse to the cured resin layer, frequently caused deviations in the breaking stress readings. Due to the varying thickness of the adhesive layer, the degree of cure of the adhesive was not consistent among the samples. Additionally, the presence of voids in this adhesive layer was also suspected. Therefore, a novel setup was tested to avoid both resin leaking and the drawbacks of the instant adhesive layer.

5.2 Finalized tensile test setup and sample preparation procedure for tensile testing

A modified upper T holder (Figure 28a) that have the ability to clamp another counter substrate and be placed in touch with the bottom substrate was added to the setup. This allowed a resin layer to be cured while sandwiched between the overlapping area of two metal substrates. Both the top and bottom substrates had the same surface features (both bare metal or both textured with same microstructure pattern). Resin leaking did not occur in this overlapping configuration. The presence of similar surface tension from the two counter substrates in the overlapping region limits resin flowability because the free energy surface area of the resin phase is significantly reduced. Therefore, resin leaking is prevented.

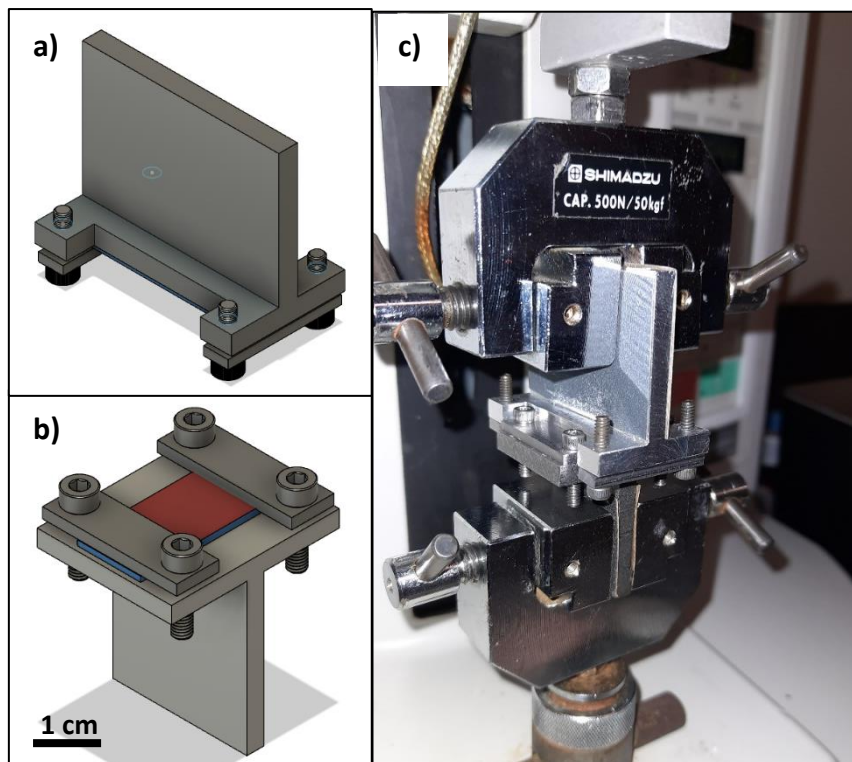


Figure 28 Finalized tensile test set up for adhesion strength test a) Top substrate with T holder unit b) Bottom substrate with T holder unit c) actual image of the setup clamped to the tensile tester

The region where the two traverses overlap is 12 mm x 14 mm in surface area. With this setup, the detailed sample preparation steps were as follows:

- i. Mix the epoxy resin and hardener in the correct ratio until a clear solution is obtained.
- ii. Keep the resin solution under vacuum in a vacuum oven till air bubbles in the solution disappear (approximately 15 minutes under ~60 mmHg pressure).
- iii. Take the resin solution out of the vacuum oven and load it into a disposable syringe (a syringe provides more control over resin deposition).
- iv. Drop cast 0.02 g of resin solution in the middle of the laser micromachined patch on the bottom substrate.
- v. Place the top substrate on the resin droplet perpendicularly to the bottom substrate. (See Figure 29)
- vi. Cure the resin following the recommended standard curing cycle.
- vii. Mount the bottom substrate on the bottom T holder.
- viii. Carefully turn the sample unit upside down and mount the top substrate on the upper T holder.

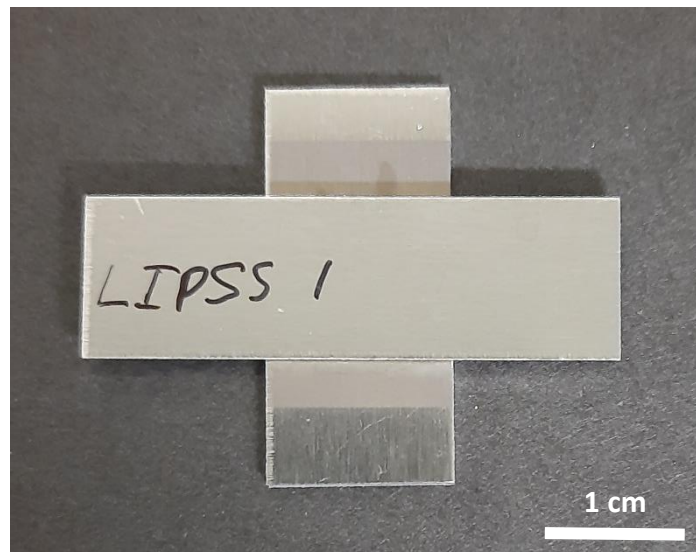


Figure 29 A tensile test sample before mounting on the test set up (A resin layer is cured in between the overlapping area of the orthogonally placed substrates with the same surface modifications

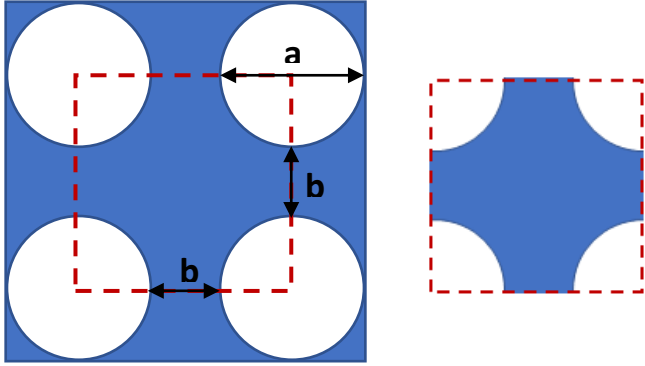
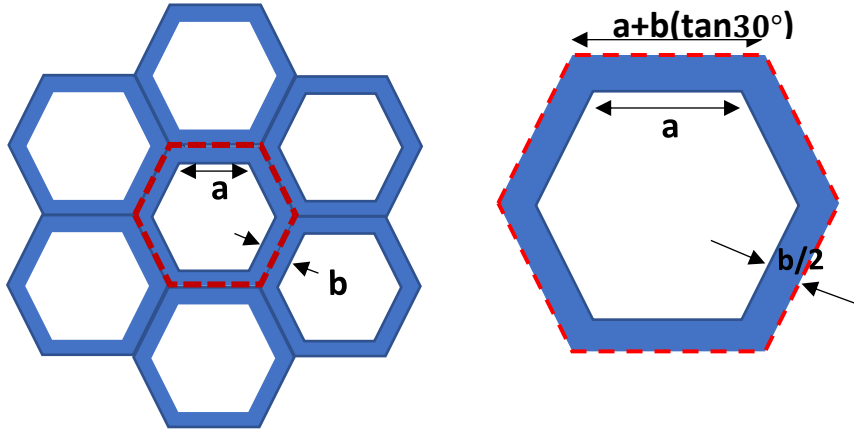
6 Optimization of required surface geometries

6.1 Thermodynamic calculations

The literature review highlights that achieving a CB wetting state for low surface tension liquids, including resins, is challenging. Therefore, while considering the laser micromachining feasibility, microstructures with the best possible non-wetting robustness were qualitatively selected for further theoretical analysis. When comparing pillars and holes structures, hole structures have closed cavities which support the entrapment of air or gases in contrast to open-cell pillar structures [55]. Since closed-end hole structures better sustain stable air pockets and thus, higher breakthrough pressure thresholds, cylindrical and hexagonal holes were considered for this study. Two different hole geometries were chosen to investigate the effect of feature geometry. The shape of the three-phase contact line differs with the hole geometry and thus can cause variations to the overall surface tension force.

After the above preliminary judgments, the most desired structural dimensions for stable CB wetting states were optimized through further thermodynamic calculations. The arrangements of the structures and the relevant calculations are summarized in the following sections. The equations are derived from the fundamental equations in section 2.2 while considering a unit cell of the selected patterns. A few common variables for both the hole structures are listed in Table 4. Definitions of a and b with respect to each pattern are given in Figure 30 & Figure 31. In addition to that, c represents hole depth.

Table 4 Equations derived for a unit cell of hexagonal and cylindrical hole patterns considered for this study

	Cylindrical holes	Hexagonal holes
Unit cell	 <p>Figure 30 Unit cell (marked in red dash lines) considered for cylindrical hole structures</p>	 <p>Figure 31 Unit cell (marked in red dash lines) considered for hexagonal hole structures</p>
$A_{unit\ cell}$	$(a + b)^2$	$\frac{3\sqrt{3}(a + b \tan 30^\circ)^2}{2}$
f	$\frac{(a + b)^2 - \frac{\pi a^2}{4}}{(a + b)^2}$	$\frac{A_{unit\ cell} - \frac{3\sqrt{3}a^2}{2}}{A_{unit\ cell}}$
$\cos\theta_{CB}$	$(\frac{(a + b)^2 - \frac{\pi a^2}{4}}{(a + b)^2})(\cos\theta + 1) - 1$	$(\frac{A_{unit\ cell} - \frac{3\sqrt{3}a^2}{2}}{A_{unit\ cell}})(\cos\theta + 1) - 1$
r	$\frac{(a + b)^2 + \pi ac}{(a + b)^2}$	$\frac{A_{unit\ cell} + 6ac}{A_{unit\ cell}}$

$\cos\theta_w$	$(\frac{(a+b)^2 + \pi ac}{(a+b)^2})(\cos\theta)$	$(\frac{A_{unit\ cell} + 6ac}{A_{unit\ cell}})(\cos\theta)$
L	πa	$6a$
η	$\frac{\pi ac}{(a+b)^2 - \frac{\pi a^2}{4}}$	$\frac{6ac}{A_{unit\ cell} - \frac{3\sqrt{3}a^2}{2}}$
λ	$\frac{(a+b)^2 - \frac{\pi a^2}{4}}{\pi a}$	$\frac{A_{unit\ cell} - \frac{3\sqrt{3}a^2}{2}}{6a}$

a) Cylindrical holes

According to Equation 9 and unit cell derivations for cylindrical holes in Table 4, the Gibb's energy change for CB wetting state and Wenzel wetting state are formulated in Equation 18 & Equation 19 respectively.

$$\Delta G_{CB} = \gamma_{la} \left(\frac{2(a+b)^2}{1 + \cos\theta_{CB}} + \frac{\pi a^2}{4} - [(a+b)^2 - \frac{\pi a^2}{4}] \cos\theta \right) \quad \text{Equation 18}$$

$$\Delta G_W = \gamma_{la} \left(\frac{2(a+b)^2}{1 + \cos\theta_W} - [(a+b)^2 + \pi ac] \cos\theta \right) \quad \text{Equation 19}$$

The breakthrough pressure equation is derived from Equation 16 and the data available in Table 4 corresponding to cylindrical holes.

$$\Delta P = - \frac{\gamma_{la} \left(\frac{(a+b)^2 - \frac{\pi a^2}{4}}{(a+b)^2} \right) \cos\theta}{\left(1 - \frac{(a+b)^2 - \frac{\pi a^2}{4}}{(a+b)^2} \right) \left(\frac{(a+b)^2 - \frac{\pi a^2}{4}}{\pi a} \right)}$$

$$\Delta P = - \frac{4\gamma_{la} \cos\theta}{a} \quad \text{Equation 20}$$

b) Hexagonal holes

Similarly to above, according to Equation 9 and unit cell derivations for hexagonal holes in Table 4, the Gibb's energy change for CB wetting state and Wenzel wetting state are listed in Equation 21 & Equation 22.

$$\Delta G_{CB} = \gamma_{la} \left(\frac{2(a\sqrt{3} + b)(3a + b)}{1 + \cos\theta_{CB}} + \frac{3\sqrt{3}a^2}{2} - [b^2 + ab(\sqrt{3} + 3)] \cos\theta \right) \quad \text{Equation 21}$$

$$\Delta G_W = \gamma_{la} \left(\frac{2(a\sqrt{3} + b)(3a + b)}{1 + \cos\theta_W} - [(a\sqrt{3} + b)(3a + b) + 6ac] \cos\theta \right) \quad \text{Equation 22}$$

The breakthrough pressure equation is derived from Equation 16 and data listed in Table 4 corresponding to hexagonal holes column.

$$\Delta P = \frac{\gamma_{la} \left(\frac{A_{unit\ cell} - \frac{3\sqrt{3}a^2}{2}}{A_{unit\ cell}} \right) \cos\theta}{\left(1 - \frac{A_{unit\ cell} - \frac{3\sqrt{3}a^2}{2}}{A_{unit\ cell}} \right) \left(\frac{A_{unit\ cell} - \frac{3\sqrt{3}a^2}{2}}{6a} \right)}$$

$$\Delta P = \frac{4\gamma_{la}\cos\theta}{\sqrt{3}a} \quad \text{Equation 23}$$

Resulting Equation 20 & Equation 23 show that low surface tension decreases critical breakthrough pressure whereas smaller hole diameter increases the critical pressure threshold. All the equations derived above require, θ and γ_{la} as input parameters. Therefore, to estimate the desired dimensions of a, b and c , θ and γ_{la} values should be known for the relevant three phase system which includes air, resin, and metal. The experimental methodology followed to obtain θ and γ_{la} values is discussed in the following section.

6.2 Liquid resin surface tension and wettability characterization



Figure 32 Example of a resin droplet image used for the surface tension calculation just before falling off from the needle tip

The surface tension of the resin solution was measured using the pendant drop method [56]. The pendant drop method considers a droplet just about to fall off from the needle tip. It uses the force balance between the vertical portion of surface tension and the weight of the droplet to calculate the surface tension. The experimentally calculated surface tension for the R2 resin solution was determined to be 7.5 mN/m at 60 °C.

However, obtaining an experimental θ value was a challenging task. Section 2.3 clarified the physical and chemical property changes of the resin solution during the curing process. Simultaneously, there is a possible adhesion bond formation between resin molecules and the metal surface oxides. Both aspects are connected to the wettability of the liquid resin on the metal. Therefore, a significant contact angle shift during the initial curing step was predicted upon temperature increase from room temperature to curing temperature due to changes in resin viscosity with temperature. On the other hand, the molecular structural change taking place during the heating was suspected to have a counter effect. These factors raised concerns over the apparent contact angle values that should be considered for this study. Since θ is required for further wettability predictions on rough surfaces, a contact angle measurement was performed for the R2 resin system on as received polished aluminum alloy with respect to the curing temperature.

6.2.1 Preliminary results of contact angle measurement

The initial contact angle experiments aimed to reveal the behavior of the apparent contact angle of liquid resin on metal at operating temperatures. Preliminary contact angle measurements were carried out on the Al alloy (AA6061) with the R2 resin system. Metal substrates were placed on a hot plate stabilized at a temperature of 30 °C. Just after the sessile resin droplet deposition, the temperature of the hotplate was increased from 30 °C to 60 °C. Then static contact angle images were captured using the camera setup. The data table is attached in APPENDIX I. Even after several repeat trials, this data set showed wide variability among the contact angle values recorded for the starting (just after droplet deposition at 30 °C) and finishing contact angles (at 60 °C). Three factors were hypothesized for this variation of results.

- i. Inertial wetting time impacted by droplet deposition kinetics

- ii. Inconsistent heating rates of the hotplate
- iii. Aging of the resin solution

According to the literature section 2.3, longer inertial wetting times are expected for highly viscous fluids. Additionally, the kinetic energy associated with droplet deposition may affect droplet inertia, thus causing variations in settling time. Therefore, another contact angle measurement was performed to verify this aspect with respect to the R2 resin system. After depositing the sessile droplet on the substrate, some time was allowed for the stabilization of the droplet before increasing the temperature to 60 °C. This delay in the temperature increasing step allowed to distinguish between the effect of temperature and inertia on the droplet spreading. The sessile drop behavior was recorded from the beginning (just after deposition), until any motion of contact angle was no longer visible to the naked eye. Droplet behavior was recorded at distinct intervals for ~3900 seconds.

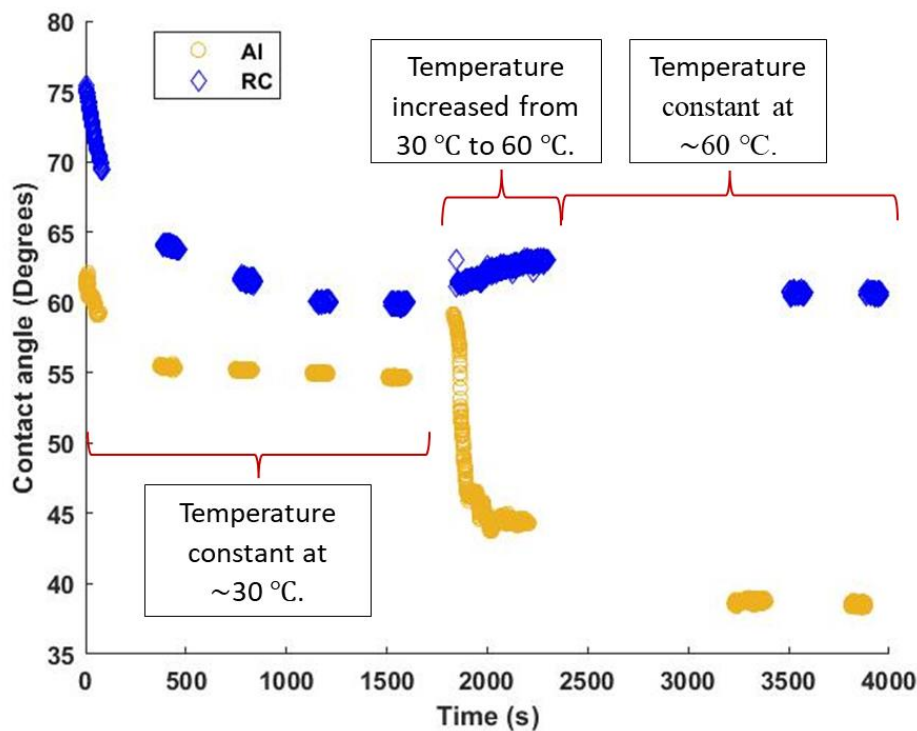


Figure 33 Time Vs Contact angle change for R2 resin system on bare Al alloy surface (Al) and release coating applied Al surface (RC)

Figure 33 shows the contact angle change for one exemplar experiment for a sessile resin droplet on a bare aluminum alloy surface and a release coating applied aluminum alloy surface respectively. As predicted, both surfaces showed longer inertial wetting times after droplet deposition. The bare aluminum alloy sample took ~500 seconds to reach the equilibrium contact angle, whereas the sample with release coating took ~1000 seconds. Interestingly, the contact angle decreased during heating to 60 °C in the bare aluminum alloy sample, but there

was no significant contact angle difference for the release coating applied substrate with release coating. This observation hinted at the increased resin wettability of the bare metal surface at elevated temperatures. However, the time spent after the resin solution was initially prepared (freshness of the resin mix) was not the same for the above two experiments, given that they were performed one after another. Slow curing reactions occurring after the resin mix is prepared cannot be neglected as this factor holds importance when comparing contact angle results and adhesion strength results between different substrates. Further to that, the heating rate of the substrate needed to be consistent to generate repeatable results. Therefore, a new experimental setup was prepared which is described in the following section.

6.2.2 Finalized contact angle measurement procedure

To solve the shortcomings highlighted in the previous contact angle experiments, a sample stage was built with more control over the heating rate. A silicone rubber flexible heating pad (Omega Engineering, Canada) was mounted under a metal stage, and controlled by a PID controller (Omega Engineering, Canada). The thermometer readings from the heating metal surface were used as input for the PID controller. This setup ensured each measurement received the same amount of thermal energy at the same rate throughout the experiments.

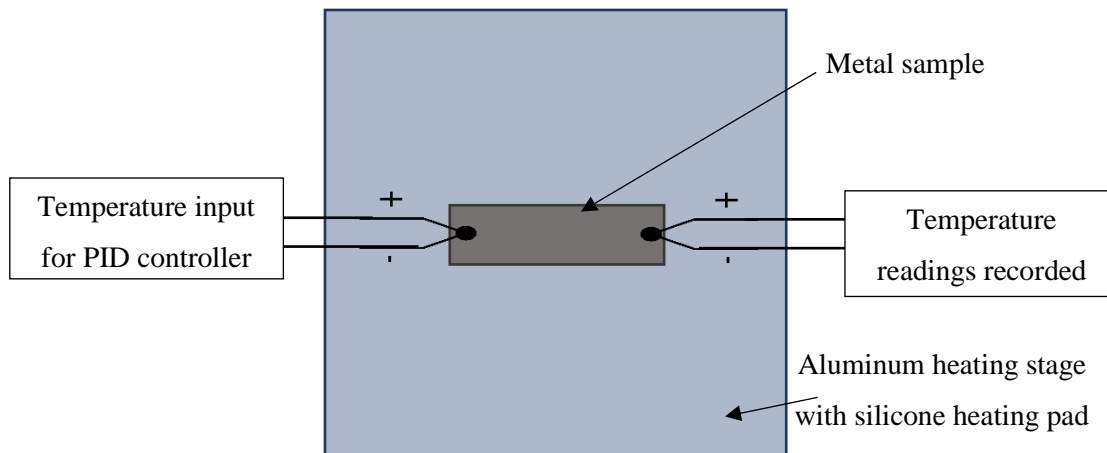


Figure 34 Schematic of the heating stage and the sample during a contact angle measurement experiment

The resin solution was prepared and kept at 25 °C. The metal sample was cleaned by sonication in acetone for 5 minutes and dried in air prior to the experiment. Then it was kept on the heating stage, and the temperature recording thermocouples were fixed at both ends of the rectangular metal sample, as presented in Figure 34 and Figure 35a. The sample temperature was stabilized at 30 °C, and then the sessile resin droplet ($> 2.5 \mu\text{l}$) was deposited using the goniometer set up through a 32-gauge needle tip. After keeping the temperature at 30 °C for 17 minutes (1020

s), the temperature was increased to 60 °C and kept for an additional 6 minutes. The heating curve used for the stage is charted in Figure 35b. This selected heating curve was based on the preliminary contact angle results discussed in the previous subsection. The 17 minutes stabilizing period was selected to match the stabilizing times observed in previous tests. The heating rate was dependent on the heating stage setup. The final 6 minutes at 60 °C was selected after detecting no further contact angle change. The contact angle data was recorded from the 16th minute (960 s) onwards.

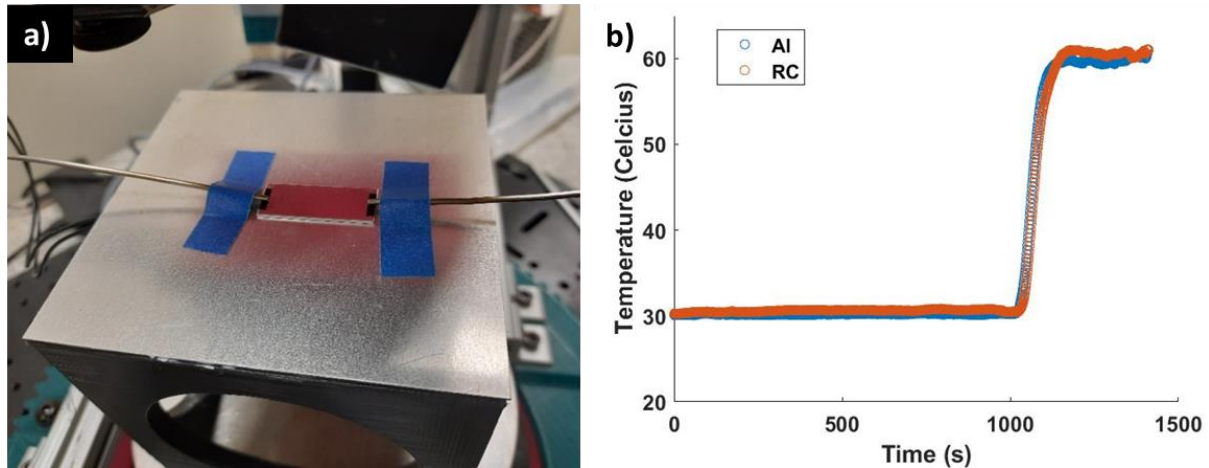


Figure 35 a) Image of the heating stage with metal sample and thermocouples attached to it during the contact angle measurement experiment b) Averaged heating curves used for the contact angle measurements on bare Al alloy surface (Al) and release coating applied surface (RC)

This sample stage setup ensured constant heating rates for all the repeated trials, allowing comparison between results as all the resin droplets had the opportunity to receive a similar amount of thermal energy.

6.2.3 Epoxy resin contact angle results on smooth metal substrates

The main objectives of contact angle measurements were to understand the liquid resin wetting characteristics upon heating to the curing temperature and identify the θ value that best represents the wettability for the concerned resin-metal-air system (R2-AA6061-air). Contact angle measurements were performed on three bare aluminum alloy substrates (Al) and three release coating applied substrates (RC). The experiments were completed at constant heating rates. Contact angle measurements were taken from droplets placed on the same substrate; 30, 120, and 240 minutes after the resin was prepared. These times were randomly selected within the R2 resin pot life which is 4 hours. The objective was to verify the wettability changes with respect to the resin solution age. For example, the Al_1 plot in Figure 36 represents contact angle readings of a droplet deposited after 30 minutes, then a droplet deposited after 120 minutes, and finally, a droplet deposited after 240 minutes on the first aluminum alloy substrate.

Figure 36 summarizes each experimental trial's final contact angles (stabilized contact angle at 60 °C curing temperature). Except for Al_2 and RC_3, none of the other samples showed significant deviations of contact angles among different resin ages (30, 120, 240 minutes). This result confirmed there is no significant effect of resin solution age on the final contact angle up to the resin pot life, for the R2 resin system.

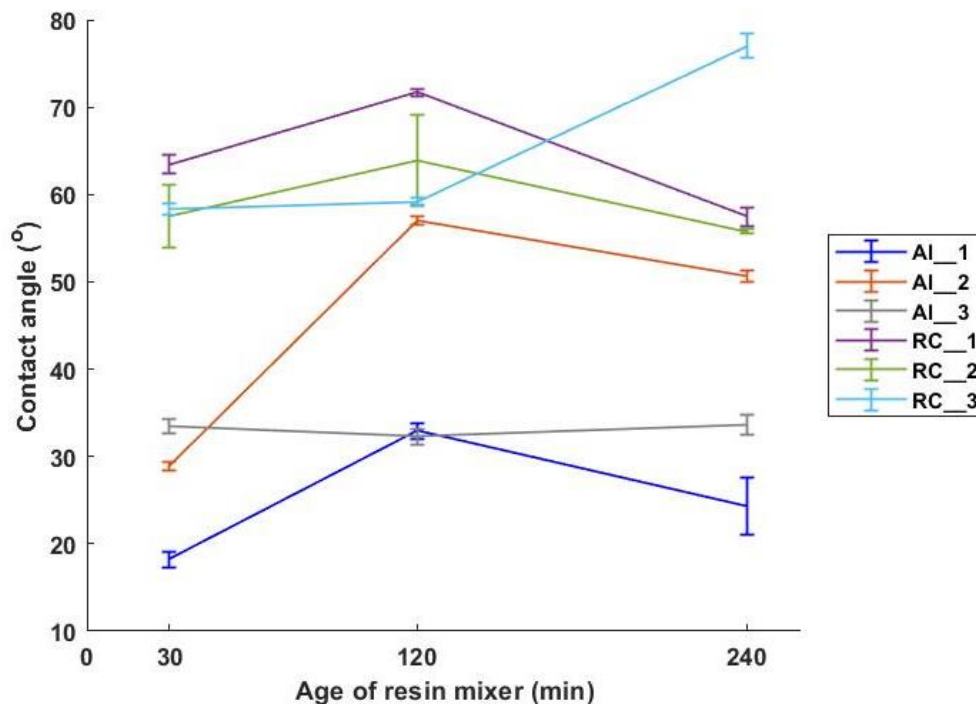


Figure 36 Final stabilized contact angles at 60 °C for bare aluminum alloy samples (Al) and with release coating applied aluminum alloy samples (RC)

According to the preliminary results from section 6.2.1, bare Al alloy samples were expected to show lower contact angles than the samples with release coating. Although that trend was generally followed, Al_3 sample showed higher contact angles at 120 minutes and 240 minutes. This deviation is attributed to different wetting natures observed on metal surfaces. An image of Al_3 is presented in Figure 38a. Usually, resin droplets placed on bare aluminum alloy samples showed directional wetting parallel to the polished lines. However, Al_3_120 and Al_3_240 have lesser directional wetting and spreading radius which caused higher contact angle readings than other samples.

Figure 37 summarizes the contact angles obtained before heating (at 30 °C) and after heating to the curing temperature (at 60 °C) for the same experimental campaign. The data confirmed no significant difference in contact angle upon heating to the curing temperature of 60 °C, which means heating does not significantly increase the resin solution wettability for this system. This is expected, given the resin system's increasing viscosity while curing reactions occur. For resin solutions, viscosity is a function of both time and temperature (Figure 10). Therefore, these results further clarify that resins have wetting characteristics unique from other polymer melts at elevated temperatures.

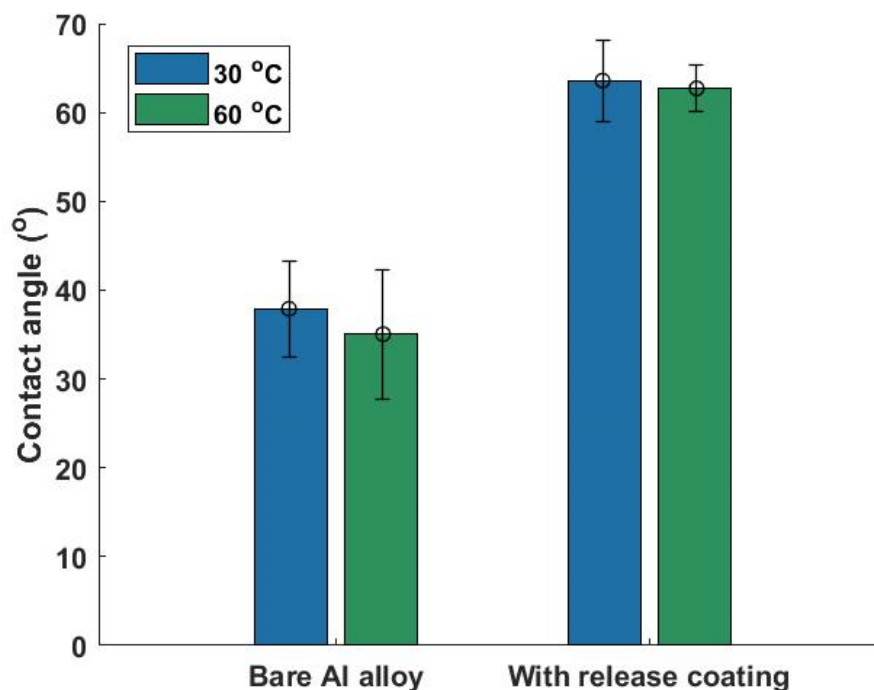


Figure 37 Temperature Vs R2 resin Average Contact Angle for aluminum alloy samples with and without release coating

Figure 38, top view observations for resin droplets at the end of experiments, show the nature of the wetting behavior that took place after droplet deposition. The bare Al alloy samples showed anisotropic wetting, whereas release coating applied samples had isotropic wetting behavior. The average surface roughness for bare Al alloy samples was $1.42 \pm 0.09 \mu\text{m}$, and $1.57 \pm 0.01 \mu\text{m}$ for release coating applied samples.

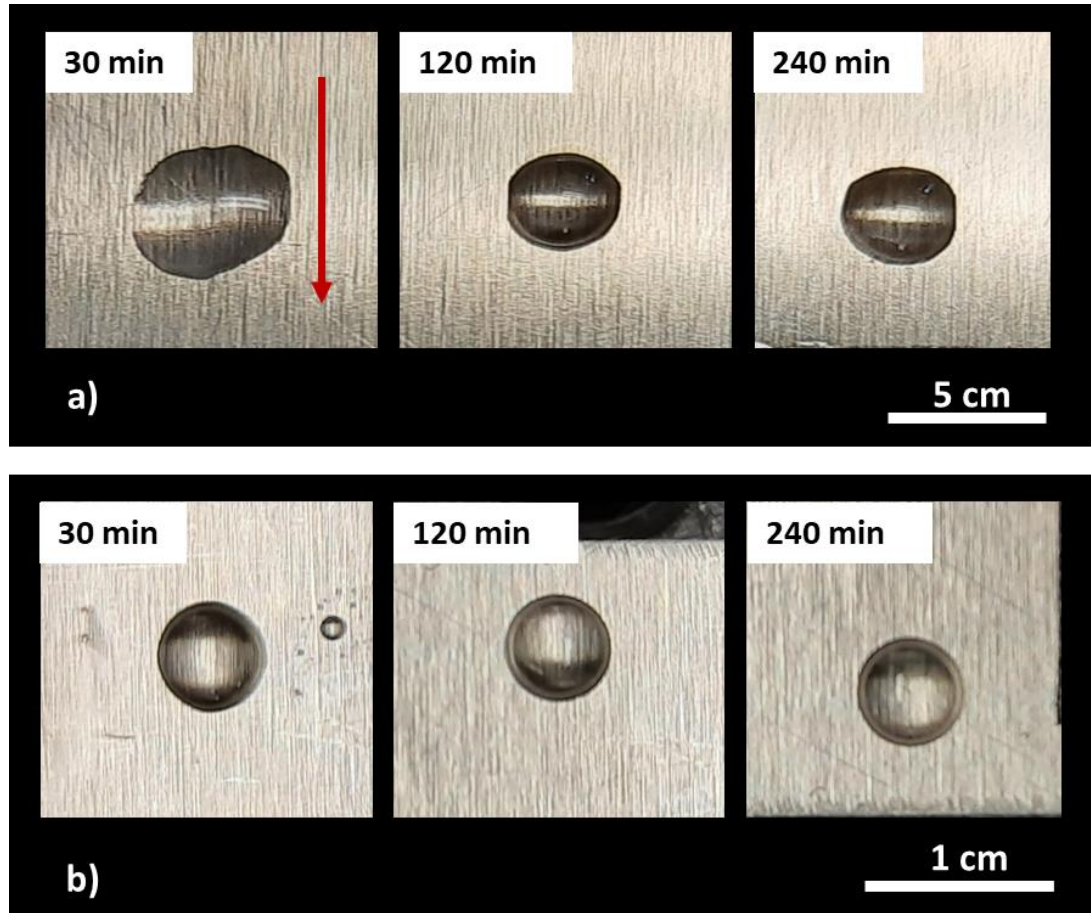


Figure 38 R2 resin droplet top view images at the end of the contact angle experiments for a) a bare aluminum alloy sample, red arrow: polished line direction b) a release coating applied aluminum alloy sample

The anisotropic wetting nature observed for bare aluminum alloy samples explains the large standard deviation in results. The release coating applied samples showed isotropic wetting at around the same surface roughness level. Therefore, high standard deviations in the bare aluminum alloy contact angles are attributed to compositional heterogeneity. However, even the release coating applied samples showed some variability. One experimental observation was that the sessile droplet deposition is affected by human errors. Consequently, initial kinetic energy of the droplet deposited varies from sample to sample, which directly affects the inertial wetting dynamics of the droplet. Thus, the base diameter or spreading nature of the droplet is affected. The more the droplet spreads, the higher the heat absorbed into the resin mix inside

the droplet, which means the rate at which the droplet becomes stable is affected. Since resin viscosity depends on temperature and changing molecular structure, the final stabilized contact angle depends on the local heating rate of the resin droplet. Thus, human errors at droplet deposition cause variations among different sample readings.

In summary, the bare aluminum alloy contact angle is 34.6 ± 12.1 , whereas release coating applied samples show contact angles of 61.4 ± 7.9 at the curing temperature for the R2 resin system. These values indicate that the compositional barrier introduced by the release coating layer decreases the resin wettability on the metal surface. However, the reason for significantly reduced adhesion strengths reported for release agent materials must be a combined effect of reduced wettability and barrier for adhesion bond formation with the metal surface. Further, it was concluded that the contact angle value (wettability) is not affected by the resin solution age within its recommended pot life. Therefore, future experiments were completed without attention to the resin lifetime, but within the resin pot life. Finally, 35° was used as the average contact angle (θ) for bare aluminum alloy for the calculations in section 6.3.

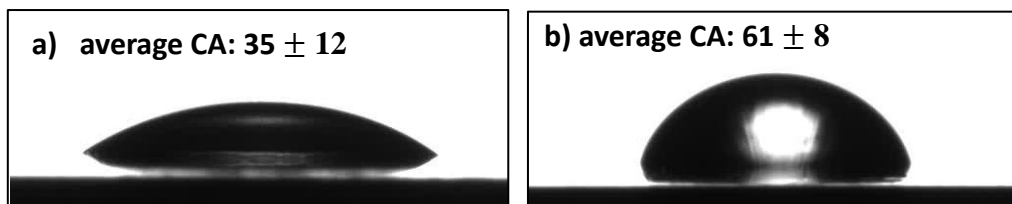


Figure 39 Side view of resin droplets on aluminum alloy surface a) bare aluminum alloy surface b) release coating applied aluminum alloy surface (CA - Contact Angle)

6.3 Selection of desired surface structures

This section summarizes the procedure followed to determine microstructural dimensions that would be the most favorable to cause air-trapping wetting behavior on metal. To this end, the contact angle determined in the last section ($\theta = 35^\circ$) was used as the apparent contact angle on a smooth aluminum alloy surface. The θ and γ_{la} values were plugged into the equations derived in section 6.1.

The feasibility of several dimensional combinations was considered under both the energy concept and the breakthrough pressure concept. Three aspects were considered in the optimization process.

- i. Achieving a stable CB wetting state
- ii. Achieving the highest possible CB \rightarrow Wenzel transition energy barrier
- iii. Achieving the highest possible critical breakthrough pressure difference

First, the contact angle at CB state (θ_{CB}) and Wenzel state (θ_w) were calculated for a selected a , b , and c combination. The dimensions that provide realistic contact angle values ($0 < \theta_{CB}, \theta_w < 180^\circ$) were used for further calculations. Two approaches were then taken, following the literature discussion in section 2.2.

a) Energy approach

First Gibb's free energy differences ($\Delta G = \Delta G_w - \Delta G_{CB}$) was determined. If the CB wetting state is in a global energy minimum, then ΔG should be positive. Therefore, if, $\Delta G > 0$ is satisfied then a, b, c corresponding to the maximum ΔG was selected as the most desired geometry. In the case that there are several possible combinations, the maximum contact angle at CB wetting state was considered as the next filtering condition.

If $\Delta G > 0$ cases were not available, then the metastable CB state was analyzed where a maximum Cassie \rightarrow Wenzel transition energy barrier (E_{gap}) exists. This route did not require further filtering as it resulted in a maximum E_{gap} with a unique combination of a , b , and c .

b) Pressure approach

Simultaneously, the second approach was to select the geometrical dimensions that would create maximum possible breakthrough pressure (ΔP). Equation 20 & Equation 23 confirms that, the breakthrough pressure is dependent only on a , which is the representative parameter of hole diameters. Hence, multiple combinations of b and c result in the same maximum

breakthrough pressure. Therefore, the second filtering condition was a maximum contact angle under a CB wetting state followed by the maximum E_{gap} .

A flow chart of the above process is illustrated in the Figure 40. A Python code was used to execute this entire optimization process (APPENDIX II). The results from the python code are attached in APPENDIX III. User defined input data points for the optimization codes are a , b , and c . A compatible range for each input parameter was chosen considering existing boundary conditions. Such as laser related constraints. Dimension a is closely related to the laser beam's effective diameter, because the cylindrical and hexagonal holes under consideration here are laser inscribed structures. Therefore, laser ablated area dimensions were restricted to be similar or higher than the laser beam's effective diameter. Dimension b was mostly restricted by the minimum spacing that is maintained without overlapping holes. Hole depth c was decided with respect to process time of the laser patches which is further explained in section 7.1.

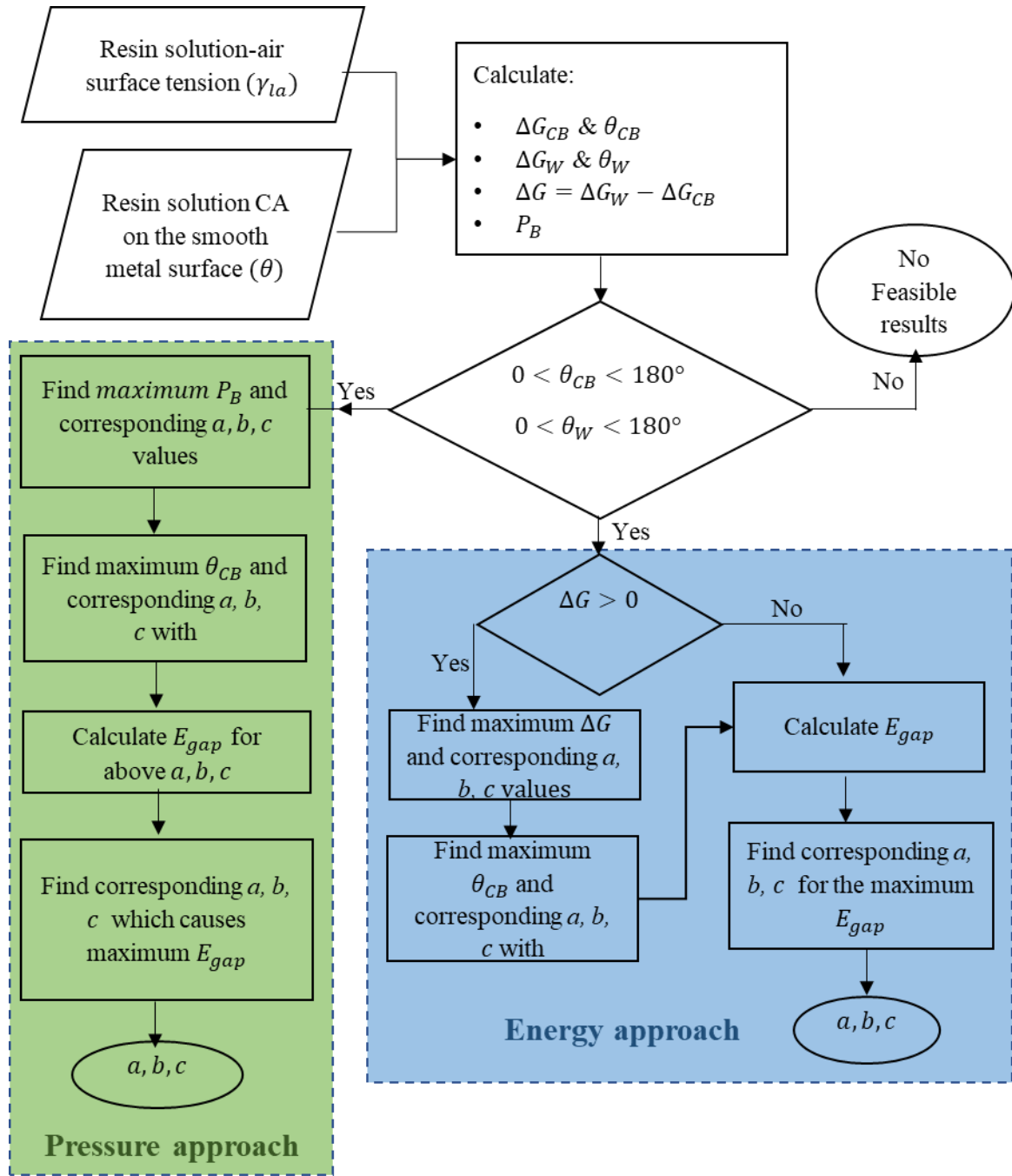


Figure 40 The summarized flowchart of the thermodynamic calculations followed in the python code

Table 5 lists the results from the screening process discussed above. None of the hexagonal hole combinations gave promising $\Delta G > 0$ values when the energy approach was considered. Therefore, a, b, c combinations with the highest transition energy barrier were selected. The negative ΔG results for most of the hexagonal and cylindrical holes further confirm that no stable CB wetting state is achievable. Although ΔG is positive for the cylindrical hole CY_P1 pattern, the energy gap is still very low. Given the low contact angle and surface tension measured for bare aluminum alloy surfaces, these theoretical results are not astounding. On the other hand, breakthrough pressure analysis identifies geometrical patterns that would retain the maximum possible pressure difference. According to the theoretically predicted ΔP values, cylindrical hole structures have significantly higher breakthrough pressure thresholds than hexagonal holes.

Table 5 Selected structural geometries from the optimization process

	Pattern	a (μm)	b (μm)	c (μm)	ΔG (nJ)	ΔP (Pa)	CA
Energy concept	CY_P1	25	149	5	0.009	984	38
Pressure concept	CY_P2	25	18	5	-0.011	984	70
Energy concept	HX_P1	127	36	16	-0.549	112	122
Pressure concept	HX_P2	80	81	18	-0.188	177	84

The textures listed in Table 6 were finalized for adhesion strength experimentation. Since HX_P1 pattern neither has a competitive breakthrough pressure nor is energy wise favorable for a CB wetting state, it was eliminated from the experimental campaign. Additionally, a cylindrical hole pattern with more hole depth was added to the experiments because more hole depth can increase the robustness of CB wetting state.

Table 6 Laser inscribed surface textures selected for the adhesion strength testing campaign

Pattern name	a (μm)	b (μm)	c (μm)	ΔP (Pa)	ΔG (nJ)	CA
CY_P1	25	149	5	984	0.009	38
CY_P2	25	18	5	984	-0.011	70
CY_P3	25	18	25	984	-0.008	70
HX_P2	80	81	18	177	-0.188	84

Both the literature and preliminary fs laser machining experiments revealed that laser irradiated surfaces tend to create hierarchical structures with nano scale features on top of microscale features. Therefore, it is essential to study the effect of finer structures than the microscale structures derived above. Hence, LIPSS structures on flat metal substrates were decided to be tested for resin-metal adhesion. Further, lauric acid treated LIPSS were also added in the experimental campaign to investigate effects from surface chemistry on resin-metal adhesion. Both ripples and triangular LIPSS were selected to uncover any effects from the different shapes of the laser induced textures.

7 Analysis of laser micromachined metal sample surfaces

7.1 Laser micromachining optimization

Prior to the preparation of the adhesion strength test samples, an optimization of laser settings for aluminum alloy micromachining was carried out. This step is crucial because, ablated material redeposition or material melting can occur under the wrong laser parameters which result in deviated hole geometries from the required geometries. Further, optimization ensures an efficient and precise surface modification process. First, the ablation threshold for the Al alloy was determined experimentally using Equation 1. The experimental value is 0.448 J/cm^2 . This indicates that the peak fluence of the laser beam used in the micromachining process should at least be 0.448 J/cm^2 or higher. The micromachining time and resulting structure quality were then optimized. The laser settings are reported in terms of peak fluence and PPS.

7.1.1 Cylindrical hole micromachining optimization

For the cylindrical hole structures, the hole entrance quality and the hole depth were optimized with respect to the machining time. As a first step, several laser beam powers (25 - 185 mW) and repetition rates (2 – 10 kHz) were tested. Among these results, the effective diameter of the laser beam at 27.1 mW, 2 kHz is $25 \text{ }\mu\text{m}$ which was an ideal dimension for the required cylindrical hole structures. In addition, the 27.1 mW, 2 kHz settings did not result in excessive nanoparticle redeposition or melting unlike the higher power settings. Therefore, only the drilling time was further optimized while keeping the power and repetition rate constant at 27.1 mW, 2 kHz. The corresponding peak fluence is 1.87 J/cm^2 . Drilling time is changed by either changing the scanning time or the number of overscans.

Table 7 shows the different settings tested and the laser process parameters finally selected are highlighted. Δz indicates the movement of the z stage towards the focusing lens so that the consequent overscan occurs at the focusing plane of the laser beam. In the occasions that several settings provide the same machining quality and hole depth, the settings with least micromachining time were selected.

The data from Table 7 show that the hole depth does not increase beyond $25 \text{ }\mu\text{m}$ after a certain drilling time. This is attributed to two reasons; 1) the laser beam is no longer focused on the deep ends of the holes and 2) the fluence falls below the threshold fluence. Simultaneously, the irradiated surface area at the narrow ends of the holes is higher than on a flat surface, which means that the accumulated fluence falls below the threshold fluence. Due to these reasons, the

material ablation is less efficient when producing deep and narrow hole structures using percussion drilling. Increasing the laser power progressively at each overscanning step is a potential solution, but this results in larger diameter and disoriented features at the hole entrance.

Table 7 Cylindrical hole percussion drilling optimization on Al alloy (AA6061) metal

Scanning time (s)	Total overscans	Δz (μm)	Depth of holes (μm)	PPS
0.016	1	-	3	32
0.016	10	5	18	320
0.016	20	5	21	640
0.016	50	5	22	1600
*0.025	1	-	5	50
0.025	5	5	22	250
0.025	10	5	24	500
0.025	20	5	20	1000
0.025	50	5	22	2500
0.05	1	-	10	100
**0.05	3	10	23	500
0.05	10	10	20	1000
0.1	1	-	23	200
0.1	5	24	22	1000
0.1	10	24	23	2000
0.5	1	-	24	1000
0.5	5	24	25	5000
*CY_P1 and CY_P2, **CY_P3				

Percussion drilling creates tapered holes on the surface due to the Gaussian intensity distribution of the laser beam. As a result, the micromachined holes have a conical shape that deviates from the desired cylindrical geometry (see Figure 41). This actual hole geometry has been taken into account when analysing the results in the following sections and the geometry will be referred to as “circular holes”.

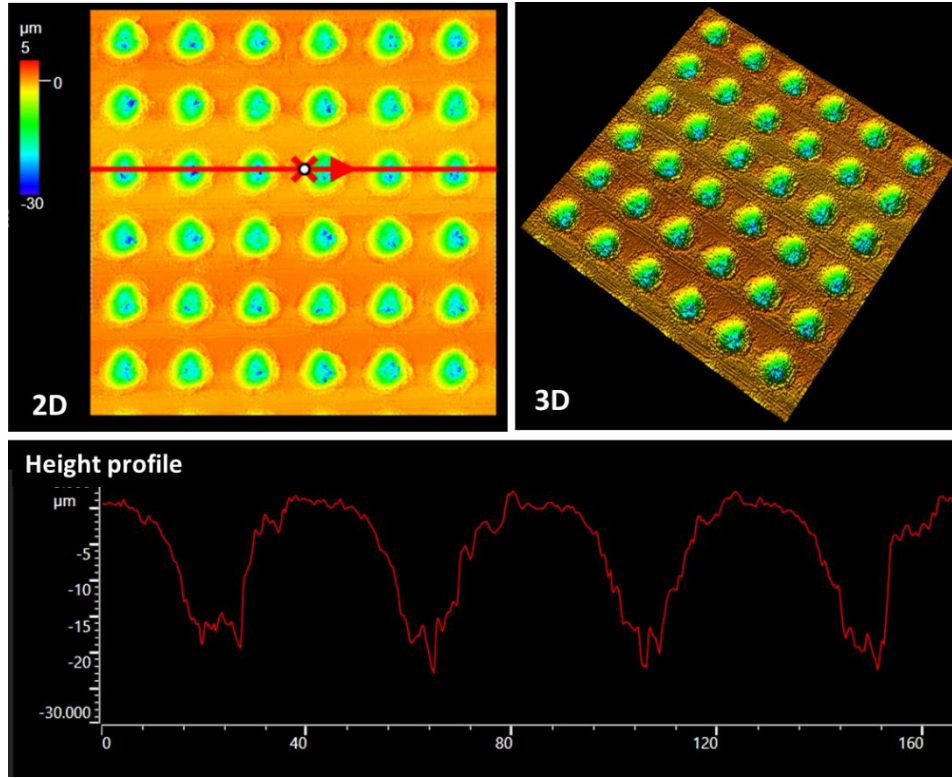


Figure 41 Confocal microscopy image of CY_P3 structures with the height profile of micro holes

7.1.2 Hexagonal hole micromachining optimization

The raster scanning strategy and total micromachining time for a laser patch affect the hexagonal hole fabrication. The quality of the material ablation was determined by observing confocal laser profilometry 3D maps. Exemplary images are presented in Figure 42. The represented raster scanned structures in Figure 42a shows efficient material removal from the surface, while Figure 42b-c show redeposition of the ablated material on the left side of the features. Depending on the required hole depth, the number of over scans was increased to achieve better refined hole structures (e.g. Figure 42d).

The considered laser parameters for the raster scans are listed in Table 8. The results indicated that 90% overlapping of the laser beam scanning trajectory is required for efficient material ablation. Then 34.8, 51.3 mW powers, 1 kHz repetition rate and 70 PPS gave satisfactory material ablation quality without major nanoparticle redeposition and melting. However, it is challenging to entirely prevent the nanoparticle redeposition. When the laser power increases, the micromachined depth also increases. After determining these initial settings, the laser power and PPS were fine tuned to adjust the hole depth required for HX_P2 pattern. Therefore, 61.3 mW, 1 kHz (12.74 J/cm²) and 75 PPS settings were used for HX_P2 pattern which gives the best compromise between machining time and structure quality.

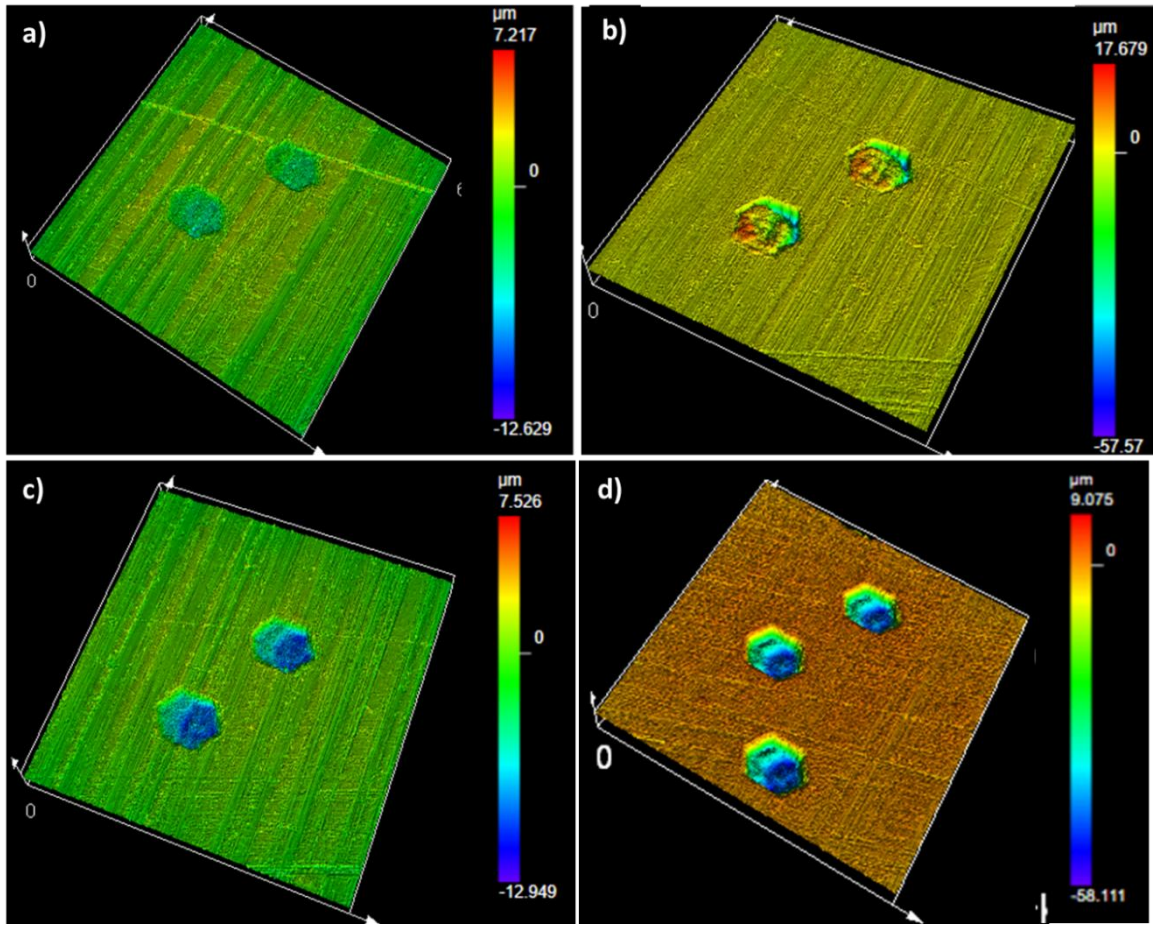


Figure 42 Raster scans with different laser parameters with 1 over scan a) 34.8 mW, 1 kHz, 70 PPS b) 184.6 mW, 1 kHz, 700 PPS c) 51.3 mW, 1 kHz, 70 PPS and d) 34.8 mW, 1 kHz, 70 PPS with 10 over scans

Table 8 fs laser raster scanning optimization on Al alloy (AA6061) metal

Power (mW)	Repetition rate (kHz)	Beam overlap (%)	Pulse fluence (J/cm ²)	PPS
26.5	1	50	12.75	9
26.5	1	50	13.94	4
34.8	1	50	10.54	12
34.8	1	50	13.11	5
51.3	1	50	19.32	10
51.3	1	50	22.68	5
34.8	1	10	9.85	8
51.3	1	10	14.51	8
34.8	1	90	9.85	70
51.3	1	90	14.51	70
105.5	1	90	29.85	70

7.1.3 Periodic nanostructures micromachining optimization

Finally, the LIPSS optimization was completed. The laser settings tested are listed in Table 9. Different low laser power settings were trialed with a beam polarizer to fabricate triangular LIPSS, whereas linear LIPSS were formed by the linearly polarized laser beam.

Table 9 Laser machining optimization settings tested for LIPSS

Expected structure	Power (mW)	Repetition rate (kHz)	Beam overlap (%)	Peak fluence (J/cm²)	PPS
Ripples	27.1	2	50	1.87	9
	27.1	2	90	1.87	43
	33.4	2	90	2.31	43
Triangles	27.1	2	90	1.87	43
	33.4	2	90	2.31	43
	38.6	2	90	2.67	43

The results (see Figure 43) indicate that the LIPSS generating window is narrow for this metal material. The selected laser settings for ripples are highlighted in Table 9 as 27.1 mW, 1 kHz (1.87 J/cm²), 90% overlap, 43 PPS. Triangular LIPSS formation was not homogeneous for AA6061 as displayed in Figure 43d-f. Therefore, only ripple structured LIPSS were used in the experimental campaign to study the resin-metal adhesion.

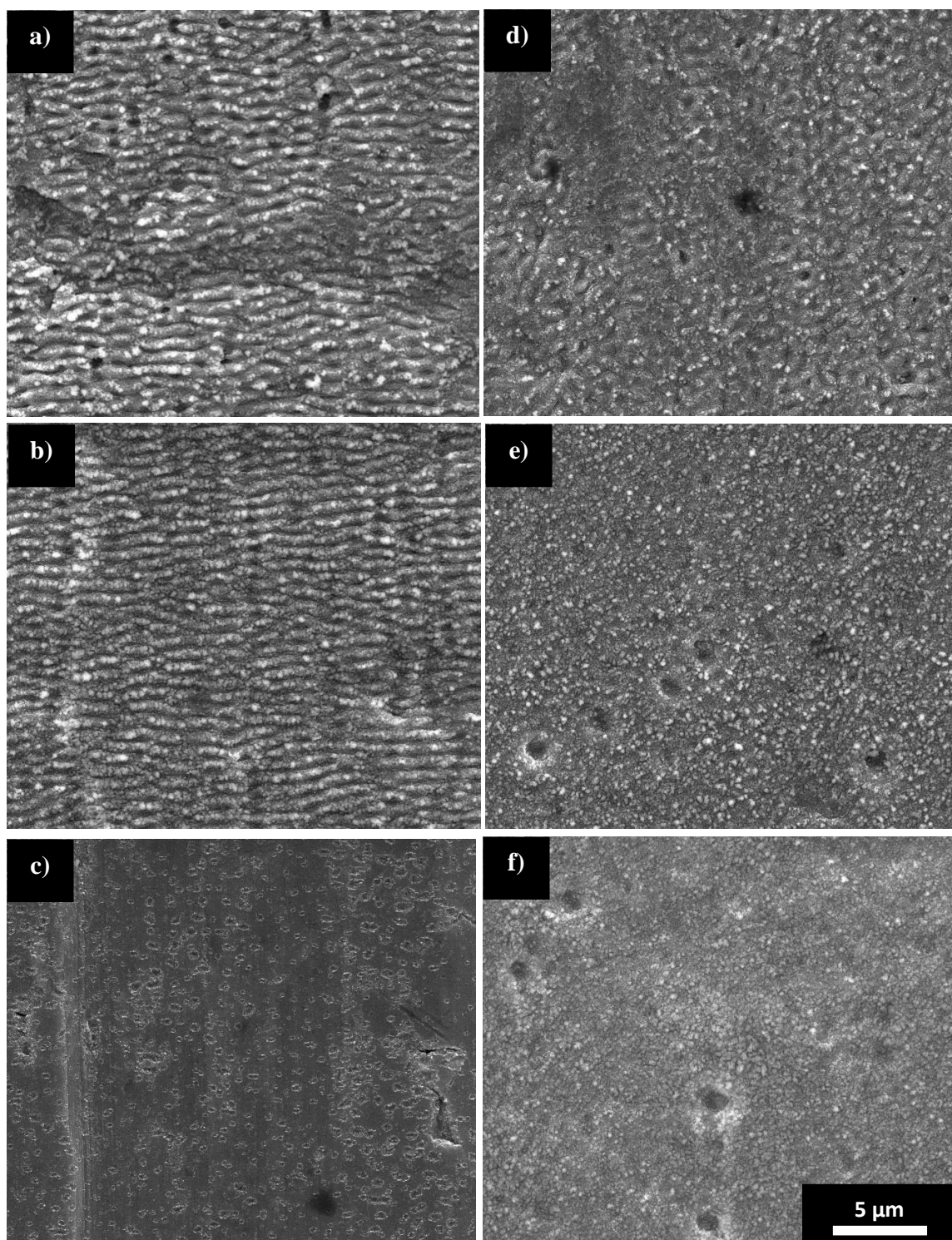


Figure 43 Different laser settings tested for LIPSS. Linearly polarized laser beam a) 27.1 mW, 43 PPS, 90% b) 33.4 mW, 43 PPS, 90% c) 27.1 mW, 9 PPS, 50%. Circularly polarized laser beam with 43 PPS, 90% d) 27.1 mW e) 33.4 mW f) 38.6 mW

7.2 Surface topography characterization of laser micromachined samples

After optimizing the laser settings, sample substrates were prepared for tensile testing. Figure 44 lists the SEM images of all the different inscribed structures. All microstructures also exhibit nanoscale features on top (see insets of Figure 44) confirming the hierarchical nature of femtosecond laser micromachined surfaces. Ripple structures are visible around the entrance of circular holes and even finer structures than ripples are present inside the holes. In contrast, hexagonal holes show traces of redeposited nano particles around the hole entrance, on the hole walls and at the hole bottom. Hence, hexagonal holes are covered with a layer of nano scale roughness which is finer than ripple structures.

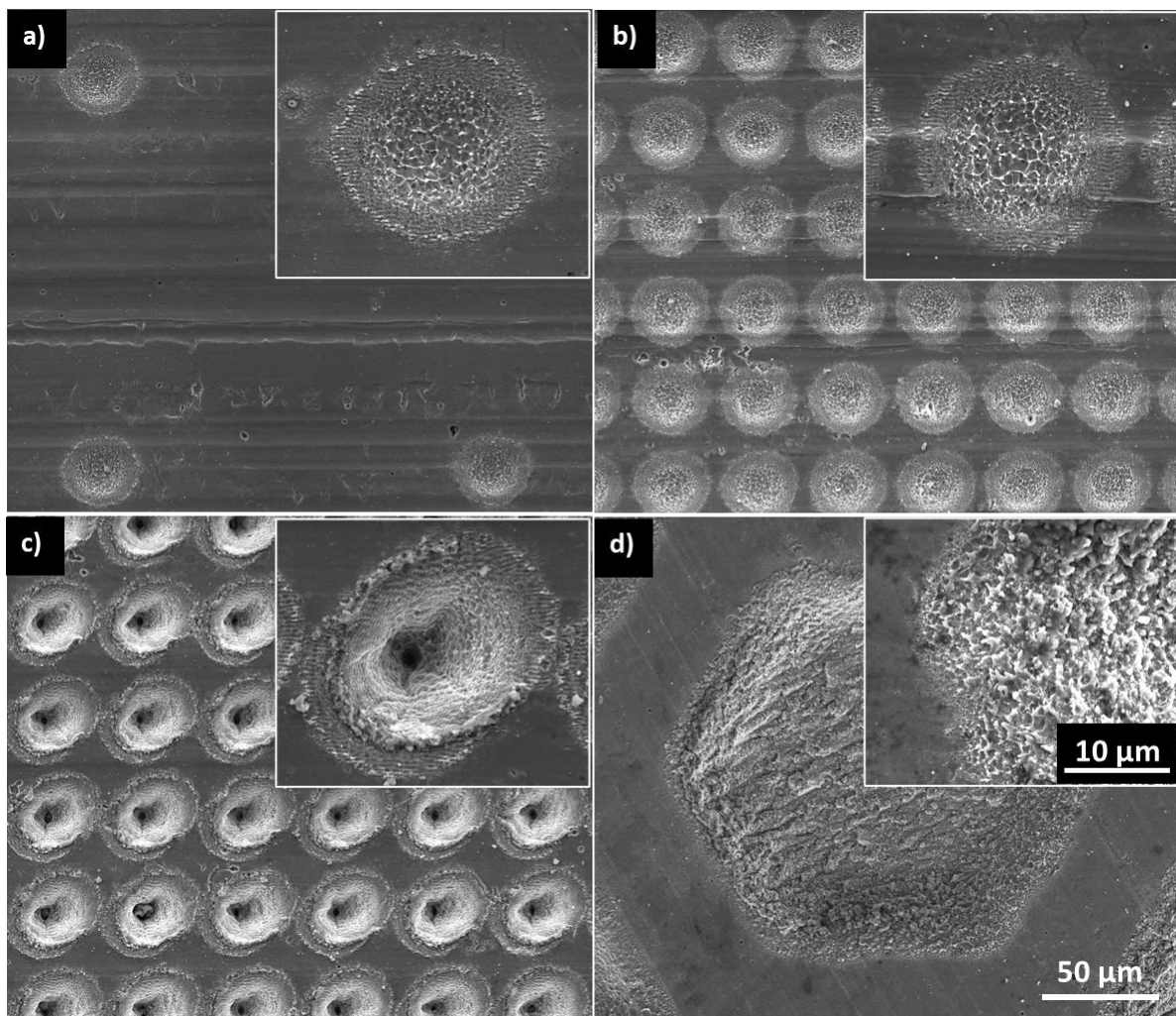


Figure 44 SEM images obtained for different laser micromachined patterns a) CY_P1 b) CY_P2 c) CY_P3 d) HX_P2

3D confocal profilometry images (example in Figure 45) were analyzed to determine the actual geometries of the laser ablated surface structures.

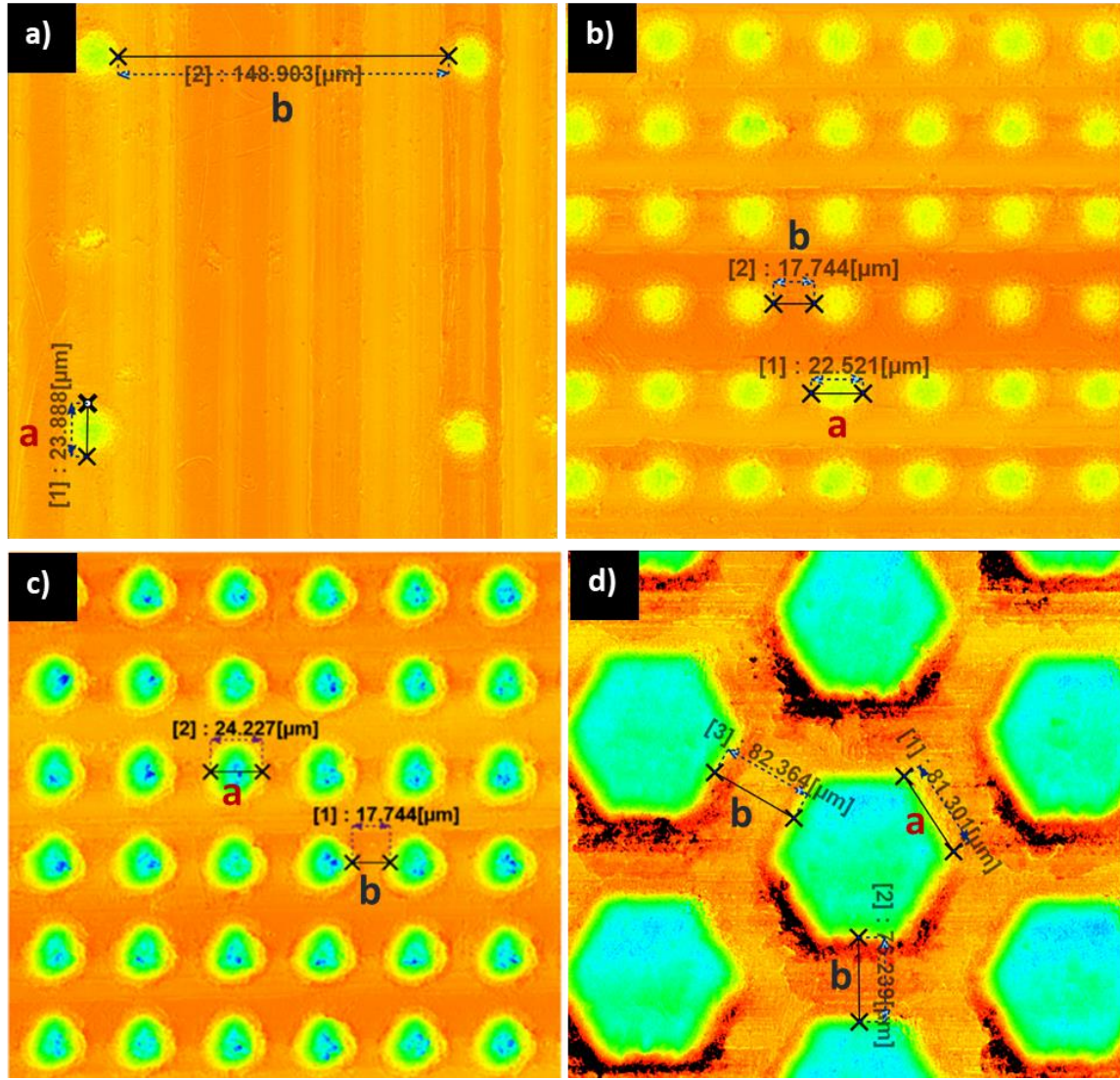


Figure 45 Confocal profilometry images obtained for different laser micromachined patterns a) CY_P1 b) CY_P2 c) CY_P3 d) HX_P2 (example dimensional measurements are presented)

The experimentally measured dimensions and the increased surface roughness data for the prepared laser textured surfaces are summarized in Table 10. Here the notation LIPSS indicates samples with ripple structures and L_LIPSS indicates samples with ripple structures and the additional lauric acid treatment. The resulting dimensions for samples CY_P1, CY_P2, CY_P3, and HX_P2 closely match the requirements from Table 6. They have dimensional accuracy within 5 μm tolerance of the desired geometries.

The increased surface area after the laser micromachining was theoretically calculated for all the substrates. Then the surface area ratio ($= \frac{\text{actual surface area}}{\text{flat surface}}$) was calculated for comparison with adhesion strength results. The increased surface area of the LIPSS samples was calculated by assuming closely packed ripple structures (see APPENDIX IV). For samples CY_P1, CY_P2, CY_P3 and HX_P2, the experimental data a, b and c in Table 10 were used and the

surface area increase due to nanoscale features was estimated using the surface area increase calculated for LIPSS surfaces. Further details of surface area calculations are attached in APPENDIX IV.

Table 10 Characteristic dimensions measured for laser textured substrates

Sample name	a (μm)	b (μm)	c (μm)	Surface area as a ratio to the flat surface
Al_bare	-	-	-	1
LIPSS	-	-	-	1.0185
L_LIPSS	-	-	-	1.0185
CY_P1	25 ± 1	146 ± 1	5 ± 1	1.0014
CY_P2	23 ± 2	19 ± 1	5 ± 0	1.0276
CY_P3	31 ± 2	19 ± 1	23 ± 2	1.2542
HX_P2	82 ± 2	81 ± 4	19 ± 2	1.2240

As can be seen from the SEM images in Figure 44, laser inscribed structures do not exhibit LIPSS nanostructures, but rather random nanostructures originating from nanoparticle redeposition as explained above. Therefore, the accuracy of the surface area calculations can be further improved for CY_P1, CY_P2, CY_P3, and HX_P2. However, this was not pursued further in this analysis due to the sensitivity limitations of the characterization tools available.

7.3 Results and discussion

7.3.1 Adhesion strength at the metal-resin interface

Tensile tests were performed on the above-mentioned laser micromachined samples following the procedure finalized in section 5.2. Figure 46 presents stress evolution plots for all the sample trials with identical axis scales. Stress is plotted against crosshead movement. The true thickness of the resin layer is unknown because the resin may have penetrated into the microcavities. Hence, it was not possible to obtain the stress-strain curves.

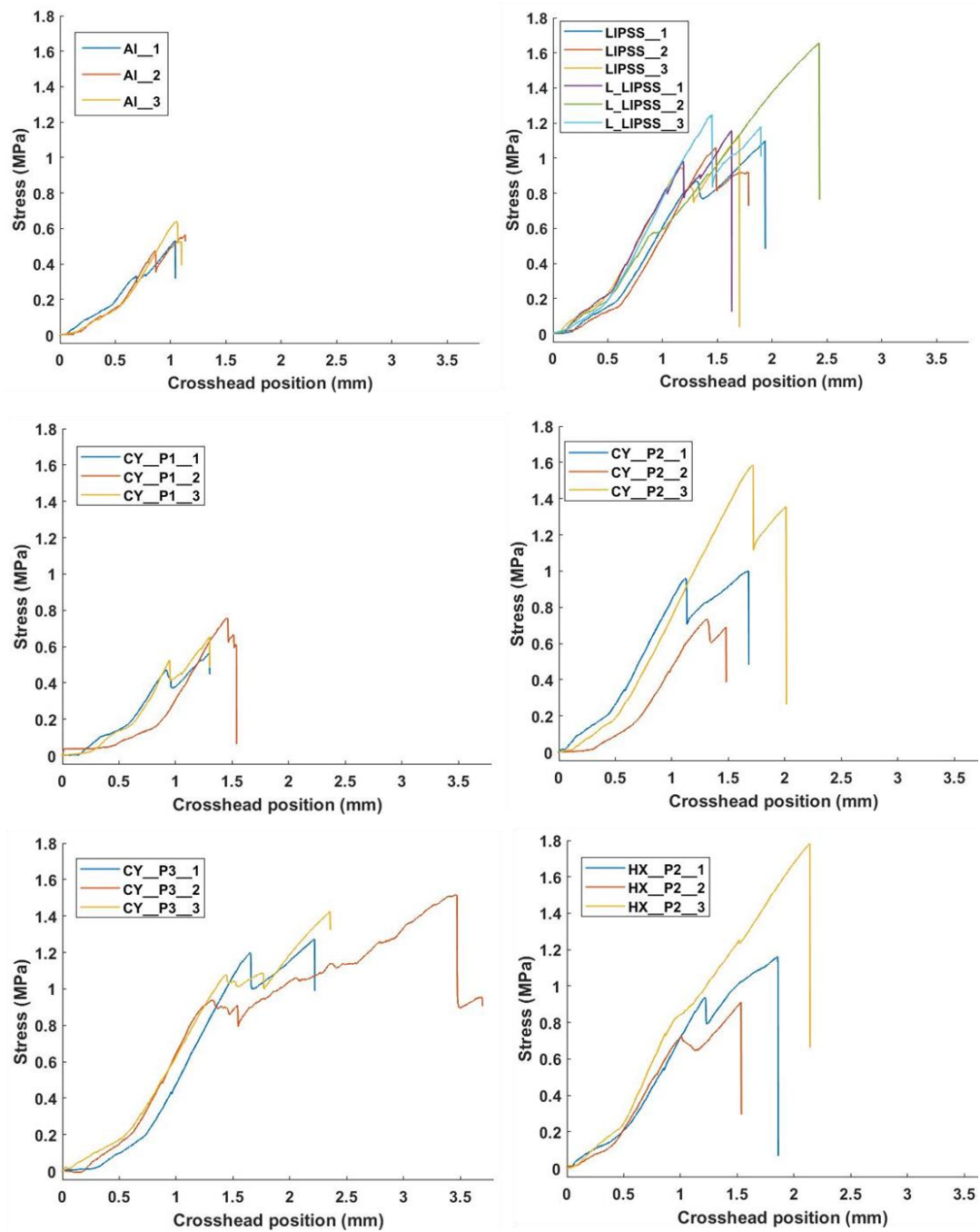


Figure 46 Stress curves reported for Al alloy substrates with different surface topographies

Step failures were common to all the tested specimens, except HX_P2_3 and L_LIPSS_2 which show minor stress fluctuations. These step failures and stress fluctuations indicate an uneven stress distribution from the test fixture to the resin-metal interface which is possibly due to misalignment of the top and bottom traverse or the presence of stress concentration points inside the resin phase and at the resin-metal interface. The LIPSS and L_LIPSS substrates show similar stress behavior with the exception of one sample (L_LIPSS_2), which does not have a step failure and therefore has a higher maximum fracture stress than L_LIPSS_1 and L_LIPSS_3.

All laser machined samples show higher breaking point stress than the bare aluminum alloy samples. CY_P1, which has the lowest density of hole structures, shows almost identical adhesion failures to the bare metal samples. However, all the other substrate patterns have increased the adhesion strength at the resin-metal interface compared to the bare metal surface. The step-failures render stress calculations difficult because of the uncertainty of the actual interfacial area to be considered because by the time a maximum breaking load is recorded, the effective surface area has changed due to the partial delamination by the step failures. However, the stress at the first step failure corresponds to the entire surface area of the resin patch. Therefore, in addition to the maximum breaking stress (Figure 47), the first step-failure (Figure 48) was also used in the analysis. Comparing the stress corresponding to the first peak load should be more accurate. Nevertheless, it is challenging to distinguish the first peak because of minor stress fluctuations. Therefore, a breaking threshold has been defined. In this analysis, if the load reduced more than 10% it was considered a step failure.

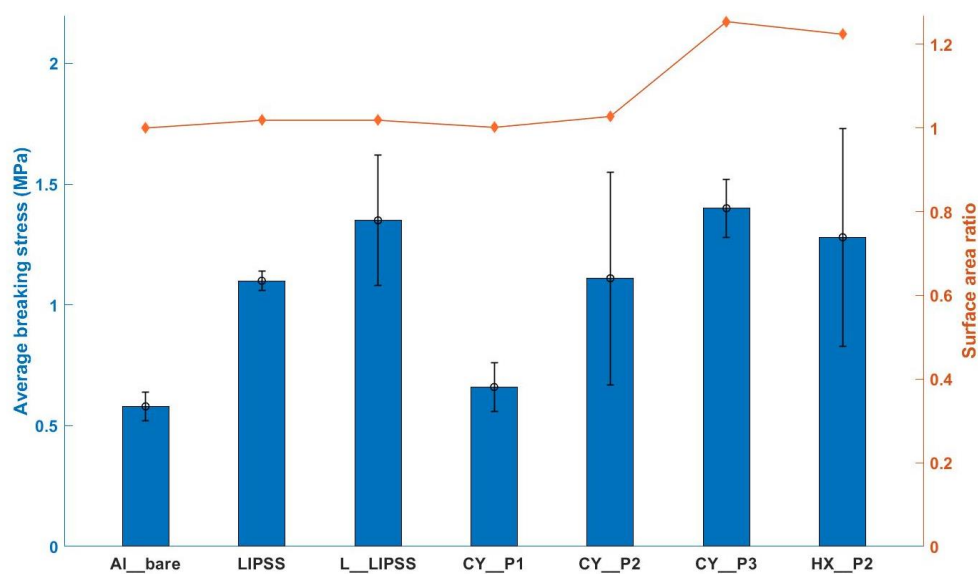


Figure 47 Average maximum breaking stress data obtained for different substrates with comparison to increased surface area

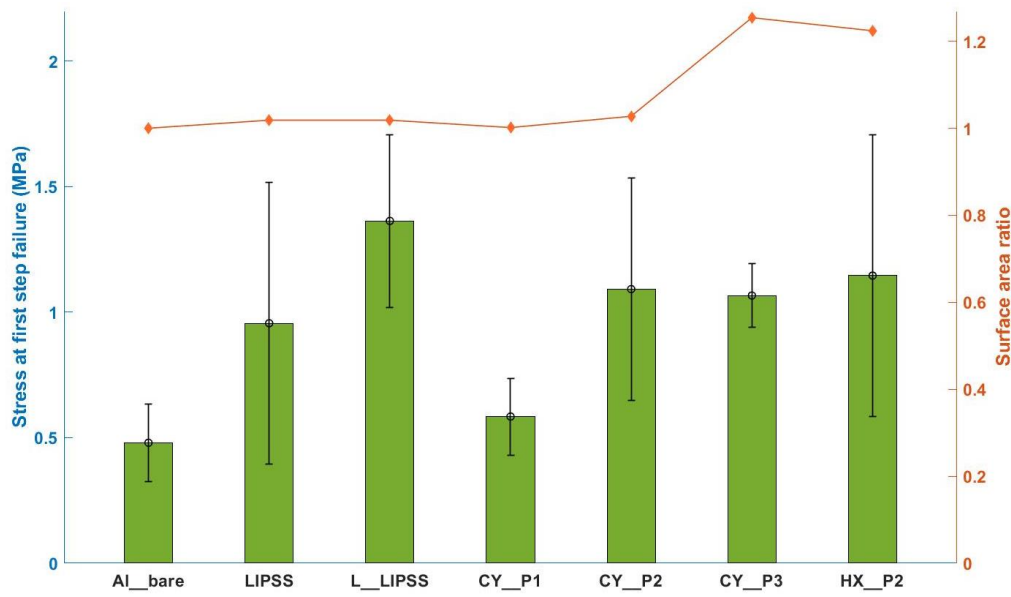


Figure 48 Stress at the first step failure obtained for different substrates with comparison to increased surface area

According to both Figure 47 and Figure 48 plots, the adhesion strength has increased with respect to the increase of metal surface area. This suggests that the liquid resin at least partially penetrated into the micro/nano cavities and increased the interfacial area available for adhesion bond formation. This is further supported by the observation that all the laser modified surfaces reported $\sim 0^\circ$ static contact angle at 60°C (see APPENDIX V), which means that the wettability was higher than the pristine surface after laser micromachining.

Further we note that the maximum peak stress values have a lower standard deviation compared to the first peak stress values. As the laser textured surfaces already show a general trend of increased adhesion compared to the bare metal surface, a one-tailed t-test was performed to check whether the increase in adhesion was statistically significant. Only CY_P3, HX_P2, and ripple structures show a statistically significant ($p < 0.05$) increase in adhesion compared to the bare metal surface according to the probability values of the t-test in Table 11.

Table 11 One-tailed T-test results for maximum breaking stress values reported

Substrate name	Paired T-Test p-value
LIPSS	0.001
L_LIPSS	0.020
CY_P1	0.150
CY_P2	0.072
CY_P3	0.003
HX_P2	0.046

Above results indicate that there is no linear relationship between the adhesion strength and surface area ratio. Hence, in addition to the absolute interfacial area, which will further be discussed in the following section, other factors (e.g. changes to the surface chemistry, nanostructure geometry and possible partial penetration) likely also play a role in determining the overall adhesion strength.

7.3.2 Surface characterization of failed surfaces

After the tensile tests, all failed surfaces were analyzed to further determine the wetting states and failure modes that occurred. The tensile test samples have two resin-metal interfaces because of the nature of the test setup. Hereafter, the resin-metal interface on the bottom substrate is labeled ‘bottom interface’ and the top substrate as ‘top interface’.

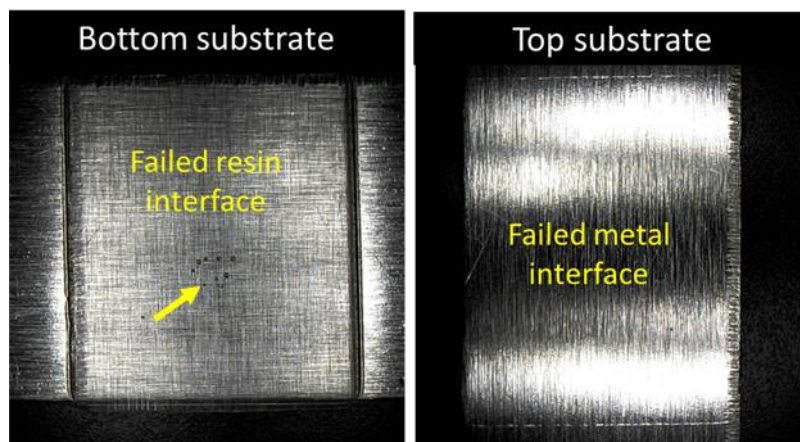


Figure 49 Images of a bare aluminum alloy sample substrates after failure. Yellow arrows: air bubbles.

Bare metal samples showed complete adhesive failure at the top interface as evident in Figure 49, whereas both cohesive and adhesive failure occurred in ripple structured samples. In Figure 50 and Figure 51, traces of the ripple structures are visible on the failed top substrates meaning that both LIPSS and L_LIPSS samples failed mostly near the top interface. Compared to Figure 50e and Figure 51e, which are before resin deposition, the failed counter surface has a negative imprint similar to a ripple pattern. However, due to the nature of the failure, it is challenging to determine if the liquid resin has fully penetrated into the nanoscale valleys between the ripple structures.

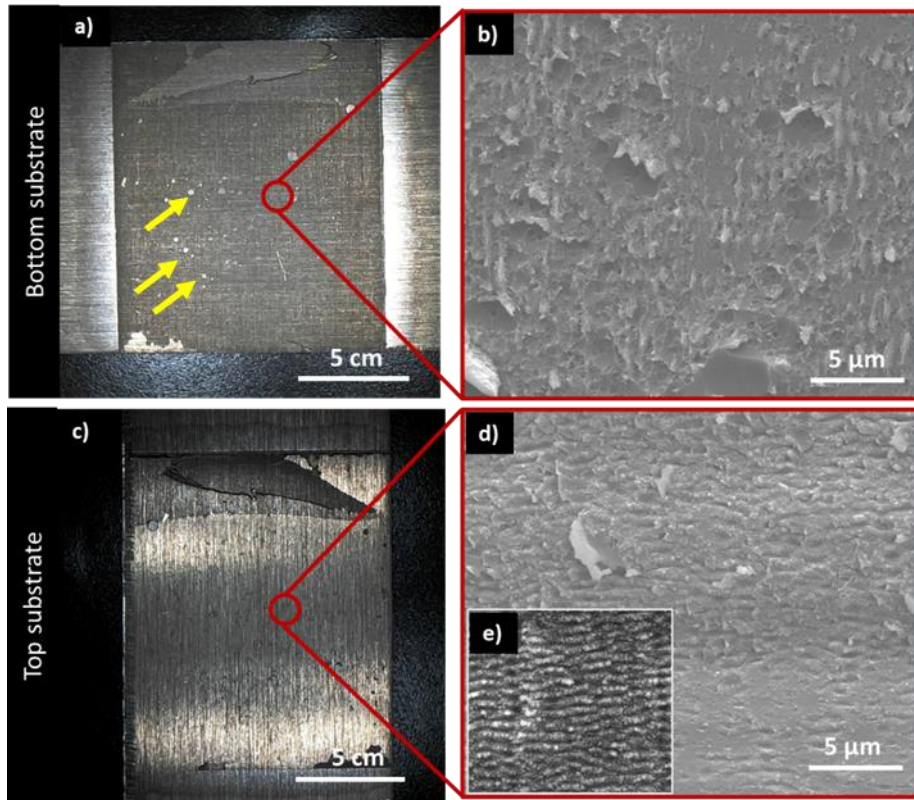


Figure 50 LIPSS failed bottom substrate a) image b) SEM, failed top substrate c) image d) SEM, e) SEM of LIPSS surface before resin casting. Yellow arrows: air bubbles.

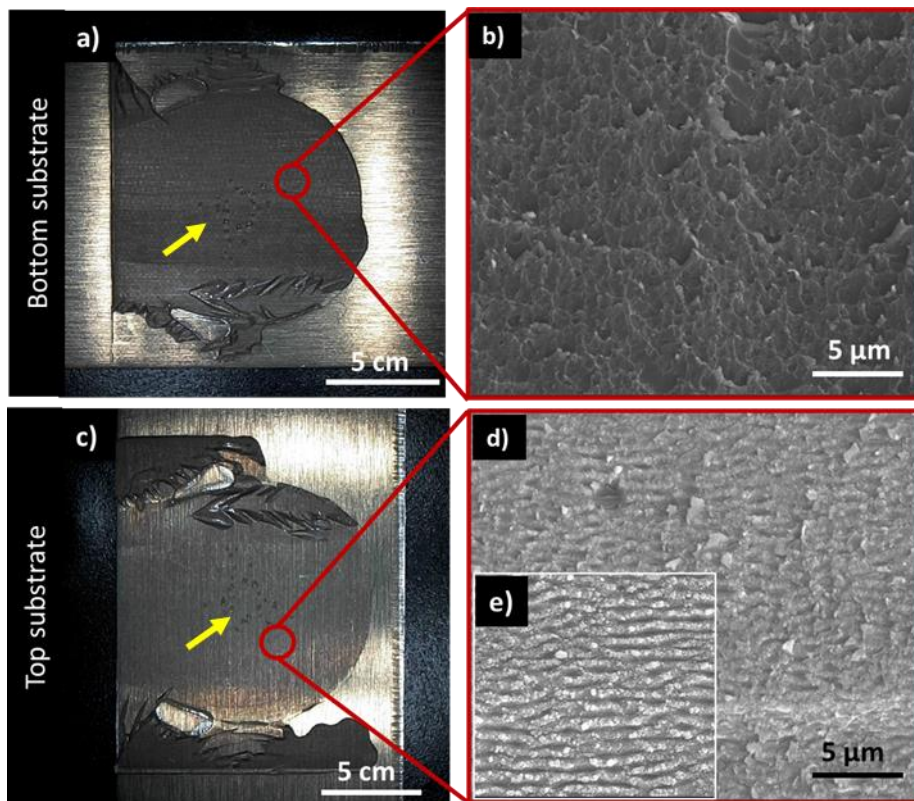


Figure 51 L_LIPSS failed bottom substrate a) image b) SEM, failed top substrate c) image d) SEM, e) SEM of L_LIPSS surface before resin casting. Yellow arrows: air bubbles.

Despite the minor surface area increase, the LIPSS (1.10 ± 0.04 MPa) and L_LIPSS (1.35 ± 0.27 MPa) structures show the most statistically significant increase in adhesion. Meanwhile the difference in surface chemistry introduced by the lauric acid treatment did not affect the wettability of the resins on the ripples. The LIPSS surfaces had polar groups such as hydroxyl ions whereas L_LIPSS had non-polar groups. Yet, there is no significant difference in adhesion strength or the failure mechanism between LIPSS and L_LIPSS. Therefore, possible mechanical interlocking that occurred between the narrow valleys of the ripple structures dominate the adhesion strength. Also, from the discussion in section 6.2.3, it was noted that the presence of a low energy release coating layer did not significantly reduce the resin wettability (only a 35° to 61° increase in contact angle), yet the adhesion was completely avoided. Both of the above results confirm that it is not enough to have non-polar groups on the metal surface and rather a weakly bonded barrier layer to the metal substrate is more effective in detaching a cured resin from the metal substrate.

Figure 52, Figure 53 and Figure 54 summarize microscopy data obtained for failed CY_P1, CY_P2, and CY_P3 samples respectively. The corresponding SEM images of CY_P1 and CY_P2 show perfect imprints from the counter surface topographies. This means, Wenzel wetting, and complete adhesive failure have occurred. Whereas both adhesive and cohesive failure have taken place in CY_P3 samples.

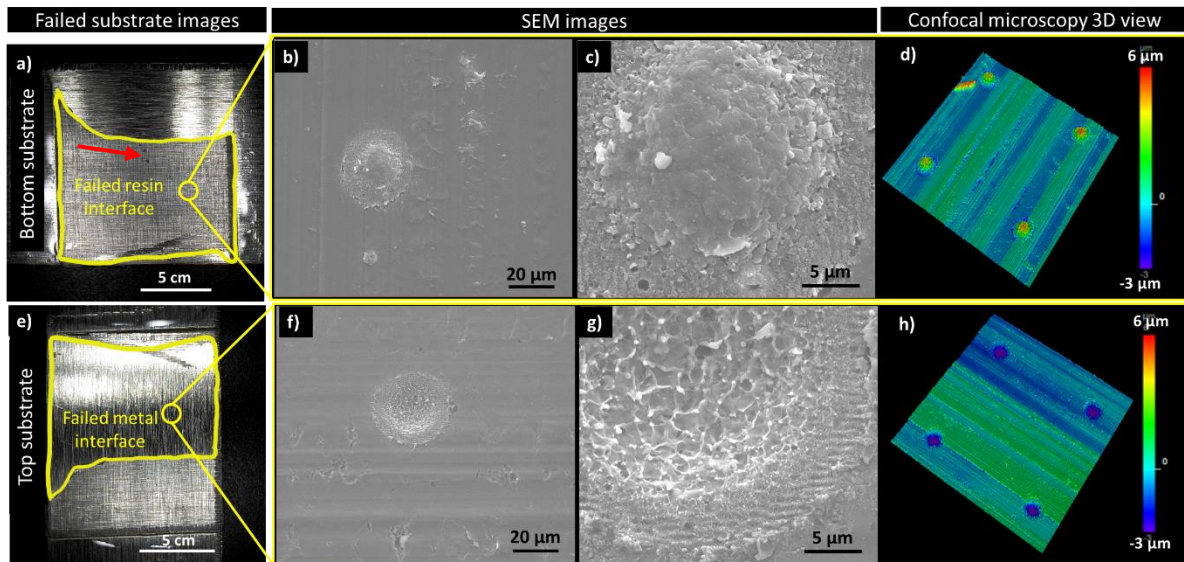


Figure 52 CY_P1 a) failed bottom substrate image b) & c) SEM d) confocal, e) failed top substrate image f) & g) SEM h) confocal. Red arrows: air bubbles.

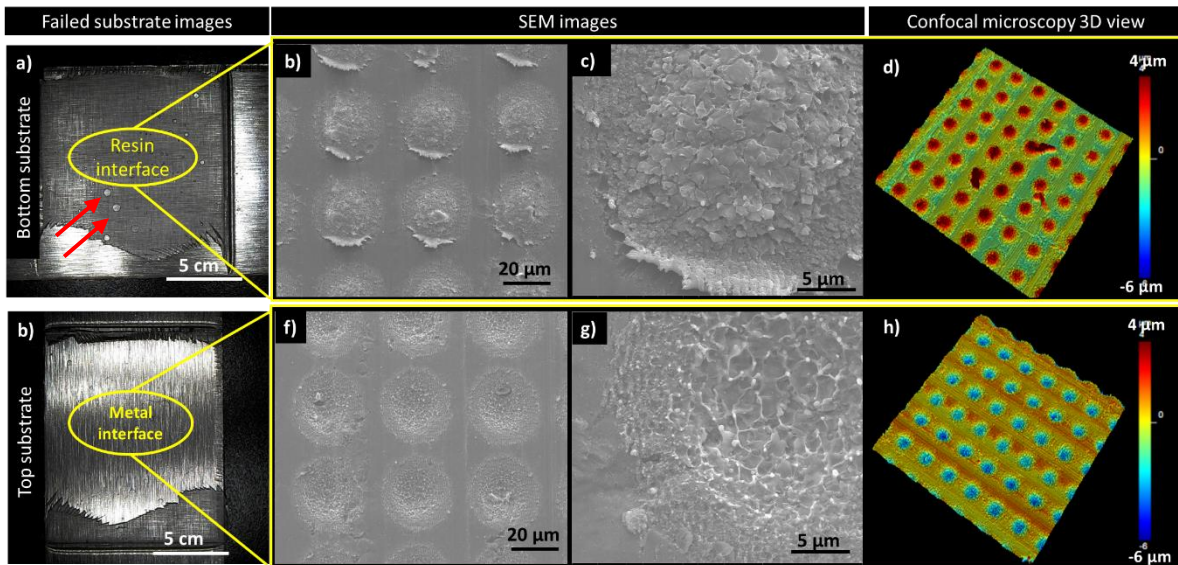


Figure 53 CY_P2 a) failed bottom substrate image b) & c) SEM d) confocal, e) failed top substrate image f) & d) SEM i) confocal. Red arrows: air bubbles.

CY_P3 also demonstrated negative imprints from the counter surface but additionally there are failures that occurred at the resin phase (see yellow arrows in Figure 54b&f). Due to mechanical interlocking, cohesive failure is abundant at such narrow ends of the circular holes in CY_P3. Again, the significant increase of adhesion strength of CY_P3 is explained by the surface area increase, as well as mechanical interlocking. Therefore, the results from CY_P3 samples further support the claim that mechanical interlocking highly contributes to the adhesion strength at the resin-metal interface.

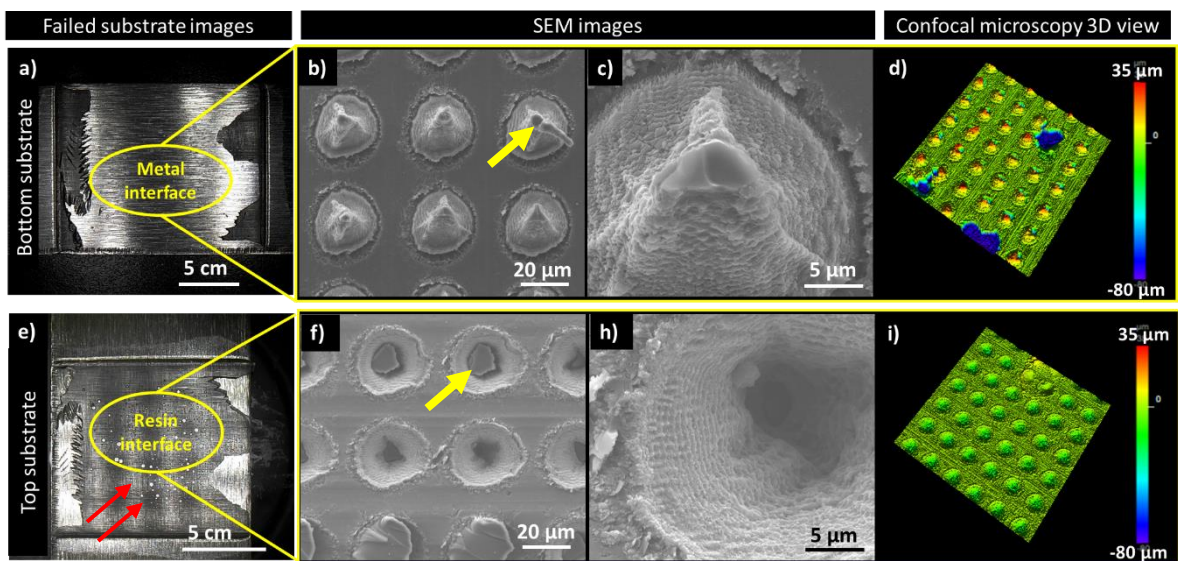


Figure 54 CY_P3 a) failed bottom substrate image b) & c) SEM d) confocal, e) failed top substrate image f) & d) SEM i) confocal. Yellow arrows: locations of cohesive failure. Red arrows: air bubbles.

Hexagonal holes also showed both adhesive and cohesive failure. Complete adhesive failure has occurred in some hexagonal hole locations (yellow arrowheads in Figure 55b&f). The nanoscale surface features present at the bottom of the hexagonal holes are still visible after the resin layer has been detached. Consequently, the resin counter surface shows the negative imprint of the nanoscale features indicating adhesive failure. Interestingly, voids are visible at some hexagonal hole positions as pointed in red arrowheads in Figure 55b and f. Confocal 3D profilometry images in Figure 55d further confirm the presence of air bubbles identified by blue regions which indicate a valley at the interface. Unlike the previously discussed substrates, the air bubbles in the HX_P2 samples coincide with the hexagonal hole positions.

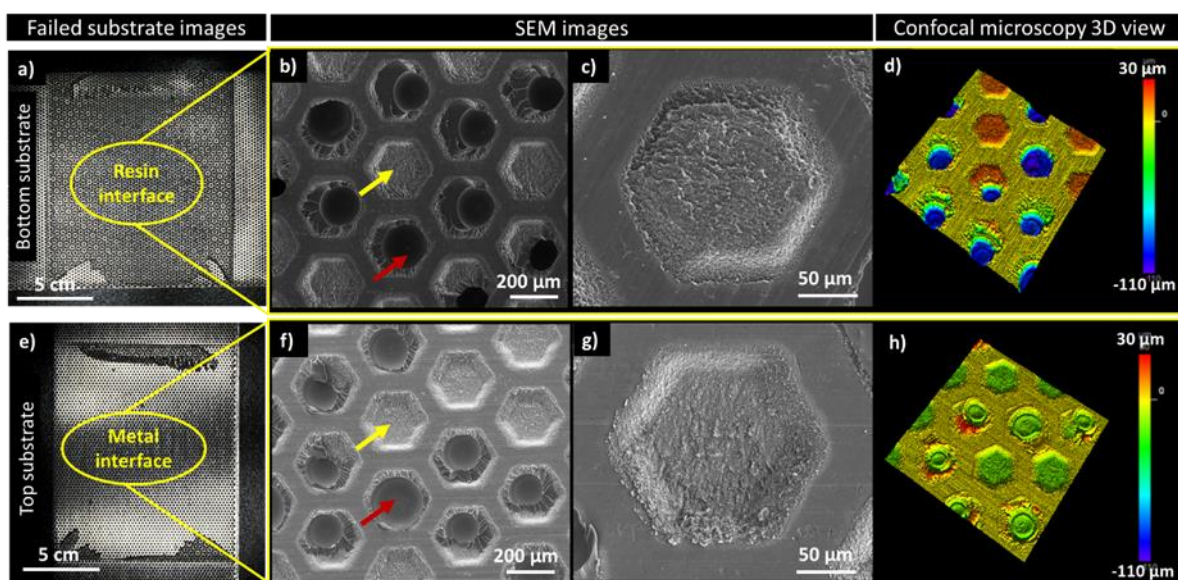


Figure 55 HX_P2 a) failed bottom substrate image b) & c) SEM d) confocal, e) failed top substrate image f) & g) SEM h) confocal

Traces of air bubbles are present on all the failed interfaces. Yellow arrows in Figure 49, Figure 50, Figure 51, and red arrows in Figure Figure 52a, Figure 53a, Figure 54e and Figure 55 indicate such regions of air bubbles. It is important to note that the air bubbles visible in the bare metal and CY_P1 are concentrated in the center of the resin patch and are only present at the top interface. Whereas the voids in the LIPSS, L_LIPSS, CY_P2, and CY_P3 samples are randomly located at the interfaces as merged air bubbles and spread throughout the resin layer thickness. Furthermore, the amount of air bubbles increases in the order of CY_P1 < CY_P2 < CY_P3 where the same ascending order of hole volume per unit area.

All the failed substrate interfaces showed traces of voids. Neither the technical data sheets nor qualitative observations confirm any gaseous by products during the curing reaction of the R2

resin system. However, air bubbles in the resin phase can be caused by two other reasons: (i) air escaping from the micro/nano cavities (ii) air bubbles incorporated into the resin matrix during resin transfer to the substrate.

The voids in bare metal samples and CY_P1 are mostly caused by the latter, as they are only observed at the top interface. Pure adhesive failure of bare metal samples at the top interface is explained by the presence of voids near the top interface. A similar failure mechanism is portrayed for CY_P1. When considering CY_P2 and CY_P3, the total void concentration has clearly increased, proving that the air escaping from the cavities was still trapped in the resin phase and merged into larger voids. This observation correlates with the obvious increase in the microcavity concentration at the interface which indicates that the volume of a cavity plays a role in generating voids in the resin phase.

HX_P2 substrates have a unique air bubbles pattern that deviates from all the other substrates. The quantity of air bubbles is the highest compared to the other substrates and the voids are present at the hexagonal hole positions. The hexagonal hole volume is larger than all the circular hole patterns which seems to have resulted in larger bubbles formation. Therefore, the results of this study indicate that larger/deeper microcavities create more stable voids at the resin-metal interface. According to the first hypothesis of the project, the presence of air pockets at the resin-metal interface should reduce the overall adhesion of the cured resin layer on the metal. However, despite the voids at the resin-metal interface, the sample with hexagonal holes still reports an increased adhesion in comparison to the bare aluminum alloy sample. Closer inspection such as in Figure 56a reveals that resin has penetrated into the holes along the vertical walls and adhered to the walls of the hexagonal hole while entrapping an air pocket in the middle. The cracks around air bubbles (Figure 56a: highlighted in white dashed line) are evidence of resin cohesive failure around the air bubbles with adhesive failure along the pristine metal surface.

Red dashed lines in Figure 57d highlight the surface around the hole entrance that exhibits redeposited nanoparticles. This nanoparticle belt, similar to the LIPSS pattern discussed earlier, heavily contributes to the increase of adhesion strength. Interestingly, adhesive failure still occurred in this region with nanoscale roughness. However, a cohesive failure has occurred around the air bubble. This means that the air bubbles have acted as the weakest point for crack propagation compared to the pathway along the actual resin-metal interface. This is because of the residual stress build-up around the air cavity while resin cures to a solid phase. Due to the difference in thermal expansion coefficients of the resin phase and the air bubble/void, such

stress concentrated points are created around voids. Still, the presence of air-resin interface cannot contribute to the reduction in overall adhesion, because of the nanostructure boundary (region highlighted in red dashed lines in Figure 57d).

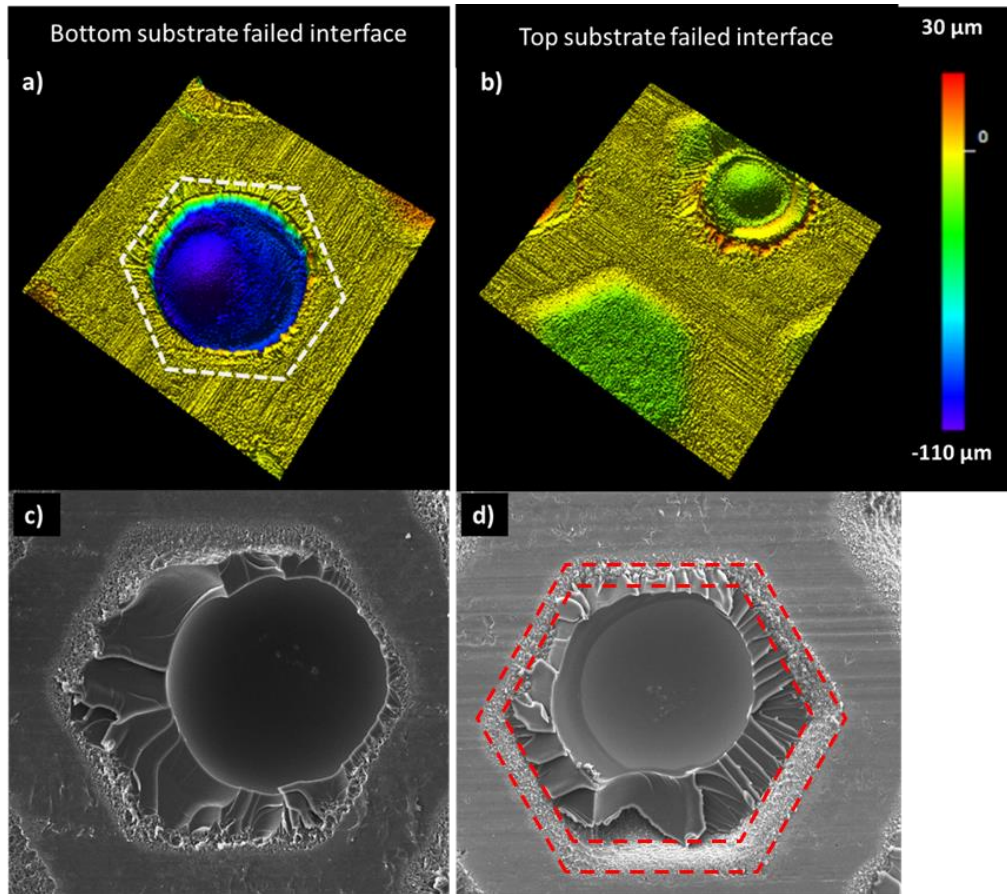


Figure 56 Failed HX_P2 interfaces a) & b) Confocal 3D view image at an air bubble entrapped location (white dashed line: traces of the hexagon on counter surface), c) & d) magnified SEM images of air bubble entrapped hexagonal hole locations (red dashed lines: a belt of redeposited nanoparticles around the hexagon hole entrance)

8 Conclusions

The experimental results proved that the resin system has a high affinity to the pristine metal surface, which is enhanced after laser micromachining. Theoretical analysis revealed that Wenzel wetting is preferred over CB wetting. Accordingly, the experimental observations confirmed that Wenzel wetting occurred on the laser micromachined samples, and the increase in surface area by nanoscale features as well as mechanical interlocking significantly increased the resin-metal adhesion. Thus, the first hypothesis, achieving a CB wetting state that can reduce resin-metal interface area is not valid for the surface textures tested in this project.

The Lauric acid treatment did neither reduce nor increase resin adhesion suggesting that surface chemistry and interfacial area play a minor role and that substrate interlocking is the prominent factor for resin-metal adhesion strength.

The surface topographies tested in this project do not promote lower adhesion. However, the second hypothesis for this research project which was that entrapped air pockets at the resin-metal interface can promote cracks, is still validated by the results because the HX_P2 pattern demonstrates the potential for air trapping and least resistant pathway for crack propagation around such voids. Hexagonal holes entrap air pockets at the interface; however, nanoscale features present around the hexagonal hole entrance significantly contribute to the final adhesion strength which ultimately outweighs any potential adhesion reduction gained by the entrapped voids.

9 Future work

The above conclusions lead to new pathways for achieving decreased resin-metal adhesion. The future suggestions of the project would be as follows.

- i. Optimize the substrate preparation process to avoid nanoparticle redeposition by changing the laser settings and setup to result in less or no nanoparticle redeposition or by integrating a post processing technique to etch the nanoparticle layer.
- ii. Expand the experimental campaign to more surface topographies.
 - a. Hexagonal and circular holes with more than 25 μm hole depth should be investigated as this project concluded that microcavities with more volume can better promote an air-metal composite interface for resin adhesion.
 - b. Closed end reentrant structures could be considered as they are promising for significantly high breakthrough pressure thresholds [35].
- iii. Perform the same set of experiments with the curing step carried out inside a vacuum.
- iv. Fabricate larger surface area samples and cure the resin including the fiber phase as a complete composite layer. The presence of fibers in the resin matrix can affect the liquid resin wettability on the metal surface and the surface topology of the cured composite may be different from a cured resin. Therefore, it is recommended to carry out a similar study with the presence of reinforcing fibers.

Although the results are contrary to the original motivation of the project, the results have possible industrial applications. For example, the LIPSS structures have the potential to improve the bonding of composite-metal components with adhesives. However, the presence of any voids in the adhesive layer should be eliminated in such a case as the presence of voids can lead to adhesion failure of bonded joints. Also, LIPSS surface texturing can be used as a base (primer) for coating applications.

10 Original contributions

The work presented in chapter 5 to 9 are solely carried out by the author of this thesis. The author's original contributions to this master's thesis are as follows.

- i. A novel methodology was developed to quantitatively measure the adhesion strength of resin to metal under a tensile force.
- ii. A procedure was developed to measure the contact angle of epoxy on a metal substrate at elevated temperature conditions.
- iii. Laser micromachining settings were optimized for the AA6061 aluminum alloy material to fabricate laser inscribed structures and laser induced structures.
- iv. Epoxy resin adhesion strength testing and interpretation of results were carried out against 6 different surface modified substrate categories.

11 References

- [1] "Industry Trend: Aerospace composite market," Global Market Insights, 2021. Accessed: 2021 December. [Online]. Available: <https://www.gminsights.com/industry-analysis/aerospace-composites-market>
- [2] F. C. Campbell, *Structural composite materials*, Materials Park, Ohio: ASM International, 2010. [Online]. Available: <http://site.ebrary.com/id/10439480>.
- [3] Z. Hasan, *Tooling for composite aerospace structures manufacturing and applications*, Oxford: Butterworth-Heinemann, 2020. [Online]. Available: <https://www.sciencedirect.com/science/book/9780128199572>
<http://search.ebscohost.com/login.aspx?direct=true&scope=site&db=nlebk&db=nlabk&AN=2367360>.
- [4] G. W. Critchlow, R. E. Litchfield, I. Sutherland, D. B. Grandy, and S. Wilson, "A review and comparative study of release coatings for optimised adhesion in resin transfer moulding applications," *International Journal of Adhesion and Adhesives*, vol. 26, no. 8, pp. 577-599, 2006, doi: 10.1016/j.ijadhadh.2005.09.003.
- [5] I. Snowdon and M. Rigby, "New developments in release agent technologies," *Reinforced Plastics*, vol. 50, no. 10, pp. 24-28, 2006, doi: 10.1016/S0034-3617(06)71159-6.
- [6] C. A. S. John Meyer, "Effect of Silicone contamination on assembly processes," presented at the APEX EXPO, 2012.
- [7] Z. Xiuli, L. Zhilan, W. Xu, X. Xiufang, W. Yongling, and W. Diben, "Comparative Study of Anti-Sticking Properties of Coatings for Tire Molds," vol. 12, no. 1740, p. 1740doi: 10.3390/coatings12111740.
- [8] J. I. Lozano, J. I. Amor, and M. Borro, "Corrosion protection on texturized steel moulds for polymeric products by sol-gel anti-adherent coatings," *Journal of Adhesion Science and Technology*, pp. 1-11, 2022, doi: 10.1080/01694243.2022.2145635.
- [9] I. A. Melamies. process produces anti-adhesion coating directly in the mold. *Moldmaking technology magazine*. Available: https://www.plasmatreat.com/downloads/english/11-10_MMT_anti-adhesion-coating-in-mold.pdf
- [10] J. Meng, X. Dong, X. Wei, and Z. Yin, "Preparation of anti-adhesion surfaces on aluminium substrates of rubber plastic moulds using a coupling method of liquid

- plasma and electrochemical machining," *AIP Advances*, vol. 4, no. 3, 2014, doi: 10.1063/1.4867245.
- [11] E. Stratakis *et al.*, "Laser engineering of biomimetic surfaces," *Materials Science & Engineering R*, vol. 141, 2020, doi: 10.1016/j.mser.2020.100562.
 - [12] T. Kong, G. Luo, Y. Zhao, and Z. Liu, "Bioinspired Superwettability Micro/Nanoarchitectures: Fabrications and Applications," *Advanced Functional Materials*, vol. 29, no. 11, 2019, doi: 10.1002/adfm.201808012.
 - [13] P. Fan, R. Pan, and M. Zhong, "Ultrafast Laser Enabling Hierarchical Structures for Versatile Superhydrophobicity with Enhanced Cassie–Baxter Stability and Durability," *Langmuir*, vol. 35, no. 51, pp. 16693-16711, 2019/12/24 2019, doi: 10.1021/acs.langmuir.9b02986.
 - [14] M. Malinauskas *et al.*, "Ultrafast laser processing of materials: from science to industry," *Light, Science & Applications*, vol. 5, no. 8, p. e16133, 2016, doi: 10.1038/lsa.2016.133.
 - [15] D. Du, X. Liu, G. Korn, J. Squier, and G. Mourou, "Laser-induced breakdown by impact ionization in SiO₂ with pulse widths from 7 ns to 150 fs," *Applied Physics Letters*, vol. 64, no. 23, pp. 3071-3073, 1994, doi: 10.1063/1.111350.
 - [16] K. Ahmmed, C. Grambow, and A.-M. Kietzig, "Fabrication of Micro/Nano Structures on Metals by Femtosecond Laser Micromachining," *Micromachines*, vol. 5, no. 4, pp. 1219-1253, 2014, doi: 10.3390/mi5041219.
 - [17] J. Cheng *et al.*, "A review of ultrafast laser materials micromachining," *Optics & Laser Technology*, vol. 46, pp. 88-102, 2013/03/01/ 2013, doi: <https://doi.org/10.1016/j.optlastec.2012.06.037>.
 - [18] J. Lehr and A.-M. Kietzig, "Production of homogenous micro-structures by femtosecond laser micro-machining," *Optics and Lasers in Engineering*, vol. 57, pp. 121-129, 2014, doi: 10.1016/j.optlaseng.2014.01.012.
 - [19] W. Perrie, M. Gill, G. Robinson, P. Fox, and W. O'Neill, "Femtosecond laser micro-structuring of aluminium under helium," *Applied Surface Science*, vol. 230, no. 1, pp. 50-59, 2004, doi: 10.1016/j.apsusc.2003.12.035.
 - [20] A.-M. K. Nithin Joy, "Role of Surface Chemistry on Wettability of Laser Machined Metallic Surfaces " McGill University, Book Chapter, 2022.
 - [21] J. Krüger and W. Kautek, "Ultrashort Pulse Laser Interaction with Dielectrics and Polymers," in *Polymers and Light*, T. K. Lippert Ed. Berlin, Heidelberg: Springer Berlin Heidelberg, 2004, pp. 247-290.

- [22] S. Sarbada and Y. C. Shin, "Superhydrophobic contoured surfaces created on metal and polymer using a femtosecond laser," *Applied Surface Science*, vol. 405, pp. 465-475, 2017/05/31/ 2017, doi: <https://doi.org/10.1016/j.apsusc.2017.02.019>.
- [23] J. Bonse, J. Kruger, S. Hohm, and A. Rosenfeld, "Femtosecond laser-induced periodic surface structures," *Journal of Laser Applications*, vol. 24, no. 4, 2012, doi: 10.2351/1.4712658.
- [24] J.-M. Romano *et al.*, "Springtail-Inspired Triangular Laser-Induced Surface Textures on Metals Using MHz Ultrashort Pulses," *Journal of Micro and Nano-Manufacturing*, vol. 7, no. 2, 2019, doi: 10.1115/1.4043417.
- [25] J.-M. Romano, A. Garcia-Giron, P. Penchev, and S. Dimov, "Triangular laser-induced submicron textures for functionalising stainless steel surfaces," *Applied Surface Science*, vol. 440, pp. 162-169, 2018/05/15/ 2018, doi: <https://doi.org/10.1016/j.apsusc.2018.01.086>.
- [26] Y. Assaf, "Femtosecond laser micromachining of polymer surfaces," Doctor of Philosophy, Chemical Engineering department, McGill University, 2018.
- [27] J. r. Bonse and S. Gräf, "Maxwell Meets Marangoni—A Review of Theories on Laser-Induced Periodic Surface Structures," *Laser & Photonics Reviews*, vol. 14, no. 10, p. 2000215, 2020, doi: 10.1002/lpor.202000215.
- [28] U. Hermens *et al.*, "Mimicking lizard-like surface structures upon ultrashort laser pulse irradiation of inorganic materials," *Applied Surface Science*, vol. 418, pp. 499-507, 2017/10/01/ 2017, doi: <https://doi.org/10.1016/j.apsusc.2016.12.112>.
- [29] A. M. Kietzig, S. G. Hatzikiriakos, and P. Englezos, "Patterned superhydrophobic metallic surfaces," *Langmuir : the ACS journal of surfaces and colloids*, vol. 25, no. 8, pp. 4821-7, 2009, doi: 10.1021/la8037582.
- [30] J. Long, M. Zhong, H. Zhang, and P. Fan, "Superhydrophilicity to superhydrophobicity transition of picosecond laser microstructured aluminum in ambient air," *Journal of Colloid And Interface Science*, vol. 441, pp. 1-9, 2015, doi: 10.1016/j.jcis.2014.11.015.
- [31] L. B. Boinovich, A. M. Emelyanenko, K. A. Emelyanenko, A. G. Domantovsky, and A. A. Shiryaev, "Comment on “Nanosecond laser textured superhydrophobic metallic surfaces and their chemical sensing applications” by Duong V. Ta, Andrew Dunn, Thomas J. Wasley, Robert W. Kay, Jonathan Stringer, Patrick J. Smith, Colm Connaughton, Jonathan D. Shephard (Appl. Surf. Sci. 357 (2015) 248-254)," *Applied Surface Science*, vol. 379, pp. 111-113, 2016, doi: 10.1016/j.apsusc.2016.04.056.

- [32] N. Joy and A.-M. Kietzig, "Role of machining and exposure conditions on the surface chemistry modification of femtosecond laser-machined copper surfaces," *Surfaces and Interfaces*, vol. 37, 2023, doi: 10.1016/j.surfin.2023.102657.
- [33] J. W. Michael, S. Phillip, and K. Anne-Marie, "The Tuning of LIPSS Wettability during Laser Machining and through Post-Processing," vol. 11, no. 973, p. 973doi: 10.3390/nano11040973.
- [34] A. Starostin *et al.*, "Robust Technique Allowing the Manufacture of Superoleophobic (Omniphobic) Metallic Surfaces[Surface te]," *Advanced Engineering Materials*, vol. 16, no. 9, pp. 1127-1132, 2014, doi: 10.1002/adem.201300561.
- [35] R. Hensel, C. Neinhuis, and C. Werner, "The springtail cuticle as a blueprint for omniphobic surfaces," *Chemical Society reviews*, vol. 45, no. 2, pp. 323-41, 2016, doi: 10.1039/c5cs00438a.
- [36] Q. S. Zheng, Y. Yu, and Z. H. Zhao, "Effects of Hydraulic Pressure on the Stability and Transition of Wetting Modes of Superhydrophobic Surfaces," *LANGMUIR*, vol. 21, no. 26, pp. 12207-12212, 2005.
- [37] S. A. Page, J. C. Berg, and J. A. E. Manson, "Characterization of epoxy resin surface energetics," *JOURNAL OF ADHESION SCIENCE AND TECHNOLOGY*, vol. 15, no. Part 2, pp. 153-170, 2001.
- [38] B. Ellis, *Chemistry and Technology of Epoxy Resins*, Dordrecht: Springer Netherlands, 1993. [Online]. Available: <https://public.ebookcentral.proquest.com/choice/publicfullrecord.aspx?p=3069404>
<https://doi.org/10.1007/978-94-011-2932-9>.
- [39] L. Chen and E. Bonaccorso, "Effects of surface wettability and liquid viscosity on the dynamic wetting of individual drops," *Physical review. E, Statistical, nonlinear, and soft matter physics*, vol. 90, no. 2, p. 022401, 2014.
- [40] G. Zitzenbacher, Z. Huang, M. Längauer, C. Forsich, and C. Holzer, "Wetting behavior of polymer melts on coated and uncoated tool steel surfaces," *Journal of Applied Polymer Science*, vol. 133, no. 21, 2016, doi: 10.1002/app.43469.
- [41] G. Zitzenbacher, H. Dirnberger, M. Längauer, and C. Holzer, "Calculation of the Contact Angle of Polymer Melts on Tool Surfaces from Viscosity Parameters," *Polymers*, vol. 10, no. 1, 2017, doi: 10.3390/polym10010038.
- [42] F. N. A.Tcharkhtchi, S.Khelladi, J.Fitoussi, S.Farzaneh, "Epoxy/amine reactive systems for composites materials and their thermomechanical properties," in *Advances in Composites Manufacturing and Process Design*, 2015, ch. 13.

- [43] Y. Li, Y. Xiao, L. Yu, K. Ji, and D. Li, "A review on the tooling technologies for composites manufacturing of aerospace structures: materials, structures and processes," *Composites Part A: Applied Science and Manufacturing*, vol. 154, p. 106762, 2022/03/01/ 2022, doi: <https://doi.org/10.1016/j.compositesa.2021.106762>.
- [44] K. Hodd, *Comprehensive Polymer Science and Supplements* 1989.
- [45] J. P. B. Randall G. Schmidt, "Epoxy adhesion to metals," presented at the Advances in polymer science, 1986.
- [46] M. J. Wood and A.-M. Kietzig, "Factors Influencing the Formation, Adhesion, and Friction of Ice," in *Ice Adhesion*: John Wiley & Sons, Inc. : Hoboken, NJ, USA, 2020, pp. 1-54.
- [47] S. Omairey, N. Jayasree, and M. Kazilas, "Defects and uncertainties of adhesively bonded composite joints," *SN Applied Sciences*, vol. 3, no. 9, p. 769, 2021/08/06 2021, doi: 10.1007/s42452-021-04753-8.
- [48] S. Motagi and S. Namilae, "In-Situ Investigation of Resin Shrinkage in the Composite Manufacturing Environment," *Applied Composite Materials : An International Journal for the Science and Application of Composite Materials*, vol. 28, no. 3, pp. 651-657, 2021, doi: 10.1007/s10443-021-09887-x.
- [49] R. Sfar Zbed, V. Sobotka, and S. Le Corre, "A Three-Dimensional Thermo-Chemical Characterization During the Whole Curing Cycle of a Carbon / Epoxy Prepreg," *ESAFORM 2021*, 2021, doi: 10.25518/esaform21.2067.
- [50] L. Liang, L. Lu, D. Xing, Z. Wan, and Y. Tang, "Preparation of superhydrophobic and anti-resin-adhesive surfaces with micro/nanoscale structures on high-speed steel via laser processing," *Surface & Coatings Technology*, vol. 357, pp. 57-68, 2019, doi: 10.1016/j.surfcoat.2018.10.001.
- [51] M. Mund, K. Lippky, D. Blass, and K. Dilger, "Influence of production based surface topography and release agent amount on bonding properties of CFRP," *Composite Structures*, vol. 216, pp. 104-111, 2019, doi: 10.1016/j.compstruct.2019.02.026.
- [52] P. He, K. Chen, and J. Yang, "Surface modifications of Ti alloy with tunable hierarchical structures and chemistry for improved metal-polymer interface used in deepwater composite riser," *Applied Surface Science*, vol. 328, pp. 614-622, 2015, doi: 10.1016/j.apsusc.2014.12.081.
- [53] S. A. Aleksandar Vencl, Gregory Favaro, Fatima Zivic, Mihailo Mrdak, Slobodan Mitrović, Vladimir Popovic, "Evaluation of adhesion/cohesion bond strength of the thick plasma spray coatings by scratch testing on coatings cross-sections," *Tribology*

- International*, vol. 44, no. 11, pp. 1281-1288, 2011, doi: <https://doi.org/10.1016/j.triboint.2011.04.002>.
- [54] M. B. Asadi, D. G. K. Aboud, M. J. Wood, G. Zeppetelli, and A.-M. Kietzig, "A new insight into dynamic contact angle measurements: Implementation of smooth splines method," *Colloids and Surfaces A: Physicochemical and Engineering Aspects*, vol. 655, p. 130234, 2022/12/20/ 2022, doi: <https://doi.org/10.1016/j.colsurfa.2022.130234>.
- [55] "Stability of the non-wetting state in a droplet impinging on surfaces with multiple holes," *Physics of fluids*, vol. 33, no. 12, 2021.
- [56] S. Fordham, "On the Calculation of Surface Tension from Measurements of Pendant Drops," *Proceedings of the Royal Society of London. Series A, Mathematical and Physical Sciences*, vol. 194, no. 1036, pp. 1-16, 1948.

12 APPENDIX

APPENDIX I: Preliminary resin contact angle results

Trial	Time after resin prepared (hours)	Roughness Sa (μm)	Wetting nature	Temperature increasing region			
				Starting CA at 30 °C	Ending CA at 60 °C	CA decreasing rate (deg/°C)	Average temperature increasing rate (°C/s)
1	0.5	1.537	Anisotropic	24.89	15	0.33	0.11
2	1.75	1.633	Anisotropic	39.16	35.5	0.12	0.20
3	3	1.791	Anisotropic	43.51	35.62	0.26	0.83
4	4	1.606	Anisotropic	41	37.8	0.11	0.65
5	4.75	1.678	-	41.51	33.07	0.28	0.19
6	5.5	1.634	Anisotropic	47	32.02	0.50	0.22
7	6	1.498	Almost isotropic	39.49	29.57	0.33	0.21
8	6.5	1.660	Anisotropic	34.2	19.52	0.49	0.33
9	7	1.727	Anisotropic	48.35	40.52	0.26	0.27
10	7.5	1.610	Almost isotropic	43.37	36.77	0.22	0.21
11	8.5	1.112	Almost isotropic	47.86	43.31	0.15	0.15
12*	-	1.115	Isotropic	59.21	44.36	0.50	0.11

* aluminum alloy sample in Figure 33

APPENDIX II: Optimization code for cylindrical holes

```
@author: shash
"""
#----- CODE FOR CYLINDRICAL HOLES -----

import math

# Input data variables
theta=34.6 # the young's CA in degrees
theta_radian=theta*math.pi/180
Gamma_la=0.007469 # Surface tension of resin (R2 resin system) to air in N/m
edge_angle=-90 # Angle of the grooves or holes
edge_angle_radian=edge_angle*math.pi/180

# solution lists for stable Cassie state
a_list=[]
b_list=[]
c_list=[]
theta_CB_list_1=[]
G_W_list=[] # Gibb's energy list for Cassie state
G_CB_list=[] # Gibb's energy list for Wenzel state
delta_G_list=[]

# solution lists for metastable cassie state
Energy_gap=[]
A_list=[]
B_list=[]
C_list=[]
theta_CB_list_2=[]

# solution lists for pressure approach
Pb_list=[]
P_a_list=[]
P_b_list=[]
P_c_list=[]
P_theta_CB_list=[]
P_delta_G_list=[]

Energy_gap_list2=[]
C_list2=[]

# a - size of a side
# b - minimum spacing between two hexagons
# c - hexagon hole depth

# the dimensions a_Um, b_Um, c_Um provided in microns
for a_Um in [25,30,35]: # Should be larger than beam effective diameter
    for b_Um in range(12,150): # Should be larger than shutter open + shutter close required distances
        for c_Um in range(5,200): # no limitations except laser settings such as overscans number
            a=a_Um*10**(-6) # converting to m from microns
            b=b_Um*10**(-6)
            c=c_Um*10**(-6)

            A_unitcell=(a+b)**2
            L=math.pi*a # L - perimeter of the three phase contact line
```

```

# Cassie-Baxter state
A_sl_CB=((a+b)**2)-(math.pi*a**2)/4
f=A_sl_CB/A_unitcell
Cos_theta_CB=f*math.cos(theta_radian)+f-1 # CA at Cassie state

A_la_CB=(2*(a+b)**2/(1+Cos_theta_CB))+(math.pi*a**2/4)
G_CB=Gamma_la*(A_la_CB-A_sl_CB*math.cos(theta_radian)) # Gibbs energy change at Cassie-
Baxter state

# Wenzel state
A_sl_W=A_unitcell+math.pi*a*c
r=A_sl_W/A_unitcell
Cos_theta_W=r*(math.cos(theta_radian))

A_la_W=(2*A_unitcell)/(1+math.cos(Cos_theta_W))
G_W=Gamma_la*(A_la_W-A_sl_W*math.cos(theta_radian)) # Gibbs energy change at Wenzel state

if -1<Cos_theta_CB<1:
    if -1<Cos_theta_W<1: # filter out the unrealistic CA values
        if G_W>G_CB: # Finding the most stable energy state

            a_list.append(a_Um)
            b_list.append(b_Um)
            c_list.append(c_Um)
            theta_CB_list_1.append(180*math.acos(Cos_theta_CB)/math.pi)
            G_W_list.append(G_W)
            G_CB_list.append(G_CB)
            delta_G_list.append(G_W-G_CB) # take the energy gap at the two wetting states

        elif G_W<G_CB : # Analyzing the metastable state
            n=c*L/A_sl_CB # N - pillar slenderness ratio (HL/A)
            E=-n*f*math.cos(theta_radian)*Gamma_la # Energy barrier calculation for Cassie to Wenzel
transfer
            Energy_gap.append(E)
            A_list.append(a_Um)
            B_list.append(b_Um)
            C_list.append(c_Um)
            theta_CB_list_2.append(180*math.acos(Cos_theta_CB)/math.pi)

            # Breakthrough pressure calculations (independent from the c dimension)
            lamda=A_sl_CB/L
            delta_P=-4*Gamma_la*math.cos(theta_radian)/a
            #delta_P=-(Gamma_la*f*math.cos(theta_radian))/(1-f)/lamda
            Pb_list.append(delta_P)
            P_a_list.append(a_Um)
            P_b_list.append(b_Um)
            P_c_list.append(c_Um)
            P_theta_CB_list.append(180*math.acos(Cos_theta_CB)/math.pi)
            P_delta_G_list.append(G_W-G_CB)

#-----DATA CALCULATION FINISHED-----

#-----BEGIN DATA ANALYSIS-----

# ENERGY APPROACH
# Checking if a stable Cassie state exists
# If not proceed to analyze metastable state
print('\nENERGY APPROACH RESULTS')

```



```

if len(delta_G_list)==0: # If no stable Cassie state
    print ('no feasible dimensions for stable Cassie-Baxter wetting state')
    Final_solutions.append(['no feasible dimensions for stable Cassie-Baxter wetting state','\n','mestable
state analysis results'])

# analyse metastable state
if len(Energy_gap)!=0:
    E_max=min(Energy_gap)
    E_max_index=Energy_gap.index(E_max)
    a2=A_list[E_max_index] # resulting dimensions in micrometers
    b2=B_list[E_max_index]
    c2=C_list[E_max_index]
    print('\nsolution with maximum C-W energy transition gap')
    print('a=',a2)
    print('b=',b2)
    print('c=',c2)

    Final_solutions.append(['\ntheta_CB> 90 solutio set','\n'])
    for i in range(0,len(theta_CB_list_2)):
        if theta_CB_list_2[i]<0: # Filtering the theta_CB> 90 degree solution set
            solution_set=[A_list[i],B_list[i],C_list[i],theta_CB_list_2[i]]
            Final_solutions.append(solution_set)

    Final_solutions.append(['\ntheta_CB< 90 solutio set','\n'])
    for i in range(0,len(theta_CB_list_2)):
        if theta_CB_list_2[i]>0: # Filtering the theta_CB< 90 degree solution set
            solution_set=[A_list[i],B_list[i],C_list[i],theta_CB_list_2[i]]
            Final_solutions.append(solution_set)

elif len(Energy_gap)==0:
    print ('no feasible dimensions with local minimum for Cassie-Baxter wetting state')
    Final_solutions.append(['no feasible dimensions with local minimum for Cassie-Baxter wetting state'])

# Filtering the most stable Cassie state by identifying the largest Gibb's energy gap
else:
    G_max=max(delta_G_list) # find the maximum delta_G gap
    G_max_solution_index_list=[]
    G_max_theta_CB_solution_list=[]
    G_max_a_solution_list=[]
    G_max_b_solution_list=[]
    G_max_c_solution_list=[]
    for m in range(len(delta_G_list)):
        if delta_G_list[m]>=G_max:
            G_max_solution_index_list.append(m)
            G_max_theta_CB_solution_list.append(theta_CB_list_1[m])
    max_theta_CB=max(G_max_theta_CB_solution_list)
    for n in range(len(G_max_theta_CB_solution_list)):
        if G_max_theta_CB_solution_list[n]>=(max_theta_CB):
            G_max_a_solution_list.append(a_list[G_max_solution_index_list[n]])
            G_max_b_solution_list.append(b_list[G_max_solution_index_list[n]])
            G_max_c_solution_list.append(c_list[G_max_solution_index_list[n]])

    print('Maximum Gibbs energy difference >> then maximum theta_CB')
    print('a=',G_max_a_solution_list)
    print('b=',G_max_b_solution_list)
    print('c=',G_max_c_solution_list)
    print('Contact Angle CB= ',max(G_max_theta_CB_solution_list))

```

```

print('Gibb\'s energy difference= ', G_max)

Final_solutions.append(['\ntheta_CB> 90 solutio set','\n'])
for i in range(0,len(theta_CB_list_1)):
    if theta_CB_list_1[i]<0: # Filtering the theta_CB> 90 degree solution set
        solution_set=[a_list[i],b_list[i],c_list[i],theta_CB_list_1[i]]
        Final_solutions.append(solution_set)

Final_solutions.append(['\ntheta_CB< 90 solutio set','\n'])
for i in range(0,len(theta_CB_list_1)):
    if theta_CB_list_1[i]>0: # Filtering the theta_CB< 90 degree solution set
        solution_set=[a_list[i],b_list[i],c_list[i],theta_CB_list_1[i]]
        Final_solutions.append(solution_set)

#----- BREAKTHROUGH PRESSURE APPROACH-----

print('\nPRESSURE APPROACH RESULTS')
P_max=min(Pb_list)
P_theta_CB_solution_list=[]
P_solution_index_list=[]
P_a_solution_list=[]
P_b_solution_list=[]
P_c_solution_list=[]
for m in range(len(Pb_list)): # To find indexes with P_max value
    if Pb_list[m]<=math.ceil(P_max):
        P_solution_index_list.append(m) # collecting all the indexes of P_max values
        P_theta_CB_solution_list.append(P_theta_CB_list[m]) # collect corresponding theta_CB values
max_theta_CB=max(P_theta_CB_solution_list)
for n in range(len(P_theta_CB_solution_list)):
    if P_theta_CB_solution_list[n]>=max_theta_CB:
        P_a_solution_list.append(P_a_list[P_solution_index_list[n]])
        P_b_solution_list.append(P_b_list[P_solution_index_list[n]])
        P_c_solution_list.append(P_c_list[P_solution_index_list[n]])

P_max_index=Pb_list.index(P_max) # gives a, b pairs with maximum breakthrough pressure

# to find a most suitable c value, select a c pair for above a, b solutions with maximum C-->W transition
energy barrier
for k in range(len(P_c_solution_list)):
    c=(P_c_solution_list[k])*10**(-6)
    a=(P_a_solution_list[k])*10**(-6)
    b=(P_b_solution_list[k])*10**(-6)
    A_sl_CB_1=b**2+a*b*(3**0.5+3)
    n=c*L/A_sl_CB_1 # n - pillar slenderness ratio (HL/A)
    E=-n*f*math.cos(theta_radian)*Gamma_la # Energy barrier calculation for Cassie to Wenzel transfer
    Energy_gap_list2.append(abs(E))

E_max_2=max(Energy_gap_list2)
E_max_2_index=Energy_gap_list2.index(E_max_2)

print('Maximum breakthrough pressure >> then maximum theta_CB >> then maximum transition energy
barrier')
print('a=',P_a_solution_list)
print('b=',P_b_solution_list)
print('c=',P_c_solution_list)
print('a=',P_a_solution_list[E_max_2_index])
print('b=', P_b_solution_list[E_max_2_index])
print('c=', P_c_solution_list[E_max_2_index])
print('Contact Angle_CB=',round(max_theta_CB,2))

```

```
print('Breakthrough pressure=',round(P_max,2))  
print('C-->W transition barrier= ',E_max_2)
```

APPENDIX III: Optimization code results

Cylindrical hole optimization results

ENERGY APPROACH RESULTS

Maximum Gibbs energy difference >> then maximum theta_CB

a= [25]

b= [149]

c= [5]

Contact Angle_CB= 37.47891496456475

Gibb's energy difference= 9.227468795455175e-12

PRESSURE APPROACH RESULTS

Maximum breakthrough pressure >> then maximum theta_CB >>
then maximum transition energy barrier

a= [25]

b= [18]

c= [5]

a= 25

b= 18

c= 5

Breakthrough pressure= -983.68

Contact Angle_CB= 70.18

C-->W transition barrier= 0.0013385337209762473

Hexagonal hole optimization results

ENERGY APPROACH RESULTS

no feasible dimensions for stable Cassie-Baxter wetting
state

solution with maximum C-W energy transition gap

a= [127]

b= [36]

c= [16]

Contact Angle_CB= 121.55

C--> W energy gap= 0.0013209880827411763

PRESSURE APPROACH RESULTS

Maximum breakthrough pressure >> then maximum theta_CB >>
then maximum transition energy barrier

a= [80, 80, 80, 80, 80, 80, 80, 80, 80, 80, 80, 80, 80, 80]

b= [81, 81, 81, 81, 81, 81, 81, 81, 81, 81, 81, 81, 81, 81]

c= [5, 6, 7, 8, 9, 10, 11, 12, 13, 14, 15, 16, 17, 18]

a= 80

b= 81

c= 18

Breakthrough pressure= -177.48

Contact Angle_CB= 84.43

C--> W energy gap= 0.0015895336331151848

APPENDIX IV: Increased surface area calculation after laser micromachining

a) LIPSS surfaces

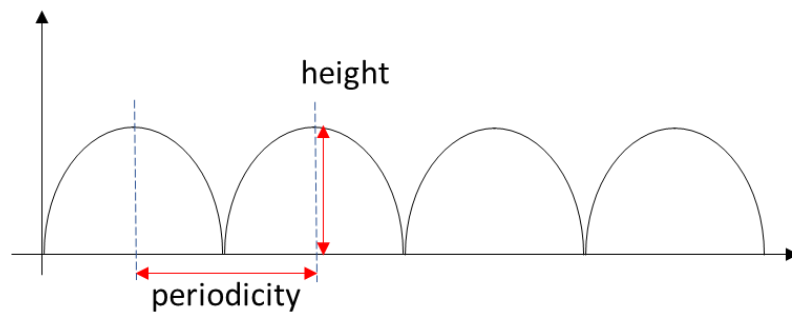


Figure 57 The model used to estimate the surface area of the ripple structure. Closely packed ridges with parabolic cross section were assumed.

Table 12 Surface area calculations for LIPSS and L_LIPSS samples

Parameter	Value	Units	Comments
<i>periodicity</i>	604	nm	Experimentally measured on SEM images using ImageJ software
<i>height</i>	60	nm	From literature
<i>arc length</i>	619.54	nm	Calculated
<i># of ripples per 21 μm</i>	25		Experimentally measured on SEM images using ImageJ software
<i># of ripples per 1 μm</i>	1.19048		
<i>actual length along 1 μm length</i>	1018.50000	nm	
<i>actual length along 1 μm length</i>	1.01850	μm	
<i>ratio</i>	1.01850		

b) Circular holes

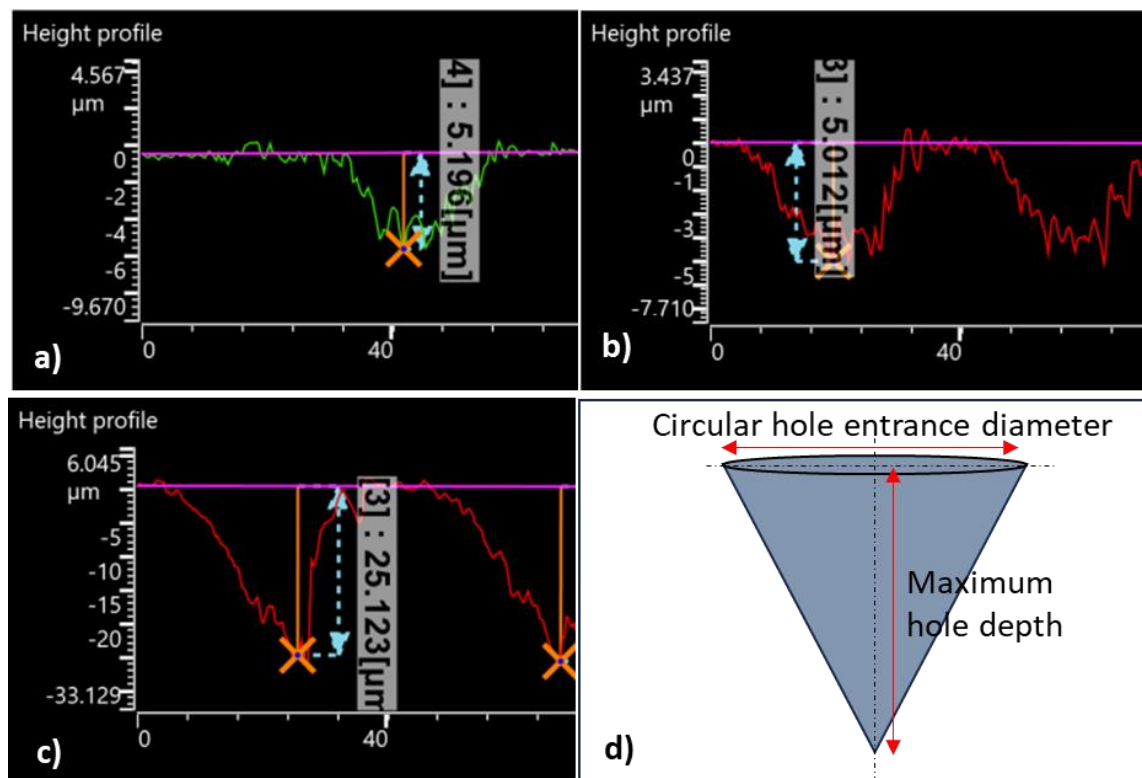





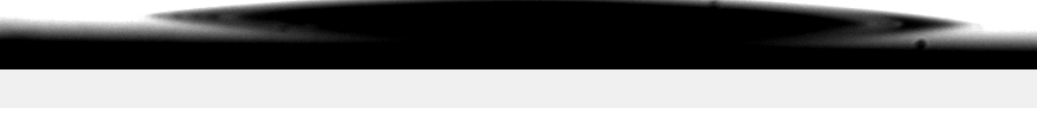
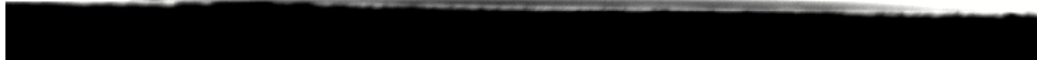
Figure 58 Example a) CY_P1 b) CY_P2 c) CY_P3 depth profile from confocal d) Model used for a circular hole for the estimation of surface area. A conical shape was assumed.

APPENDIX V: Increased surface area calculation after laser micromachining

CA angle measurement procedure: The resin droplet was deposited on the laser modified substrate which has been stabilized at the 60 °C temperature.

Results:

All the samples showed complete spreading (contact angle $\sim 0^\circ$) within 2 minutes after the droplet deposition.

Sample	Snapshot of the droplet 1 minute after the deposition
LIPSS	
L_LIPSS	
CY_P1	
CY_P2	
CY_P3	
HX_P2	